SIGNAL PROCESSING BASED METHOD FOR SOLVING INVERSE SCATTERING PROBLEMS

by

Umer Shahid

A dissertation submitted to the faculty of
The University of North Carolina at Charlotte
in partial fulfillment of the requirements
for the degree of Doctor of Philosophy in
Optical Science and Engineering

Charlotte

2009

Approved by:

Dr. Michael A. Fiddy

Dr. Robert K. Tyson

Dr. M. Yasin Akhtar Raja

Dr. Greg Gbur

Dr. Boris R. Vainberg

ABSTRACT

The problem of reconstructing an image of the permittivity distribution inside a penetrable and strongly scattering object from a finite number of noisy scattered field measurements has always been very challenging because it is ill-posed in nature. Several techniques have been developed which are either computationally very expensive or typically require the object to be weakly scattering. I have developed here a non-linear signal processing method, which will recover images for both strong scatterers and weak scatterers. This nonlinear or cepstral filtering method requires that the scattered field data is first preprocessed to generate a minimum phase function in the object domain. In 2-D or higher dimensional problems, I describe the conditions for minimum phase and demonstrate how an artificial reference wave can be numerically combined with measured complex scattering data in order to enforce this condition, by satisfying Rouche's theorem. In the cepstral domain one can filter the frequencies associated with an object from those of the scattered field. After filtering, the next step is to inverse Fourier transform these data and exponentiate to recover the image of the object under test. In addition I also investigate the scattered field sampling requirements for the inverse scattering problem. The proposed inversion technique is applied to the measured experimental data to recover both shape and relative permittivity of unknown objects. The obtained results confirm the effectiveness of this algorithm and show that one can identify optimal parameters for the reference wave and an optimal procedure that results in good reconstructions of a penetrable, strongly scattering permittivity distribution.

ACKNOWLEDGMENTS

I thank my advisor Dr. Michael A. Fiddy, for his patient guidance and constant encouragement during the course of my research. Dr.Fiddy provided me with timely and instructive comments at every stage of the research process, allowing me to complete this research on schedule.

I would like to thank my committee members Dr. Robert Tyson, Dr. Yasin Raja, Dr. Greg Gbur and Dr. Boris Vainberg for their encouraging words, thoughtful criticism, time and attention during a busy semester.

I would never have been able to finish my dissertation without the support from my wife Beenish. She was always there cheering me up and supporting me throughout the dissertation process. My father, Shahid Bashir, and my mother, Ghazala Shahid, gave me the confidence to pursue for PhD. My aunty/mother Saima Shahid, who always believed in me. My uncles Dr.Arif Bashir and Dr.Khalid Bashir, always encouraged me to go for higher education. Finally, I would like to thank my lovely daughters Zara and Zunaira for letting me hide in my room and write this dissertation.

TABLE OF CONTENTS

LIST OF FIGURES

CHAPTER 1: INTRODUCTION AND LITERATURE REVIEW

1.1 THE INVERSE SCATTERING PROBLEM

The inverse scattering problem is the attempt to find the physical and optical properties of an unknown penetrable scattering object from a limited set of scattered field data, available only outside the scatterer. For penetrable scattering objects in a homogeneous background, the solution to the inverse scattering problem requires knowledge of the total field within the scattering volume. A successful solution should not only give us the shape of the scattering object but it should also provide a meaningful quantitative description of the scattering object such as its spatial distribution of permittivity, conductivity or other internal constitutive parameters.

The problem of reconstructing the object from measured scattered field data has many vital sensing and remote sensing applications e.g. target identification, biomedical imaging, remote sensing, geophysical imaging, structure synthesis and non-destructive testing.

One limited formalism of the inverse scattering problem is diffraction tomography which attempts to solve the inverse scattering problem by employing weak scattering approximations. Diffraction tomography is a Fourier-inversion based imaging technique in which a weakly scattering object, represented by its complex permittivity, is illuminated with a known incident plane wave in many directions and the far-field (or near field) scattering data are measured, ideally, all around the object. Using these

measured far-field data and employing weak scattering approximations, diffraction tomography attempts to reconstruct the scattering object's permittivity profile. Based on diffraction tomography many algorithms have been developed but their usefulness is limited as they only work for weak scatterers whereas most of the objects encountered in real life are clearly strongly scattering.

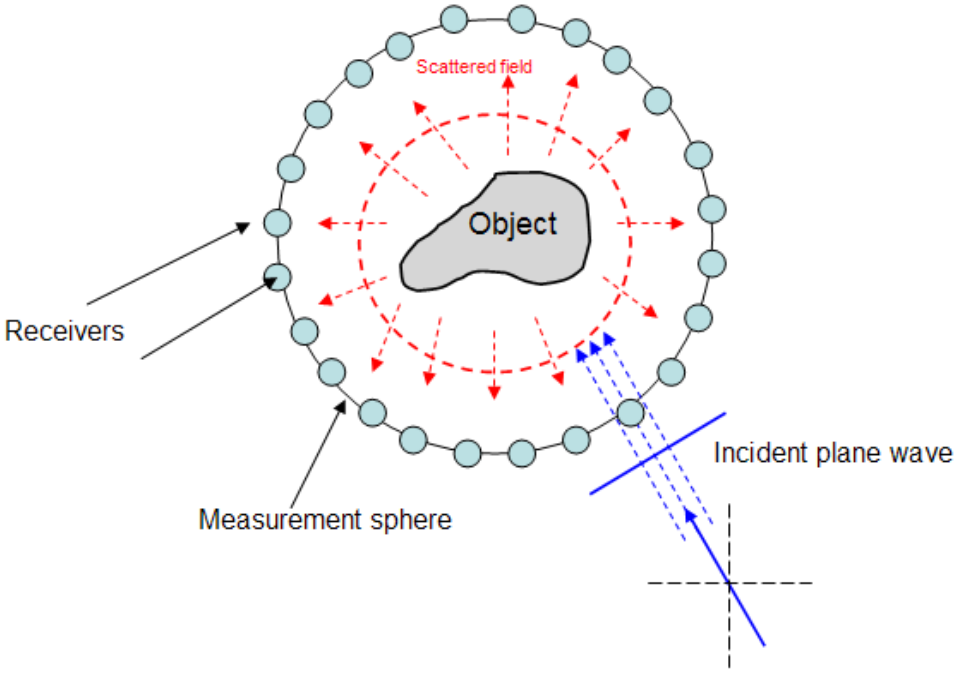

Figure.1.1. Typical experimental setup for diffraction tomography. Object is illuminated with monochromatic plane wave and the transmitted waves, after the interaction of the incident plane wave with the scattering object, are collected with receivers all around the object.

Both electromagnetic and acoustic radiation have been used to image scattering objects using diffraction tomography.

Imaging with x-ray wavelengths can be modeled using a geometrical optics or ray-projection description since it normally involves structural details of the object to be much larger than the wavelength being used. X-ray tomography is based on the Fourier

slice theorem [1]. It utilizes the fact that x-rays travel in straight lines through the object and after interacting with the object, x-rays undergo an attenuation which can be represented mathematically by a line integral. X-ray tomography has been in use for a long time but, in medical applications for example, it fails to distinguish between various types of soft tissues. It therefore is mainly used in orthopedics and not for detecting small tumors. Also x-rays are ionizing radiation and there is high energy associated with x-ray photons, which can lead to hazardous side effects such as increased cancer risk and chromosome breakage.

Being inexpensive and clinically safe, ultrasonic imaging has gained a lot of attention over the years; it has been in use for medical imaging for over 50 years. Despite ultrasound having been in use by the medical community for a long time, these waves are longitudinal and/or shear waves which makes it quite difficult to retrieve a quantitative description of an object especially if that object is strongly scattering. For weak inhomogeneities, tomography with acoustic waves still yields reasonable results but as object inhomogeneities becomes stronger, the performance of ultrasonic diffraction tomography rapidly degrades. Also the fact that ultrasonic waves are not very penetrating for the application of medical imaging, there can be significant scattering by bones and different types of tissue which makes it very difficult to recover quantitative and qualitative description of object with acoustic waves.

Microwaves are low energy transverse electromagnetic waves i.e. relatively safe electromagnetic waves compared to x-rays. With microwave imaging, the quantitative description of the object under test could be recovered in terms of refractive index or permittivity. The ability of microwaves to recover a quantitative description of an object

makes it very attractive in biomedical imaging of tissues, although the resolution might be less than hoped for.

1.2 THEORETICAL CONCERNS

The inverse scattering problem is well-understood in the one-dimensional regime. A detailed discussion on the subject can be found in [3] [4]. Typically the data to be inverted are taken as reflection and transmission coefficients and then 1-D inversion algorithms are applied to retrieve the 1-D object profile.

The two dimensional inverse scattering problem has been under investigation for many years now [7]-[15]. Much work has been done to address this problem for the weak scattering case i.e. when multiple scattering effects are negligible. Most of these algorithms are based on linearizing the inverse scattering problem by using Born or Rytov approximations [1]; these will be discussed in detail in chapter 3. Although these algorithms are computationally very attractive, their applicability is limited in practice as most of the objects of practical interest are strong scatterers. Consider the 2-D scattering problem as a scalar wave problem initially. I will also assume that, for some simulations, the objects under consideration are cylindrically symmetric with constant dielectric properties along a cylindrical axis. For the transverse magnetic (TM) case i.e. the electric field vector is parallel to the cylindrical axis, all the vectors will have the same direction and the problem is translated to a simple 2D scalar problem. This will also ensure that the scattering object has no depolarization effects.

There are a lot of difficulties associated with solving the inverse scattering problem because it is ill-posed in nature. Problems are considered as ill-posed

(Hadamard 1923) if i) a solution does not exist, ii) solution is non-unique, or iii) the solution is unstable.

For the inverse scattering problem it is possible that a solution may not exist for the given scattered field or even if it exists, it may not depend continuously on the scattered field data. For the first condition I assume that the solution exists for the class of target objects under considerations. The inverse scattering problem is essentially a non-unique problem in the sense that its solution has to be chosen from a space of possible solutions. It is possible for two different sources to produce the same propagating field outside a given scattering surface or two different objects may generate similar scattered fields at only a finite number of measurement locations, thus making the problem of inverse scattering non-unique. The field outside the localized scattering potential may not be sufficient to uniquely determine the field within the scattering volume.

The scattering data produced as a result of an experiment involving a single scattering object using a unit amplitude incident plane wave is not adequate to uniquely specify the scatterer. Even with the appropriate use of the Born approximation, it is impossible in principle to uniquely identify the scattering structure from measurements of the field external to the scattering volume in any finite number of scattering experiments using incident plane waves [4]. However if sampling points are chosen appropriately such that the scattering pattern is well-represented and we have some *a priori* knowledge about the object or class of objects, then a unique solution can be found in the sense a global minimum can be found in some solution space, often shaped by available prior knowledge.

The stability of the inverse scattering problem depends upon the system response *h*, which maps input *x* to output *y*.

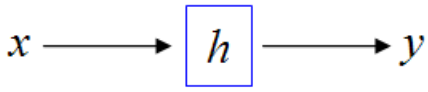

$$y = hx \tag{1.1}$$

The inverse problem is stable if h^{-1} exists and is stable. If *h* is continuous and h^{-1} exists then h^{-1} is continuous [6]. Even if h^{-1} exists and is continuous, the noise in the measurement may lead to instabilities and discontinuities. For the inverse scattering problem, the operator *h* is an integral equation and Eq. 1.1 is a Fredholm integral equation of the first kind having a square integrable (Hilbert-Schmidt) kernel which in general form could be written as

$$y(t) = hx(s) \qquad y(t) = \int_a^b u(t,s)x(s)ds \tag{1.2}$$

For the inverse scattering problem *y(t)* is the system output, *u(t,s)* is the system response and *x(s)* is the object function or scatterer. A small error in the measured data may cause a large error in the reconstructed results. If a solution *x* is perturbed by

$$\delta x(s) = \varepsilon \sin(2\pi cs) \quad where\ c = 1,2,3...., \varepsilon = \text{constant}$$

Then the perturbation in the output *y(t)* is given by

$$\delta y(t) = \varepsilon \int_a^b u(t,s)\sin(2\pi cs)ds, \qquad c = 1,2,....$$

Using the Riemann-Lebesgue lemma it follows that

$$\delta y \to 0 \quad as \ \ c \to \infty$$

$\|\delta x\|/\|\delta y\|$ can become very large by choosing integer c large enough, thus showing that Eq. 1.2 is ill-posed because it is discontinuous. The stability of the solution can be improved by reducing the measurement noise and carefully selecting sample points. The measurement locations should be chosen to include as much information about the scattering function as possible. Also the non-linear relationship between the scatterer and scattered field makes it very hard to find the closed form solution of the inverse scattering problem. There are approximations to linearize the problem but these approximations are only valid for a limited class of objects.

In this dissertation I propose a nonlinear filtering technique based on homomorphic filtering which can address the strongly scattering case in a completely universal way. This technique is straightforward to implement. The proposed algorithm starts with the diffraction tomography formalism and then preprocesses the results of diffraction tomography before applying the nonlinear filtering algorithm to recover meaningful images of a strongly scattering target. The proposed method is computationally attractive as it requires only two fast Fourier transforms. The preprocessing step ensures that the data being filtered fulfills the so-called minimum phase condition. With minimum phase scattered field data, the nonlinear filtering operation can be executed in a reliable and stable fashion. The proposed algorithm is applied to the real data provided by US Air Force Research Laboratory's (AFRL) [54]-[57] and Institut Fresnel [58]. These objects fall under the category of strong scatterers and linearizing techniques do not provide satisfactory reconstructions. I will show the reconstructions of these targets both in terms of shape and permittivity. The scattered field measurements provided by AFRL and Institut Fresnel are at a limited number of

data points. I investigate the significance of this on the quality of the reconstructions obtained by the proposed method and others' methods.

Since limited data are always an inevitable limitation of any experiment, I anticipated the need to also make use of spectral estimation techniques to assist with the reconstruction steps. I demonstrate that by using spectral estimation techniques such as PDFT one can further enhance the quality of reconstruction. I also compare the reconstructions using the proposed method with reconstructions achieved by using methods published by other authors. I estimate the quality of reconstructions using the cepstral filtering method alongside the most commonly used alternative reconstruction methods in terms of shape recovery, permittivity recovery and computational power.

One of the principal results of this research was to show that for optimum reconstruction of the image of the target, the scattered field sampling rate chosen is critical. It has to be chosen based on the scattering strength of the object being imaged. I propose a need for a sampling theorem for inverse scattering problems which takes into account the strength of the scattering object and the wavelength of the incident wave. The results of numerical experiments show that there exists a linear relationship between the permittivity of object and data density.

As a part of this research I have developed a graphical user interface (GUI), cepstral inversion tool, to implement the algorithm. This user-friendly tool loads scattered field data and in run time shows the reconstruction while we change parameters.

1.3 OUTLINE OF DISSERTATION

The dissertation is organized as follows: Chapter 2 gives an overview on the problem description and mathematical background of the inverse scattering problem. Chapter 3 discusses the well-known methods for solving inverse scattering problems. Chapter 3 also includes a brief discussion on both linearizing techniques and iterative methods. Chapter 4 explains in detail the proposed method which is based on homomorphic filtering and minimum phase function. It discusses how scattered field data can be preprocessed to enforce the minimum phase condition and apply filtering in the cepstral domain. In Chapter 5 the proposed algorithm is applied on real scattered data and the reconstructions for each object are shown. Comparisons of reconstructions between cepstral inversion method and reconstructions from other methods are also shown in this chapter. This chapter also discusses the sampling needs for the inverse scattering problem. Finally, in the conclusions, the research is summarized and future prospects are discussed.

CHAPTER 2: MATHEMATICAL FORMULATION OF THE INVERSE SCATTERING PROBLEM

2.1 CLASSIFICATION OF INVERSE SCATTERING PROBLEMS

In a broad sense the inverse scattering problem is classified into two categories: a) weak scattering and b) strong scattering. Weak scatterers refer to the class of objects in which the "wave" gets scattered only once. The effect of multiple scattering is negligible and the incident field undergoes an insignificant perturbation after interacting with the scatterer. Many successful algorithms are available to solve weak inverse scattering problems. These are based on the first Born or Rytov approximations [1][7]. These algorithms linearize the inverse scattering problem and establish a Fourier relationship between the measured scattered field data and the scattering function. Even though these algorithms are numerically attractive, they lack usefulness in practice since generally objects encountered in real life do not fall into the category of weak scatterers. Most real targets belong to the class of strong scatterers. Effects of multiple scattering can no longer be ignored and the incident wave goes through considerable perturbations after interacting with the scattering function. Multiple scattering effects introduce a nonlinear relationship between the scattered field and the scatterer [2], thus making the inverse scattering problem very difficult to solve. Many methods have been proposed to solve the inverse problem for strong scatterers by making certain underlying assumptions about the scattering problem. I will discuss these methods in detail in chapter 3.

2.2 THEORETICAL BACKGROUND ON THE INVERSE SCATTERING PROBLEM

An inverse scattering experiment could be set up as shown in Fig.2.1. The transmitter and receiver can rotate about the center of 2-D scattering object. The incident plane wave illuminates the object at an angle ϕ_{inc} with respect to *x-axis* and scattered field is detected at an angle ϕ_s in the far-field.

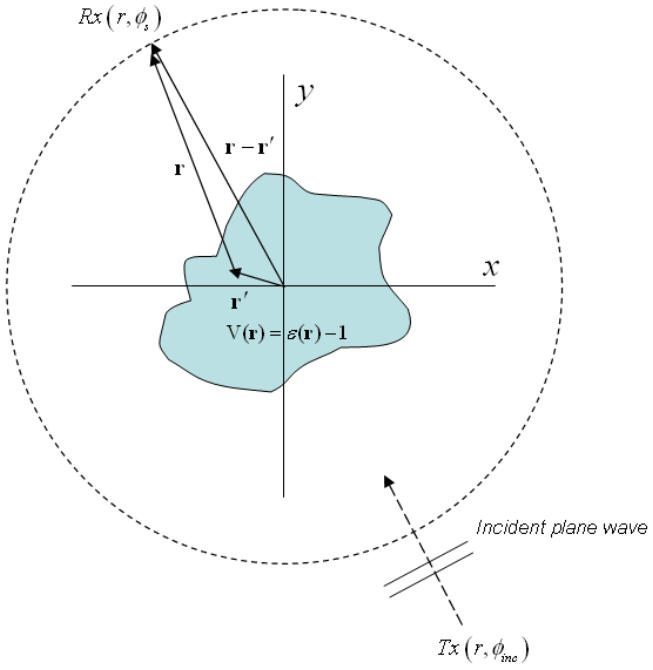

Figure. 2.1. A typical 2D inverse scattering experimental setup. Transmitter Tx transmits incident monochromatic plane wave to the scattering object V(r). The receivers Rx are located all around the object which collect scattered field data after the interaction of incident wave with scattering object.

Consider a penetrable scattering object, V(**r**) in a homogeneous background of permittivity ε_o, where ε_o is free space permittivity. The object has permittivity of $\varepsilon(\mathbf{r})$ and it is related to the object as

$$\mathrm{V}(\mathbf{r}) = \varepsilon(\mathbf{r}) - 1 . \tag{2.1}$$

V(**r**) represents permittivity fluctuations relative to free space and with the coordinate system shown in Fig.2.1 where **r** = (*x*,*y*). The scattering potential V(**r**) is zero at all points outside the object which has a compact support domain D i.e. V(**r**) is an entire function which is completely determined by its exact values inside the window but it could only be reconstructed outside of it by using analytic continuation. The incident plane wave i.e. plane wave measured in the absence of object, is governed by the scalar homogeneous Helmholtz equation [1];

$$\nabla^2 + k^2 \ \Psi_{inc}(\mathbf{r}) = 0 \tag{2.2}$$

where k is the wave number and it is given as $k = 2\pi / \lambda$. The solution of Ψ_{inc} could be written in terms of a plane wave

$$\Psi_{inc}(\mathbf{r}) = e^{ik\hat{\mathbf{r}}_{inc}\bullet\mathbf{r}} \ . \tag{2.3}$$

where $\hat{\mathbf{r}}_{inc}$ is the unit vector that specifies incident field direction. The total field $\Psi(\mathbf{r})$ as a result of interaction of incident field $\Psi_{inc}(\mathbf{r})$ with object $\mathrm{V}(\mathbf{r})$ satisfies the inhomogeneous Helmholtz equation [1]

$$\nabla^2 + k^2 \ \Psi(\mathbf{r}) = -k^2 \mathrm{V}(\mathbf{r})\Psi(\mathbf{r}) . \tag{2.4}$$

The total field in Eq. 2.4 can be expressed as sum of incident field and scattered field

$$\Psi(\mathbf{r}) = \Psi_{inc}(\mathbf{r}) + \Psi_s(\mathbf{r}) \tag{2.5}$$

where

Ψ_{inc} : Incident field at position defined by **r**;

Ψ_s : Scattered field at position defined by **r**;

We can express the total field $\Psi(\mathbf{r})$ in terms of an inhomogeneous Fredholm integral equation of first kind [8]

$$\Psi(\mathbf{r},\hat{\mathbf{r}}_{inc}) = \Psi_{inc}(\mathbf{r}) - k^2 \int_D \mathrm{V}(\mathbf{r}')\Psi(\mathbf{r}',\hat{\mathbf{r}}_{inc})G_o(\mathbf{r},\mathbf{r}')d\mathbf{r}' \tag{2.6}$$

where $G_o(\mathbf{r},\mathbf{r}')$ is the Green's function which is the solution of scalar Helmholtz equation (Eq. 2.4) and it satisfies differential equation [8]

$$\nabla^2 + k^2 \;\; G_o(\mathbf{r},\mathbf{r}') = \delta(\mathbf{r}-\mathbf{r}')\,. \tag{2.7}$$

Green's function $G_o(\mathbf{r},\mathbf{r}')$ is the field amplitude at $\mathbf{r}$ generated by given point source located at $\mathbf{r}'$. Since space is rotationally symmetrical and homogeneous, one can solve for $G_o(\mathbf{r},\mathbf{r}')$ in spherical coordinates with origin at $\mathbf{r}'$;

$$\nabla^2 + k^2 \;\; G_o(\mathbf{r}) = -\delta(\mathbf{r}) = -\delta(x)\delta(y)\delta(z)\,. \tag{2.8}$$

For homogeneous, spherically symmetrical PDE the solution is

$$G_o(\mathbf{r}) = \frac{Ce^{ikr}}{r} + \frac{Ue^{-ikr}}{r}\,. \tag{2.9}$$

By radiation boundary condition i.e. sources can not be present at infinity, only outgoing wave solution exists and therefore U=0

$$G_o(\mathbf{r}) = \frac{Ce^{ikr}}{r}\,. \tag{2.10}$$

Substituting $G_o(\mathbf{r})$ from Eq. 2.10 into Eq. 2.8 and integrating over a small volume ΔV about its origin

$$\int_{\Delta V} dV \;\; \nabla^2 + k^2 \;\; \frac{Ce^{ikr}}{r} = \int_{\Delta V} dV(-\delta(x)\delta(y)\delta(z)) \tag{2.11}$$

$$\int_{\Delta V} dV \;\; \nabla^2 + k^2 \;\; \frac{Ce^{ikr}}{r} = -1$$

$$\int_{\Delta V} \nabla^2 \frac{Ce^{ikr}}{r} dV + \int_{\Delta V} k^2 \frac{Ce^{ikr}}{r} dV = -1 . \tag{2.12}$$

As V becomes smaller and smaller the second term in above integral vanishes due to r^2 in $dV = r^2 \sin\theta dr d\theta d\phi$ therefore Eq. 2.12 becomes

$$\int_{\Delta V} \nabla^2 \frac{Ce^{ikr}}{r} dV = -1 .$$

Rearranging the above equation such that

$$\int_{\Delta V} \nabla^2 \frac{Ce^{ikr}}{r} dV = \int_{\Delta V} dV \nabla \cdot (\nabla \frac{Ce^{ikr}}{r}) = -1.$$

Applying the divergence theorem to above equation

$$\int_{\Delta V} dV \nabla \cdot (\nabla \frac{Ce^{ikr}}{r}) = \oiint_S \nabla \frac{Ce^{ikr}}{r} d\mathbf{S} = -1$$

$$\oiint_S \left(\frac{\partial}{\partial r} \frac{Ce^{ikr}}{r} d\mathbf{S} \right) r^2 \sin\theta d\theta d\phi = -1$$

$4\pi C = -1$ (as r approaches to 0)

$$C = \frac{1}{4\pi} . \tag{2.13}$$

Putting value of C from Eq. 2.13 into Eq. 2.10

$$G_o(\mathbf{r}) = \frac{e^{ikr}}{4\pi r} .$$

Shifting source point back to $\mathbf{r}'$ we find the Green's function

$$G_o(\mathbf{r}, \mathbf{r}') = \frac{e^{ik|\mathbf{r}-\mathbf{r}'|}}{4\pi |\mathbf{r}-\mathbf{r}'|} . \tag{2.14}$$

Eq. 2.14 is the Green's function for solving inhomogeneous Helmholtz equation. In 2-D problems Green's function can be expressed in terms of a zero order Hankel function of first kind [2][6].

$$G(\mathbf{r},\mathbf{r}') = \frac{-i}{4} H_o^{(1)} k\left|\mathbf{r}-\mathbf{r}'\right| \tag{2.15}$$

Using asymptotic approximation i.e. as $\mathbf{r} \to \infty$ the Hankel function is written as

$$H_o^{(1)} = \frac{4}{i}\frac{1}{\sqrt{8\pi kr}} e^{i\,kr+\pi/4}\, e^{-ik\hat{\mathbf{r}}\bullet\mathbf{r}'}. \tag{2.16}$$

where $\hat{\mathbf{r}} = \dfrac{\mathbf{r}}{|\mathbf{r}|}$. Putting $H_o^{(1)}$ in Eq. 2.15 to find 2-D Green's function

$$G(\mathbf{r},\mathbf{r}') \simeq -\frac{1}{\sqrt{8\pi kr}} e^{i\,kr+\pi/4}\, e^{-ik\hat{\mathbf{r}}\bullet\mathbf{r}'} k\left|\mathbf{r}-\mathbf{r}'\right|. \tag{2.17}$$

from Eq. 2.5, Eq. 2.6 and Eq. 2.17 we can write scattered field as

$$\Psi_s(\hat{\mathbf{r}},\hat{\mathbf{r}}_{inc}) = \frac{1}{\sqrt{8\pi kr}} e^{i\,kr+\pi/4}\, k^2 \int_D \mathrm{V}(\mathbf{r}')\, e^{-ik\hat{\mathbf{r}}\bullet\mathbf{r}'} \Psi(\mathbf{r}',\hat{\mathbf{r}}_{inc})\, d\mathbf{r}'. \tag{2.21}$$

where $\hat{\mathbf{r}}_{inc} = (\cos\phi_{inc}, \sin\phi_{inc})$ is the unit vector defining direction of incident plane wave and $\hat{\mathbf{r}} = (\cos\phi_s, \sin\phi_s)$ is the unit vector defining direction of scattered. In order to solve for scattering object $\mathrm{V}(\mathbf{r})$ we need to know total field $\Psi(\mathbf{r})$ inside the object. The total field inside the object is unknown as $\mathrm{V}(\mathbf{r})$ is not known, thus making it very difficult to solve the above integral equation which is also classified as Fredholm integral equation of first kind.

CHAPTER 3: WELL-KNOWN METHODS FOR SOLVING INVERSE SCATTERING PROBLEMS

3.1 OVERVIEW

Based on the wavelength being employed in the scattering experiment we can classify the inverse scattering problem as:

i. Object inhomogeneities are much larger than the incident wavelength i.e. parameter ka >> 1.

ii. Object inhomogeneities are of the order of incident wavelength i.e. parameter ka ≈ 1.

In the first scenario, which is the high frequency regime, one can adopt geometrical optics or ray optics models. Energy propagation is characterized by refraction and multipath effects. X-ray based imaging is one example in which measured data corresponds to a line integral; as X-rays suffer little from diffraction effects for objects which are non-crystalline. However when we try to use a straight ray assumption for acoustic waves or longer wavelength electromagnetic waves, then measured data are affected by diffraction and can no longer be represented by line integrals [1]. Algebraic reconstruction is the technique that has been proposed to address this problem [1]; an initial estimate of the refractive index is used to determine the ray path. This method works well for weak scattering targets as it eventually converges to the correct refractive index after few iterations. For the case when object inhomogeneities are of

the order of the wavelength being used, we need to know the field inside the object. By definition this is unknown therefore we need to make some assumptions about the nature of the field in order to solve the inverse scattering problem. Linearizing techniques have been frequently adopted to invert scattering data. The first Born and Rytov approximations are the most widely used techniques [1]. Using the Born (BA) or Rytov approximations (RA), the measured scattered field data in the far-field (or near field) may be related to the Fourier transform of object. Even though these linearizing approximations are simple and computationally very attractive, their usefulness is limited in practice. For objects with high permittivity values the effect of multiple scattering becomes more significant and BA and RA fail to give good reconstructions. Ramm proposed an exact inversion method [16] [17] [18]. It has not been proven that an exact inversion method, which is computationally very complex, works on real data or not. Iterative reconstruction algorithms have gained a lot of attention to solve the inverse scattering problem for strongly scattering objects. These iterative techniques try to minimize difference between measured data and simulated data using nonlinear optimization methods. The conjugate gradient method is an iterative technique based on an optimization procedure solving the direct scattering problem at each step of iteration [12] [13]. Wang and Chew proposed iterative algorithms based on the Born iterative methods (BIM) [14] and the distorted Born iterative method (DBIM) [15]. It has been shown [83] that the DBIM is equivalent to Newton-Kantorovich method [82]. The DBIM method converges faster as compared to BIM but BIM has more immunity to noise. They also proposed a recursive aggregate T-matrix algorithm (RATMA) [19] to enhance the speed of DBIM. These iterative algorithms typically require longer

computational times and it has not been proven that they can successfully estimate an image of a strong scattering object from limited and noisy data.

In some of the more recent methods, Estatico and Pastorino used the second order Born approximation to develop an iterative method called the two step inexact Newton method [20]. In this approach they used the Gauss–Newton method (outer steps) for linearization and the truncated Landweber method (inner steps) for regularization. Berg *et al.* proposed contrast source inversion (CSI) algorithm based on the source-type integral equation which relates measured data to a source distribution in the scattering object [21]. In the CSI method, the contrast sources and the contrast itself are iteratively reconstructed by alternately updating the sources and the contrast. CSI is similar to the alternating direction implicit (ADI) method proposed by Kohn and McKenney [22] in which contrasts and sources are reconstructed iteratively by alternately updating the sources and the contrasts. CSI is similar to the modified gradient method in the sense that it does not require complete inversion of object equations. However, it is faster than the modified gradient method and uses less memory [23]. Berg *et al.* also proposed an extension to the CSI method known as MR-CSI [23] [24]. Song and Liu proposed DTA-CSI which is the combination of diagonal tensor approximation (DTA) and contrast source inversion (CSI) methods [25] [26] [27]. In this method DTA is used as an alternative to the Born approximation and reportedly it has shown better results than the Born approximation [27]. In DTA-CSI an initial estimate of the image is made using DTA and this estimate is then used in CSI as a starting point. Crocoo and Urso have proposed a theoretical model known as the Contrast Source Extended Born (CS-EB) [30] [31] method. It uses a contrast source as

the fundamental unknown in an integral equation and exploits the nature of the Green's function in a way to include the extended Born approximation. Recently Belkebir *et al.* proposed various iterative methods namely the modified^2 gradient method (M^2GM), the modified Born method (MBM), and the modified gradient method (MGM) [28] [29]. In the MGM the search direction is the conjugate gradient direction for the field, and the expansion coefficients for field and profile are determined simultaneously [29]. In MBM the field is considered as a fixed solution to the forward problem and the coefficients for field and profile are computed simultaneously [29]. In M^2GM both field directions are used to determine all coefficients simultaneously [29].

It is evident from the above citations that most of the recent work is based on iterative algorithms. Even though some of them have shown promising results, they are computationally very expensive and mostly fail to converge to a solution. In the next two sections I will be giving brief overview of the most popular linearizing and iterative techniques.

3.2 LINEARIZING INVERSE SCATTERING PROBLEMS

As discussed above, most of the linearizing algorithms are based on weak scattering approximations, BA and RA. These approximations give a Fourier relationship between the object function and measured scattered field data.

3.2.1 FIRST BORN APPROXIMATION

The first Born approximation serves as the basis for many weak scattering and iterative algorithms. It exploits the use of small dielectric perturbations. Recalling from chapter 2 that the total field is expressed as

$$\Psi(\mathbf{r}) = \Psi_{inc}(\mathbf{r}) + \Psi_s(\mathbf{r}) . \tag{3.1}$$

We could write it in terms of an inhomogeneous Fredholm integral equation of first kind [8]

$$\Psi(\mathbf{r}, \hat{\mathbf{r}}_{inc}) = e^{ik\hat{\mathbf{r}}_{inc}\bullet\mathbf{r}} + \frac{1}{\sqrt{8\pi kr}} e^{i\,kr+\pi/4}\, k^2 \int_D \mathrm{V}(\mathbf{r}')\, e^{-ik\hat{\mathbf{r}}\bullet\mathbf{r}'} \Psi(\mathbf{r}', \hat{\mathbf{r}}_{inc}) d\mathbf{r}' \tag{3.2}$$

where the 2nd term in above equation is the scattered field

$$\Psi_s(\mathbf{r}, \hat{\mathbf{r}}_{inc}) = \frac{1}{\sqrt{8\pi kr}} e^{i\,kr+\pi/4}\, k^2 \int_D \mathrm{V}(\mathbf{r}')\, e^{-ik\hat{\mathbf{r}}\bullet\mathbf{r}'} \Psi(\mathbf{r}', \hat{\mathbf{r}}_{inc}) d\mathbf{r}' \tag{3.3}$$

$$\Psi_s(\mathbf{r}, \hat{\mathbf{r}}_{inc}) = \frac{1}{\sqrt{8\pi kr}} e^{i\,kr+\pi/4}\; f(k\hat{\mathbf{r}}, k\hat{\mathbf{r}}_{inc}) \tag{3.4}$$

where $f(k\hat{\mathbf{r}}, k\hat{\mathbf{r}}_{inc})$ is the scattering amplitude which is defined as

$$f(k\hat{\mathbf{r}}, k\hat{\mathbf{r}}_{inc}) = k^2 \int_D \mathrm{V}(\mathbf{r}')\, e^{-ik\hat{\mathbf{r}}\bullet\mathbf{r}'} \Psi(\mathbf{r}', \hat{\mathbf{r}}_{inc}) d\mathbf{r}' . \tag{3.5}$$

The total field for scattering objects $\mathrm{V}(\mathbf{r})$ whose relative dielectric constant is closer to unity may be approximated by the incident field in the above integral equation [32]:

$$\Psi(\mathbf{r}, \hat{\mathbf{r}}_{inc}) = e^{ik\hat{\mathbf{r}}_{inc}\bullet\mathbf{r}} . \tag{3.6}$$

For the first Born approximation to be valid or an object to be classified as a weak scatterer, a necessary condition is that the product of object's permittivity, its characteristic dimension and wave number should be less than unity. Mathematically we can write it as

$$k\mathrm{V}(\mathbf{r})\mathrm{a} << 1 \tag{3.7}$$

where k is the wave number, object and permittivity are related by $\mathrm{V}(\mathbf{r}) = \varepsilon(\mathbf{r}) - 1$ and 'a' specifies the physical size of the object. As the dimensions of the object increase or the magnitude of permittivity fluctuations increase, the first Born approximation

becomes increasingly poor. The first Born approximation can be improved by increasing the wavelength of the incident plane wave but this in turn reduces the resolution of the reconstructed image. Using the first Born approximation, one assumes that the total field $\Psi(\mathbf{r},\hat{\mathbf{r}}_{inc})$ in the integral can be replaced by the known incident field, which linearizes this inversion problem

$$f^{BA}(k\hat{\mathbf{r}},k\hat{\mathbf{r}}_{inc}) = k^2 \int_D \mathrm{V}(\mathbf{r}')\, e^{-ik\,\hat{\mathbf{r}}-\hat{\mathbf{r}}_{inc}\,\cdot\mathbf{r}'} d\mathbf{r}' . \tag{3.8}$$

and the scattered field within first Born approximation is written as

$$\Psi_s^{BA}(\mathbf{r},\hat{\mathbf{r}}_{inc}) = \frac{1}{\sqrt{8\pi kr}} e^{i\,kr+\pi/4}\, k^2 \int_D \mathrm{V}(\mathbf{r}')\, e^{-ik\,\hat{\mathbf{r}}-\hat{\mathbf{r}}_{inc}\,\cdot\mathbf{r}'} d\mathbf{r}' . \tag{3.9}$$

Eq. 3.6 gives the Fourier relation between scattering object V(**r**) and the scattering amplitude $f^{BA}(k\hat{\mathbf{r}},k\hat{\mathbf{r}}_{inc})$. Ramm [33] showed an inconsistency associated with the Born approximation. The object V(**r**) is real if and only if its Fourier transform $f^{BA}(k\hat{\mathbf{r}},k\hat{\mathbf{r}}_{inc})$ is Hermitian i.e. $f^{BA}(k\hat{\mathbf{r}},k\hat{\mathbf{r}}_{inc})$ is equal to the transpose of its complex conjugate. The optical theorem suggests that [7]

$$-\frac{i}{2}\; f^{BA}(k\hat{\mathbf{r}},k\hat{\mathbf{r}}_{inc}) - \left[\, f^{BA}(k\hat{\mathbf{r}},k\hat{\mathbf{r}}_{inc})\right]^* = \mathrm{Im}[\, f^{BA}(k\hat{\mathbf{r}},k\hat{\mathbf{r}}_{inc})] \tag{3.10}$$

$$= \frac{k}{4\pi} \int_{\Omega\in H^2} d\Omega \left| f^{BA}(k\hat{\mathbf{r}},k\hat{\mathbf{r}}_{inc})\right|^2 = 0 \tag{3.11}$$

where Ω is the solid angle which is integrated over the unit sphere H^2 in the three dimensional space. Eq. 3.11 suggests that in order for the Born approximation to be valid, the only real scatterer that can exist should be zero everywhere i.e. it is not possible to find a real scattering object for which exact solutions for the scattered field satisfy the Born approximation. However for sufficiently small scattering objects with

negligible noise levels, one can get a consistent and stable estimate of V(**r**) by using a regularized inversion of Fourier data [7]. A simple and proven approach to do this is to modify the basis functions that represent V(**r**) from complex exponentials to weighted complex exponentials, such that the weights incorporate information about the object's shape or support. A closed form solution to the minimization of the squared error between the actual object and its estimate can be written and is known as PDFT [34]. I will be discussing the PDFT in later chapters.

Eq. 3.8 shows that the inverse Fourier transform of the complex far-field scattering amplitude gives us the scattering object. Inversion of scattered field data can be accomplished through two algorithms, namely Fourier based interpolation and filtered back propagation [1]. I will give a brief introduction to these two algorithms in forthcoming sections. When the Born approximation is not valid i.e. the scattering object has strong permittivity fluctuations, the Fourier inversions results in recovering $V_{BA}(\mathbf{r})$ instead of V(**r**)

$$V_{BA}(\mathbf{r},\hat{\mathbf{r}}_{inc}) \approx \mathrm{V}(\mathbf{r})\left\langle \frac{\Psi(\mathbf{r},\hat{\mathbf{r}}_{inc})}{\Psi_{inc}(\mathbf{r},\hat{\mathbf{r}}_{inc})} \right\rangle . \tag{3.12}$$

The symbol ≈ indicates that the reconstruction is an approximation since the Fourier transformation can only be taken for $\hat{\mathbf{r}}_{inc}$ = constant and limited data coverage will limit the accuracy. Also the symbol $\langle\ \rangle$ indicates an averaged dependence of the total field on the direction of incident plane wave. Given data from many illumination directions, a set of these Born reconstructed images can be generated, one for each illumination direction $\hat{\mathbf{r}}_{inc}$ and in which V(**r**) is common to each one of them but total field is different.

3.2.2 RYTOV APPROXIMATION (RA)

The Rytov approximation gives an alternative approach to linearizing the inverse scattering problem. The Rytov approximation represents the total field in terms of a complex phase [35] [1]

$$\Psi(\mathbf{r},\hat{\mathbf{r}}_{inc}) = \Psi_{inc}(\mathbf{r})e^{i\Phi_s(\mathbf{r})} \quad . \tag{3.13}$$

where $\Phi(\mathbf{r})= \Phi_{inc}(\mathbf{r}) + \Phi_s(\mathbf{r})$ is the complex phase function and $\Phi_s(\mathbf{r})$ is the phase function of scattered field. Substituting the total field from Eq. 3.13 into the inhomogeneous Helmholtz equation Eq. 2.4 and using identity

$$\nabla^2\left[\Psi_{inc}(\mathbf{r})\Phi_s(\mathbf{r})\right] = \left[\nabla^2\Psi_{inc}(\mathbf{r})\right]\Phi_s(\mathbf{r}) + 2\nabla\Psi_{inc}(\mathbf{r})\bullet\nabla\Phi_s(\mathbf{r}) + \left[\nabla^2\Phi_s(\mathbf{r})\right]\Psi_{inc}(\mathbf{r}) \tag{3.14}$$

the inhomogeneous Helmholtz equation becomes [7]

$$\nabla^2 + k^2\left[\Psi_{inc}(\mathbf{r})\Phi_s(\mathbf{r})\right] = i\,k^2V(\mathbf{r}) - \left[\nabla\Phi_s(\mathbf{r})\right]^2\Psi_{inc}(\mathbf{r}) . \tag{3.15}$$

Using the free-space Green's function, the complex phase function can be written as

$$\Phi_s(\mathbf{r}) = \frac{ik^2}{\Psi_{inc}(\mathbf{r})}\int_D V(\mathbf{r}')\Psi_{inc}(\mathbf{r}')G_o(\mathbf{r},\mathbf{r}')d\mathbf{r}' - \frac{i}{\Psi_{inc}(\mathbf{r})}\int_D\left[\nabla\Phi_s(\mathbf{r})\right]^2\Psi_{inc}(\mathbf{r}')G_o(\mathbf{r},\mathbf{r}')d\mathbf{r}' . \tag{3.16}$$

The second term in Eq. 3.16 can be ignored if the following inequality hold true [7]

$$\left|k^2\mathbf{V}(\mathbf{r})\right| \gg \left|\left[\nabla\Phi_s(\mathbf{r})\right]^2\right| \tag{3.17}$$

$$\left|\varepsilon(\mathbf{r}) - 1\right| \gg \left|\left[\frac{\lambda\nabla\Phi_s(\mathbf{r})}{2\pi}\right]^2\right| \tag{3.18}$$

The above inequality essentially requires that the incident wavelength be very small compared to the mean size of scattering inhomogeneities or the phase change induced by the scattering object per unit wavelength to be very small. The scattered field's phase, $\Phi_s(\mathbf{r})$, to a first approximation is linearly dependent on the permittivity of

scattering object. Eq. 3.18 is the local inequality which breaks down for V(**r**) = 0. A global condition for the Rytov approximation to be valid is written as

$$\left| k^2 \int_D \mathrm{V}(\mathbf{r}')\Psi_{inc}(\mathbf{r}')G_o(\mathbf{r},\mathbf{r}')d\mathbf{r}' \right| \gg \left| \int_D \left[\nabla\Phi_s \ \mathbf{r} \ \right]^2 \Psi_{inc}(\mathbf{r}')G_o(\mathbf{r},\mathbf{r}')d\mathbf{r}' \right|. \tag{3.19}$$

When the RA is valid then the complex scattered phase is

$$\Phi_s \ \mathbf{r} \ = \frac{ik^2}{\Psi_{inc}(\mathbf{r})} \int_D \mathrm{V}(\mathbf{r}')\Psi_{inc}(\mathbf{r}')G_o(\mathbf{r},\mathbf{r}')d\mathbf{r}'. \tag{3.20}$$

Substituting the value of scattered field's complex phase into Eq. 3.13 to compute total field

$$\Psi(\mathbf{r},\hat{\mathbf{r}}_{inc}) = \Psi_{inc}(\mathbf{r}) e^{\left[\frac{ik^2}{\Psi_{inc}(\mathbf{r})} \int_D \mathrm{V}(\mathbf{r}')\Psi_{inc}(\mathbf{r}')G_o(\mathbf{r},\mathbf{r}')d\mathbf{r}' \right]}. \tag{3.21}$$

Dividing the total field by incident field and taking its logarithm

$$\Psi_{inc}(\mathbf{r},\hat{\mathbf{r}}_{inc}) \ln\left[\frac{\Psi(\mathbf{r},\hat{\mathbf{r}}_{inc})}{\Psi_{inc}(\mathbf{r},\hat{\mathbf{r}}_{inc})} \right] = -k^2 \int_D \mathrm{V}(\mathbf{r}') e^{ik\hat{\mathbf{r}}_{inc}\bullet\mathbf{r}} G_o(\mathbf{r},\mathbf{r}')d\mathbf{r}'. \tag{3.22}$$

The above equation is very similar to Eq. 3.9 in the sense that with simple Fourier-inversion, we should be able to recover V(**r**). However the presence of the natural logarithm, which is a multi-valued function, makes it very difficult to solve for V(**r**) unless the right hand side of Eq. 3.22 is a continuous function. Ensuring this requires that the phase of the total field to be unwrapped prior to taking the logarithm. Phase unwrapping is very difficult in 2-D or higher dimensional problems because zeros in the field are associated with wave-front dislocations [53]. Phase unwrapping around these dislocations is not possible unless each dislocation is locally paired with one of opposite charge. Dislocations will permeate the function and these abrupt high spatial frequency

features will totally corrupt its Fourier transform. However, similar to the case of the first BA, when the RA is not valid, instead of recovering V(**r**) we recover $V_{RA}(\mathbf{r})$ where

$$V_{RA}(\mathbf{r},\hat{\mathbf{r}}_{inc}) = \mathrm{V}(\mathbf{r}) - \frac{1}{k^2}\left[\nabla\Phi_s \quad \mathbf{r} \quad\right]^2. \tag{3.23}$$

3.2.3 DISCUSSION ON BA AND RA

The BA and RA are applicable to a very small class of objects due to the fact that they either require object inhomogeneities to vary slowly on the scale of wavelength or the total phase shift introduced by the scatterer is less than 2π. In the case of the BA, both V(r) and V_{BA}(r) have zeros at same locations therefore, in principle; we get good recovery of the boundaries of objects. The same is not true for the RA therefore the RA does not recover voids and the shape of the object as accurately as BA. Slaney and Kak [1] [36] have shown that for small sized objects, the BA gives a better estimate of a scatterer as compared to the RA, as long as the phase shift induced in the incident field is less than π. For large objects with small permittivity fluctuations, the RA generates a more accurate estimate of scattering object. The RA is insensitive to the dimensions of the object. It has also been shown that for small objects and small permittivity variations, the BA and RA produce the same results [1] [36].

When using these two approximations, the distortion in the reconstruction for complicated objects can be significant due to some multiple scattering even for broadly weakly scattering objects. Kaveh and Soumekh [37] made the direct comparison between distortion effects of RA and BA. Sharp discontinuities in the object lead to large contributions from the second term in Eq. 3.16 and thus make the RA less valid. It

has been shown that the RA can be improved if scattering is largely in the forward direction [38].

3.3 INVERSION ALGORITHMS

There are two commonly used algorithms for the Fourier inversion of scattered field data: a) Fourier based interpolation, b) Filtered back propagation. Detailed discussion on these two methods can be found in [1]. In Fourier based interpolation, the scattered field data are placed onto semicircular arcs in the Fourier domain. These arcs are loci of points on the so-called Ewald circle [32] which is tangent to the origin of k-space and has radius of k. The scattered field transmission data lie on the part of arc tangent to the origin and reflection data lie farthest away from the origin Fig.3.1.

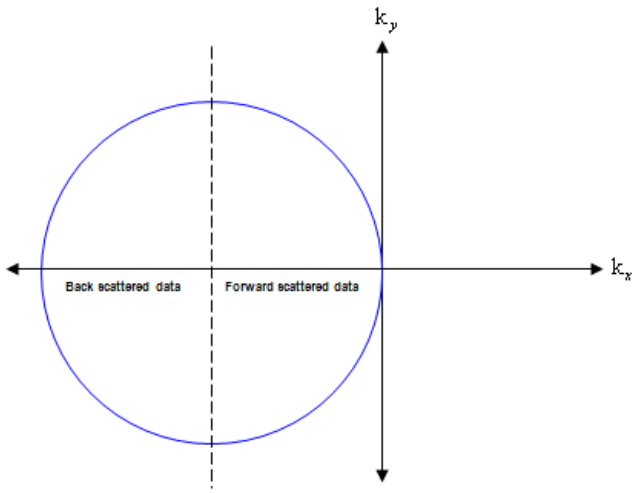

Figure. 3.1. k-map showing that the forward transmission data lies close to the origin and back scattered data lies away from the origin.

Scattered field data collected from one illumination angle $\hat{\mathbf{r}}_{inc}$ maps entirely onto an Ewald circle in that direction only. Therefore, if an object is illuminated from many

different directions, in principle, the corresponding data fills up the entire k-space, from which the scattering object can be reconstructed by a simple inverse Fourier transform Fig.3.2.

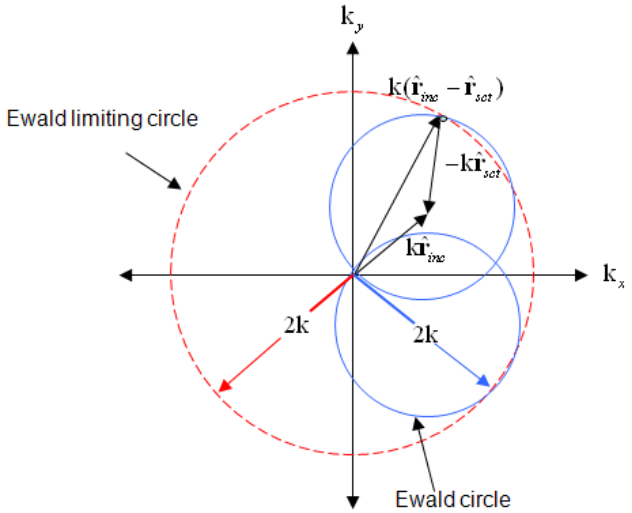

Figure. 3.2. Fourier space (k-space) of the object as a result of interaction of incident plane wave with scattering object. The direction of the incident field $\hat{\mathbf{r}}_{inc}$ and the direction $\hat{\mathbf{r}}_{sct}$ of a particular plane wave component of the scattered field define a point at the Ewald circle. Changing incident field directions $\hat{\mathbf{r}}_{inc}$ fills the interior of Ewald limiting circle.

With careful selection of the illumination direction and wavelength, it is possible to estimate the Fourier transform of the object at any given frequency. Changing the wavelength of the incident plane wave changes the radius of Ewald circle as illustrated in Fig.3.3

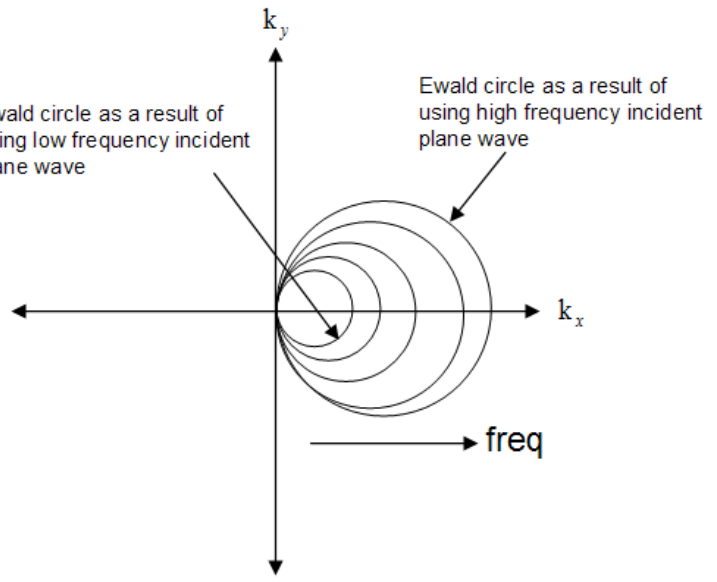

Figure. 3.3 Radius of Ewald circle increases by increasing the frequency of the incident plane wave.

In the filtered backpropagation method, the scattered field data are propagated backwards into the object domain using an appropriate Green's function [2] [7].

3.4 ITERATIVE INVERSE SCATTERING METHODS

Iterative techniques to solve the inverse scattering problem have gained tremendous attention in the past 20 years [12]-[15], [21], [27]-[31]. Several iterative methods have been proposed but only a few of them have achieved some level of success. I will briefly discuss the Born iterative method, distorted Born iterative method, and conjugate gradient method, which serve as the basis for many other iterative methods.

3.4.1 BORN ITERATIVE METHOD (BIM)

Wang and Chew proposed the Born iterative method [14]. The first Born approximation fails for strong scattering objects because of strong diffraction effects,

therefore the inherent nonlinearity of the integral equation (Eq. 3.2) has to be taken into account. The starting point of BIM is to first acquire an initial estimate, $V_{BA}^{1}(\mathbf{r})$, of the object by using the first Born approximation. The estimated $V_{BA}^{1}(\mathbf{r})$ is then used to compute the field inside the scattering volume and at the receiver points. The BIM uses a point matching method with the pulse basis function to solve the forward scattering problem [14]. The estimated field computed in the above step is substituted into Eq. 2.6

$$\Psi(\mathbf{r},\hat{\mathbf{r}}_{inc}) = \Psi_{inc}(\mathbf{r}) - k^2 \int_D \mathrm{V}(\mathbf{r}')\Psi(\mathbf{r}',\hat{\mathbf{r}}_{inc})G_o(\mathbf{r},\mathbf{r}')d\mathbf{r}' . \tag{3.24}$$

to calculate next order scattering function $V_{BA}^{2}(\mathbf{r})$. The second order scattering object $V_{BA}^{2}(\mathbf{r})$ is used to solve the scattering problem for the field inside the object and at the observation points. This simulated field $\Psi_s^{sim}(\mathbf{r},\hat{\mathbf{r}}_{inc})$ is then compared with the measured scattered field data $\Psi_s^{measured}(\mathbf{r},\hat{\mathbf{r}}_{inc})$

$$D = \left|\Psi_s^{sim}(\mathbf{r},\hat{\mathbf{r}}_{inc}) - \Psi_s^{measured}(\mathbf{r},\hat{\mathbf{r}}_{inc})\right| .$$

and if the difference between them is less than 5% then iteration can be terminated, otherwise one continues with the iterations. The BIM also uses a regularization method to address the non-uniqueness and instability of the inverse scattering problem. The regularization method imposes an additional constraint on the linear system and allows us to choose a solution from many available solutions. The Green's function remains unchanged during the entire iterative process. More details of the method can be found at [14].

3.4.2 DISTORTED BORN ITERATIVE METHOD (DBIM)

The Distorted Born iterative method was proposed by Wang and Chew [15] as an improvement over BIM [14]. Similar to BIM it starts by solving for the first order scattering object $V_{BA}^{1}(\mathbf{r})$ by using the first Born approximation and the homogeneous Green's function with relative permittivity of unity is used. The next step is to use this object function $V_{BA}^{1}(\mathbf{r})$ to solve the forward scattering problem using the method of moments [39] and to calculate the field inside the object and at the receiver points. Using $V_{BA}^{1}(\mathbf{r})$, the point source response in the object for every observation point is computed. In BIM the Green's function was kept constant throughout the iterative process, whereas in DBIM the Green's function $G_o^1(\mathbf{r},\mathbf{r}')$ is calculated with the last reconstructed permittivity profile as the background permittivity. The estimated Green's function and field are substituted in the integral equation

$$\Psi_s(\mathbf{r},\hat{\mathbf{r}}_{inc}) = -k^2 \int_D \mathrm{V}(\mathbf{r}')\Psi(\mathbf{r}',\hat{\mathbf{r}}_{inc})G_o(\mathbf{r},\mathbf{r}')d\mathbf{r}' . \tag{3.25}$$

The calculated scattered field is then subtracted from the field at receivers and the inverse scattering problem is solved for the correction of last reconstructed profile. Feedback from the previous profile is used to generate a new profile. The forward scattering problem is solved again using this new profile and the computed scattered field is compared with the measured scattered field. If the relative residual error (RRE) is less than the criterion defined then the process terminates; else it continues. Wang and Chew defined RRE as [14]

$$RRE = \frac{\sum_{a=1}^{M} \left| \Psi_s^{measured}(\mathbf{r}_a) - \Psi_s^{sim(j)}(\mathbf{r}_a) \right|}{\sum_{a=1}^{M} \left| \Psi_s^{measured}(\mathbf{r}_a) \right|}. \tag{3.26}$$

where j is the iteration cycle. The convergence rate of the distorted Born iterative method is faster than the Born iterative method. However the Born iterative method is more tolerant to noise than the distorted Born iterative method. Depending upon the nature of the problem we can either use BIM or DBIM.

3.4.2 CONJUGATE GRADIENT METHOD (CGM)

The conjugate gradient method [13] [41] is an iterative technique for solving the inverse scattering problem using an optimization procedure. In the conjugate gradient method a functional is defined as a norm of discrepancy between simulated scattered field amplitude and measured scattered field amplitude. Harada *et al.* defined this functional as [13]

$$X\ \mathrm{V}_{\mathrm{est}}(\mathbf{r}) = \sum_{m=1}^{M} \sum_{n=1}^{N} \left| f(\mathrm{V}_{\mathrm{est}}(\mathbf{r}); \phi_{inc}^{\ m}; \phi_s^{\ n}) - \tilde{f}(\phi_{inc}^{\ m}; \phi_s^{\ n}) \right|^2 \tag{3.27}$$

where f is the simulated scattered field amplitude which is calculated using an estimated object function $\mathrm{V}_{\mathrm{est}}\ \mathbf{r}$, $\tilde{f}$ is the measured scattered field amplitude and $X\left[\mathrm{V}\ \mathbf{r}\right]$ is the norm of difference between measured and simulated scattered field amplitude. The goal of the optimization method, which in this case is the conjugate gradient, is to find the ideal object function $\mathrm{V}_{\mathrm{est}}\ \mathbf{r}$ which minimizes the functional $X\left[\mathrm{V}\ \mathbf{r}\right]$. The gradient direction of the functional is found by using the

Fréchet derivative [13] [41] [42]. Similar to the Born iterative method, the forward scattering problem is solved using moment methods [39] with pulse basis functions and point matching, which transforms integral equations into matrix equations. The conjugate gradient method shows good immunity to noise levels and its convergence rate can be increased by using *a priori* information about the outer boundary of the object.

CHAPTER 4: SIGNAL PROCESSING BASED SOLUTION FOR INVERSE SCATTERING PROBLEMS

I propose here a simple signal processing based technique to solve the inverse scattering problem for objects with strong permittivity profiles. The starting point of this method is diffraction tomography for which inversion techniques are formulated as straightforward Fourier inversion procedures [7]. Complex scattered field data are collected at a number of scattering angles in the far field for each angle of illumination as shown in Fig.1.1. The scattered field data under these conditions, based on the first-order Born approximation are mapped onto the Ewald sphere in k-space [32] and with sufficient k-space coverage that can be inverse Fourier transformed to provide information about the scattering object, see Fig.3.2 and Fig.3.3. Physically this requires that the scattering from the object is extremely weak in order for the total field, everywhere within the object, to be well approximated by the incident field. The backpropagated image from the single scattering experiment can also be expressed as a convolution of scattering volume and point spread function of the imaging system [43]

$$V_{1-view}(\mathbf{r},\hat{\mathbf{r}}_{inc}) = \mathrm{V}(\mathbf{r}) ** \xi(\mathbf{r},\hat{\mathbf{r}}_{inc}) \tag{4.1}$$

where ** is the convolution in 2-D and $\xi(\mathbf{r},\hat{\mathbf{r}}_{inc})$ is the point spread function which for complete scattering experiment is the Fourier transform of Ewald circle. When the first Born approximation is not valid Eq. 4.1 becomes

$$V_{1-view}(\mathbf{r},\hat{\mathbf{r}}_{inc}) = V_{BA}(\mathbf{r}) ** \xi(\mathbf{r},\hat{\mathbf{r}}_{inc}) . \tag{4.2}$$

where $V_{BA}(\mathbf{r},\hat{\mathbf{r}}_{inc})$ is the secondary source or contrast source function written as

$$V_{BA}(\mathbf{r},\hat{\mathbf{r}}_{inc}) \approx \mathrm{V}(\mathbf{r})\left\langle \frac{\Psi(\mathbf{r},\hat{\mathbf{r}}_{inc})}{\Psi_{inc}(\mathbf{r},\hat{\mathbf{r}}_{inc})} \right\rangle. \tag{4.3}$$

In Eq. 4.3, V and Ψ are unknowns and Ψ_{inc} is the known quantity, which is the field in the absence of scattering object. The quality of the backpropagated image $V_{1-view}(\mathbf{r},\hat{\mathbf{r}}_{inc})$ depends upon the uniformity of the field inside the scatterer $\mathrm{V}(\mathbf{r})$. As the scattering strength increases and the object moves away from the first Born approximation, the multiple scattering components cause the field inside the object to become more complex and non-uniform. When the Born approximation is valid, then $\Psi(\mathbf{r},\hat{\mathbf{r}}_{inc}) \approx e^{ik\hat{\mathbf{r}}_{inc}\bullet\mathbf{r}}$ and $V_{BA}(\mathbf{r}) \approx \mathrm{V}(\mathbf{r})$, at least within low-pass spatial filtering effects resulting from the available k-space coverage.

The product in Eq. 4.3 is that of the total field, which obviously exhibits spatial fluctuations characteristic of the wavelengths being employed and the spatial distribution of the permittivity. For incremental wavelength changes, the field $\Psi(\mathbf{r},\hat{\mathbf{r}}_{inc})$ will change quite considerably but the permittivity need not in a low dispersion scattering distribution, V. In our approach we exploit the fact that the product, $\mathrm{V}(\mathbf{r})\Psi(\mathbf{r},\hat{\mathbf{r}}_{inc})$, retrieved following backpropagation can be separated using cepstral or homomorphic filtering assuming that the effect of point spread function can be ignored.

4.1 HOMOMORPHIC FILTERING

Changing the direction of illumination changes the secondary source function $V_{BA}(\mathbf{r},\hat{\mathbf{r}}_{inc})$, and a set of these single-view backpropagated reconstructions can be generated. We restate Eq. 4.3

$$V_{BA}(\mathbf{r},\hat{\mathbf{r}}_{inc}) \approx \mathrm{V}(\mathbf{r})\left\langle \frac{\Psi(\mathbf{r},\hat{\mathbf{r}}_{inc})}{\Psi_{inc}(\mathbf{r},\hat{\mathbf{r}}_{inc})} \right\rangle \tag{4.4}$$

where $\left\langle \Psi(\mathbf{r},\hat{\mathbf{r}}_{inc}) / \Psi_{inc}(\mathbf{r},\hat{\mathbf{r}}_{inc}) \right\rangle$ is a complex and noise-like term with a characteristic range of spatial frequencies dominated by the bandwidth of the source. The problem is now reduced to a complex filtering problem in which we want to get rid of the unwanted multiplicative noise term $\left\langle \Psi(\mathbf{r},\hat{\mathbf{r}}_{inc}) / \Psi_{inc}(\mathbf{r},\hat{\mathbf{r}}_{inc}) \right\rangle$. Homomorphic filtering converts a multiplicative modulation into additive one by taking the logarithm of the product. Taking the complex logarithm of Eq. 4.4 gives

$$\begin{aligned} &\log\ \mathrm{V}(\mathbf{r})\left\langle \Psi(\mathbf{r},\hat{\mathbf{r}}_{inc}) / \Psi_{inc}(\mathbf{r},\hat{\mathbf{r}}_{inc}) \right\rangle \\ &= \log\left|\mathrm{V}(\mathbf{r})\right| + \log\left|\left\langle \Psi(\mathbf{r},\hat{\mathbf{r}}_{inc}) / \Psi_{inc}(\mathbf{r},\hat{\mathbf{r}}_{inc}) \right\rangle\right| + i\left[\arg\ \mathrm{V}(\mathbf{r}) + \arg\ \left\langle \Psi(\mathbf{r},\hat{\mathbf{r}}_{inc}) / \Psi_{inc}(\mathbf{r},\hat{\mathbf{r}}_{inc}) \right\rangle\ \right]. \end{aligned} \tag{4.5}$$

The imaginary part of the logarithm represents the phase of the product which carries important information about the scattering object. Taking the Fourier transform of $\log\ \mathrm{V}(\mathbf{r})\left\langle \Psi(\mathbf{r},\hat{\mathbf{r}}_{inc}) / \Psi_{inc}(\mathbf{r},\hat{\mathbf{r}}_{inc}) \right\rangle$ gives the so-called "complex cepstrum" of the function [44] [45]. The complex cepstrum retains the phase information of complex data, which is useful for the meaningful filtering operation. Cepstral processing reduces the problem of convolution of two signals in the time domain to addition in the cepstral domain. Spatial filtering in the cepstral domain can separate information about V(**r**) from the product $\mathrm{V}\Psi$ and is known as homomorphic filtering. In the 2-D frequency

domain we can write the object and field as $\mathbf{V}\ \omega_1,\omega_2$ and $\mathbf{\Psi}\ \omega_1,\omega_2$. The complex cepstrum can be written as

$$\hat{g}\ x_1,x_2 = ifft\left[\log\ \mathbf{V}\ \omega_1,\omega_2\ \mathbf{\Psi}\ \omega_1,\omega_2\ \right] \tag{4.6}$$

$$= \frac{1}{2\pi}\int_{-\pi}^{\pi}\int_{-\pi}^{\pi}\left[\log\ \mathbf{V}\ \omega_1,\omega_2\ \mathbf{\Psi}\ \omega_1,\omega_2\ \right] e^{i2\pi\ \omega_1 x_1+\omega_2 x_2}\, d\omega_1 d\omega_2 . \tag{4.7}$$

Where *ifft* is the inverse fast Fourier transform. The complex cepstrum $\hat{g}\ x_1,x_2$ can be filtered to remove the unwanted noise term provided the field and object occupy distinct spatial frequencies in the cepstral domain. There are numerous numerical problems associated with performing $\log(V\Psi)$ and taking its Fourier transform. Aliasing of the cepstrum is a problem because of unwanted harmonics introduced by the complex logarithm in the cepstral domain [44]. The zero-padding of the input data sequence certainly helps in reducing the effect of aliasing; it also increases the sampling rate of the discrete Fourier transform. Care should be taken to ensure that the magnitude of $V\Psi$ does not go to zero else its logarithm becomes singular. Another problem in computing a complex cepstrum is due to the fact that the complex logarithm is multi-valued because of the uncertainty of 2π in its imaginary part. When the phase of $V\Psi$ has a range that exceeds 2π, the resulting wrapped phase introduces spurious spatial frequencies in the cepstrum. Phase unwrapping is exceedingly difficult, especially in two- and higher dimensional problems because of the zeros of a field leading to wave-front dislocations [48]. Modifications to homomorphic filtering, such as differential cepstral filtering have been developed [45], but here its effectiveness is shown when the data being processed satisfies the minimum phase condition.

4.2 MINIMUM PHASE BASED CEPSTRAL FILTERING

The concept of minimum phase is well understood in one-dimensional problems [47]. A one-dimensional signal *f (x)* is minimum phase if and only if its Fourier transform, *F*(*z*) has zero-free upper half plane, i.e. it has no zeros for $v > 0$ where $z = u + iv$.

$$F(u) = \int_{-\infty}^{+\infty} f(x) e^{i2\pi ux} dx \tag{4.8}$$

Some useful properties of minimum phase functions are [47]

i. *f (x)* is causal.

ii. The phase of *F(u)* lies between $-\pi$ and $+\pi$; i.e. their phase is always unwrapped (non-discontinuous).

iii. Most of the energy in *f(x)* lies close to origin.

iv. *F(u)* is absolutely summable.

The minimum phase function has a "minimum energy delay" property. As a result a minimum phase function possesses the highest partial energy among all the functions that have the same Fourier magnitude [52]. The function *f(x)* is minimum phase if its Fourier transform, *F(u)* is analytic and has a zero free half plane.

At this point it is important to discuss the concept of complex cepstrum. The complex cepstrum for a function *f* is calculated by finding the complex natural logarithm of the Fourier transform *F* of *f*, then the inverse Fourier transform (IFT) of the resulting function is

$$\hat{g} = ifft\left[\log\ F\right] \ where\ \ F = fft(f)$$

or we can also write it as

$$\hat{g}(x) = \frac{1}{2\pi} \int_{-\infty}^{+\infty} \log\ F(u)\ e^{i2\pi ux} du \tag{4.9}$$

where $\hat{g}$ is the cepstrum of the input signal *f*. In a one dimensional problem, the minimum phase condition is associated with the need to ensure that the Fourier transform of a causal function has a zero free upper half plane. This permits Cauchy's integral formula to be written to relate the Fourier magnitude and phase on the real u-axis, so-called logarithmic Hilbert transform pairs.

The meaning of a zero-free half plane in two dimensions is problematic since functions are typically 'irreducible' or non-factorizable i.e. their zeros are in the form of a single analytic curve. Creating a minimum phase function therefore requires preprocessing to remove all zeros from the upper half plane. Even for separable functions, where $F(u_1,u_2)=G(u_1)H(u_2)$, a zero-free upper-half plane in $G(z_1)$ automatically leads to $F(z_1, z_2)$ having zeros in the upper-half plane of z_2. For function $f(x)$ of compact support, $F(u)$ is a bandlimited function or equivalently, an entire function of exponential type and such functions having only real zeros. Functions having a zero-free half plane are rare in practice and few general conditions seem to be known for which these characteristics can be imposed.

Any Fourier-based theory of scattering or imaging involves fields that are analytic functions because scatterers or objects are of finite spatial extent. More precisely these fields are entire functions of exponential type [49] i.e. they satisfy Cauchy-Riemann equations for all finite z

$$\frac{\partial \operatorname{Re} F}{\partial x} = \frac{\partial \operatorname{Im} F}{\partial y} \tag{4.10}$$

$$\frac{\partial \operatorname{Re} F}{\partial y} = \frac{-\partial \operatorname{Im} F}{\partial x}. \tag{4.11}$$

This leads to strong constraints on how their amplitude grows and fluctuates and how their zero crossings are distributed. The properties of analytic functions of one complex variable are well known as compared to two or more variables. In 1-D, a bandlimited function behaves much like a polynomial and it can be represented by the location of its roots or zeros. For weak scattering objects each zero encodes a harmonic with phase and amplitude independent of the location of other zeros. The Hadamard product represents the function in terms of the locations of its zeros which are isolated points. Asymptotically, these zeros must be distributed uniformly, in a manner determined by the behavior of the function's Fourier transform near the edges of its support. Since the Fourier transform of a function of compact support is analytic or more precisely an entire function of exponential type, there are rigid constraints on how the real and imaginary parts and hence the magnitude and phase of such functions can behave.

4.3 GENERATING THE MINIMUM PHASE FUNCTION

Dudgeon and Mersereau [47] state that a two-dimensional minimum phase function is one that is absolutely summable and one whose inverse and complex cepstrum are absolutely summable and have the same region of support. This region of support also has to be a convex region of some kind. It has not been possible to find general properties for classes of functions for which these conditions can be satisfied and this condition appears to be sufficient but not necessary. Some specific examples exist of well-conditioned cepstra, as a result of the incorporation of a background or reference wave on the function whose logarithm is to be Fourier transformed. Taking

the logarithm of a bandlimited function produces a bandlimited function and hence a cepstrum of finite support only for minimum phase functions.

At this point, a brief digression on dispersion relations may be helpful. It is well known that the real and imaginary parts of the Fourier transform of a causal function *f(x)* are related to each other by a Hilbert transform. This follows directly from Titchmarsh's theorem [51] and is a consequence of the finite support or causal nature of the Fourier transform. The Hilbert transform, HT, is an integral transform that is a principal value integral which is implicitly solved as a contour integral. The contour is the real axis and a semicircle in either the upper or lower half of the complex plane which, if Jordan's lemma is satisfied, can be ignored. The HT relationship then takes the form

$$\mathrm{Im}\left[F\ \ u\ \right] = \frac{1}{\pi} P \int_{-\infty}^{+\infty} \frac{\mathrm{Re}\left[F\ \ u' \right]}{u' - u}\, du' \tag{4.10}$$

$$\mathrm{Re}\left[F\ \ u\ \right] = -\frac{1}{\pi} P \int_{-\infty}^{+\infty} \frac{\mathrm{Im}\left[f\ \ u' \right]}{u' - u}\, du' \tag{4.11}$$

where *P* is the Cauchy principal value. Closure of the contour without contributions to the value of the integral from residues is necessary and so the real and imaginary parts of log[*F(u)*] can be similarly related, provided *F* has no zeros within the contour of integration. This statement also defines the minimum phase condition. Function *F* can be written in terms of magnitude and phase as

$$F = |F| e^{i\phi} \tag{4.12}$$

Taking the complex logarithm of Eq. 4.12 yields

$$\log\ F\ = \log|F| + i\phi \tag{4.13}$$

where log|*F*| is the real part and ϕ is the imaginary part. One can compute the phase of *F*

$$\mathrm{Im}\left[\log F\ \ u\ \right] = \frac{1}{\pi} P \int_{-\infty}^{+\infty} \frac{\mathrm{Re}\left[\log F\ \ u'\ \right]}{u' - u}\, du' . \tag{4.14}$$

The above integral only works if *F* has no zeros in the upper half plane. If *F* is not a minimum phase function, then the result of the above integral will be to produce a phase which, when applied to |*F*| generates a minimum phase function. An important feature of a minimum phase function is that the phase is a continuous function bounded between −π and π and 'minimum' in this sense can be interpreted to mean that the phase is already unwrapped. Using this property of minimum phase functions we can execute the step defined in Eq. 4.5 in a satisfactory fashion.

In the one dimensional problem, it is possible to enforce the minimum phase condition on a function by applying Rouche's theorem [49]. A 2-D version of Rouche's theorem has been validated in [46]. Suppose *h =F(z)* is analytic in a domain D where *F =(F*$_1$*, F*$_2$*, . . . , F*$_N$*)* and the boundary of D is smooth and contains no zeros of *F*, then if for each point *z* on the boundary, there is at least one index *j (j = 1, 2, . . . , N)* such that | *F*$_j$*(z)*| > |*G*$_j$*(z)*| then *G(z) + F(z)* have the same number of zeros in D as the number of zeros in *F(z)* (it actually suffices that *Re{ G*$_j$ *(z)} < Re{ F*$_j$*(z)})*. In other words; if a function

A has N number of zeros

B has M number of zeros

and

|*A*| > |*B*| on same contour

then

$A + B$ will have N number of zeros in that contour contrary for $|A| < |B|$, $A+B$ will have M number of zeros. See Fig. 4.1. The sum of the two functions will have the number of zeros equal to the number of zeros of the larger magnitude function. Consequently, adding a sufficiently large background or reference wave to a bandlimited function, A, where we assume $|A|<<1$, allows us to write $G = 1 + A \sim \exp(A)$ thereby satisfying this minimum phase condition.

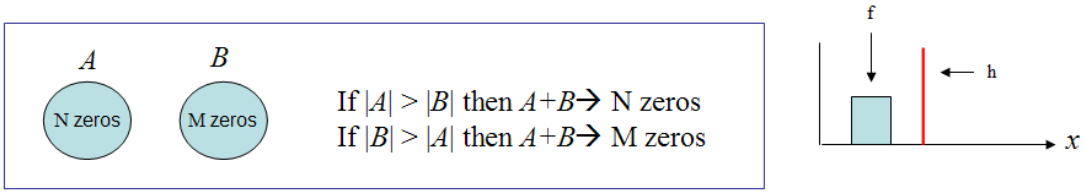

Figure. 4.1. Shows the pictorial description of Rouche's theorem.

Therefore, if, to our bandlimited function *F(z)*, we add another function *G(z)* which we refer to as a reference function and *G(z)* has no zeros in upper half plane, then the function *F(z)+G(z)* will have no zeros in upper half plane, thus satisfying Rouche's theorem and the minimum phase condition. The addition of a reference function to an analytic function only moves the zeros from upper half plane to lower half plane without destroying them [49]. If a reference function is chosen as a constant then we can always find a contour in the upper half plane along which the magnitude of the added function is greater than the magnitude of *F(z)*. Increasing the constant moves the contour across the real axis and thus pushing zeros to the lower half plane [49]. It therefore follows that one can preprocess by adding a finite constant or reference point to make it minimum phase before taking its logarithm.

4.4 PREPROCESSING DATA

The preprocessing step requires the data available in k-space to be made causal, $V\langle\Psi\rangle_c$. This can be done by moving available scattered field data into one quadrant of k-space i.e. data is nonzero only in one quadrant as shown in Fig. 4.2.

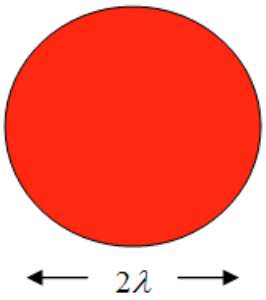

(a)

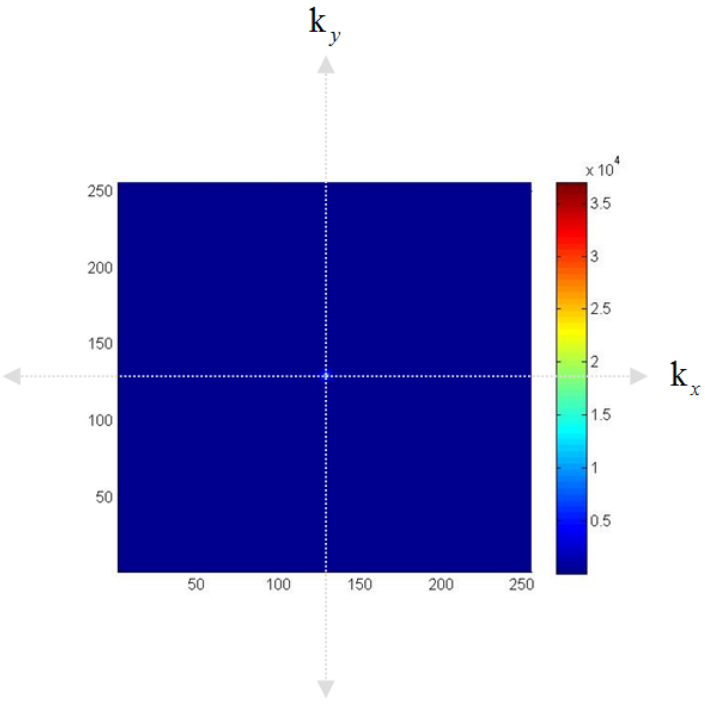

(b)

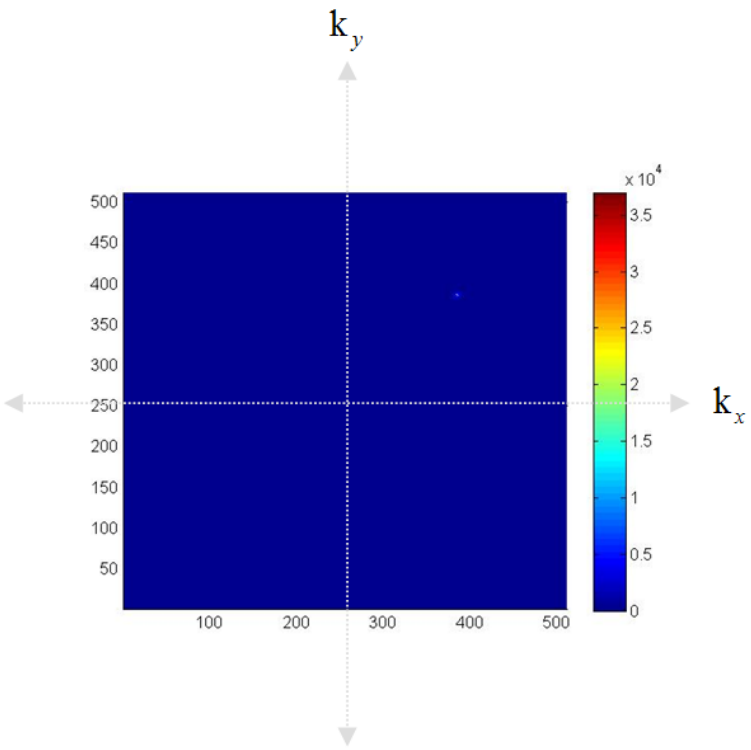

(c)

Figure. 4.2 Scattering cylinder – k-space data: (a) Cylinder with 2λ diameter, (b) unprocessed $V(\mathbf{r})\langle\Psi(\mathbf{r},\hat{\mathbf{r}}_{inc})\rangle$ in k-space, (c) Data is made causal by moving it into one quadrant.

The next step is to add a reference point at the origin of the causal data $V\langle\Psi\rangle_c$ in k-space. This corresponds to adding a linear phase factor to VΨ in the object domain. In order to satisfy the minimum phase condition the reference point *R* does not need to have an arbitrarily large amplitude (a sufficient condition), but simply be just large enough to ensure that phase of VΨ is continuous and lies within the bounds of $-\pi$ and $+\pi$. A very large reference point with amplitude *R* such that $\left|V\langle\Psi\rangle\right|/R \gg 1$ leads to the Fourier transform of $\log(R+V\langle\Psi\rangle) \longrightarrow \log(1+V\langle\Psi\rangle/R)$ being approximately equal to $V\langle\Psi\rangle/R$ indicating that we have satisfied the minimum phase condition but we have

not provided a function of $V\langle\Psi\rangle$ that will result in successful filtering in the cepstral domain. In this case, the cepstrum of $V\langle\Psi\rangle$ contains the same information that we originally had in k-space. This corresponds to $R = 0$ and the unwanted harmonics in the cepstrum makes filtering impossible. The optimal choice of R is an amplitude which is just large enough to ensure that the phase of $V\langle\Psi\rangle$ is unwrapped and lies between $-\pi$ and $+\pi$. It has been shown [48] [53] that in order to enforce a minimum phase condition the reference should satisfy

$$R \geq \left|V\langle\Psi\rangle\right|_{\max} \tag{4.15}$$

i.e. the reference point needs to be larger than the maximum value of the scattered field amplitude to satisfy Rouche's theorem. I found the inequality given in Eq. 4.15 to be a sufficient condition to enforce minimum phase condition. In the forward scattering problem, this is intuitively satisfying since it is equivalent to requiring that the scattering is relatively weak compared to a larger amplitude background or incident plane wave, as demanded by the first Born approximation. The analogy with holography is also immediate since interference with a reference wave, especially when off-axis with respect to the scattered field, ensures the phase of the scattered field is encoded in the magnitude via a logarithmic Hilbert transform. An important point however is that if one can compute a good estimate for $V\langle\Psi\rangle$ from measured data, then one could numerically add in this reference wave prior to homomorphic filtering. It becomes a post-data processing step and not an experimental requirement.

In order to choose an appropriate reference point the starting point is to make the amplitude of the reference point the same as the maximum amplitude of $V\langle\Psi\rangle$ and then

systematically increase its amplitude until the phase of Born reconstructed $V\langle\Psi\rangle$ lies between $-\pi$ and $+\pi$. Fig4.3 shows the result of this procedure applied to a cylinder of radius 1λ.

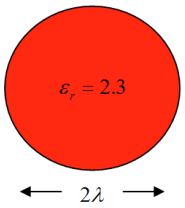

(a)

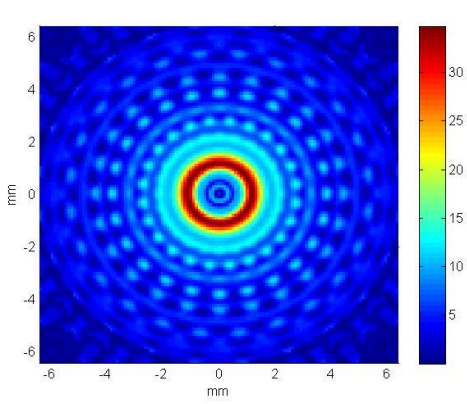

(b)

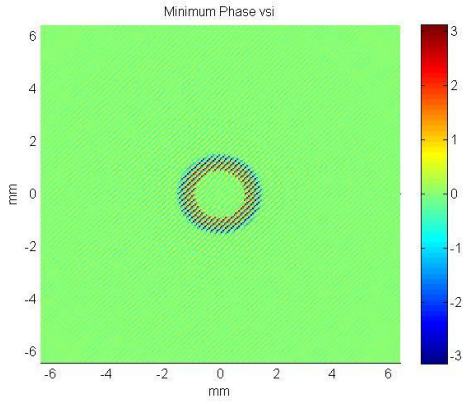

(c)

Figure 4.3 Scattering cylinder: (a) Cylinder with 2λ diameter and relative permittivity of 2.3, (b) Born reconstruction, (c) Minimum phase after adding a suitable reference point

This value for *R* permits us to write

$$\log(R + V\langle\Psi\rangle) \longrightarrow \log(1 + \frac{V\langle\Psi\rangle}{R}) \sim \frac{V\langle\Psi\rangle}{R} - \frac{1}{2}\left(\frac{V\langle\Psi\rangle}{R}\right)^2 + \ldots \qquad (4.16)$$

or one could also write

$$\log(1 + \frac{V\langle\Psi\rangle}{R}) = \log\left(\left\{\frac{V}{R}\right\}\left\{\frac{R}{V} + \langle\Psi\rangle\right\}\right) = \log\left(\frac{V}{R}\right) + \log\left(\frac{R}{V} + \langle\Psi\rangle\right) \qquad (4.17)$$

$$\approx \log\left(\frac{\mathrm{V}}{R}\right) + \log\ R' + \langle\Psi\rangle$$

$$\approx \log\left(\frac{\mathrm{V}}{R}\right) + \frac{\langle\Psi\rangle}{R'} \tag{4.18}$$

The second term in Eq. 4.18 contains spatial frequencies which are similar to the spatial frequencies of field. One can vary the frequency of the incident plane wave to determine the spatial frequency characteristics of the second term in Eq. 4.18 whereas log (V/*R*) should stay the same. The implementation of the cepstral filtering requires that a low pass filter be applied until the wavelike structure associated with $\langle\Psi\rangle$ is removed. The success of the filtering operation depends upon how distinct the spatial frequencies of $\langle\Psi\rangle / R'$ are from spatial frequencies of $\log\ \mathrm{V}/R$. A linear combination of estimates for V acquired in this way will further improve the signal to noise ratio (SNR) of the reconstructed V while suppressing any residual components from the Fourier transform in each of these images.

4.5 TWO DIMENSIONAL FILTERING

The choice of filter depends upon the spatial frequency characteristics of log(V/R) and $\langle\Psi\rangle / R'$. A simple low pass filter, Fig. 4.4, should work for a large class of objects as $\langle\Psi\rangle / R'$, which is influenced by the frequency of illumination wave, possess high spatial frequencies and simple scattering objects, V, usually occupy low the frequency regime.

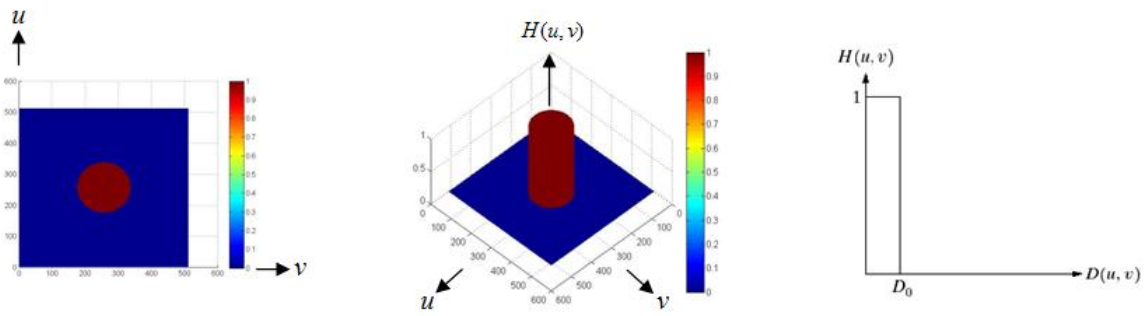

(a) (b) (c)

Figure. 4.4 Low pass filter (a) ideal hard-cut low pass filter 2D view, (b) low pass filter displayed in 3D, (c) cross section of ideal low pass filter

I have found that a Gaussian cepstral filter, Fig.4.5, being apodized, is preferable to a circular or square hard-cut filter.

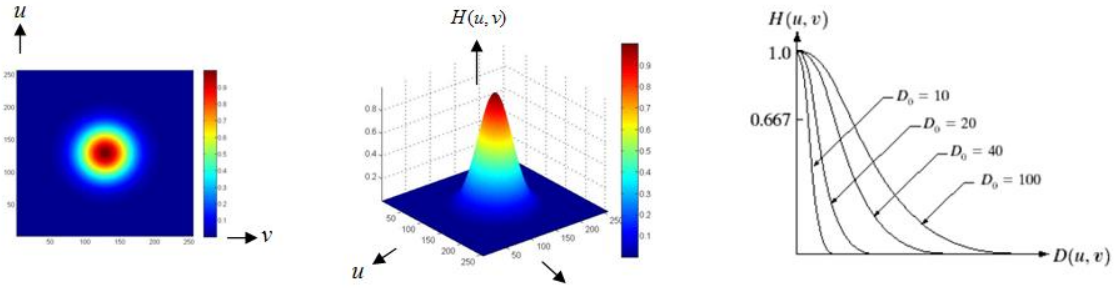

(a) (b) (c)

Figure. 4.5 Gaussian low pass filter (a) Gaussian low pass filter 2D view, (b) Gaussian low pass filter displayed in 3D, (c) Cross section of Gaussian low pass filter

Using an ideal hard-cut filter can result in unwanted ringing in the reconstruction. Smoothing the filter also helps in improving SNR by cutting off the high frequency gently. Fig.4.6 shows the effect of a hard-cut filter versus a smoothed filter like Gaussian.

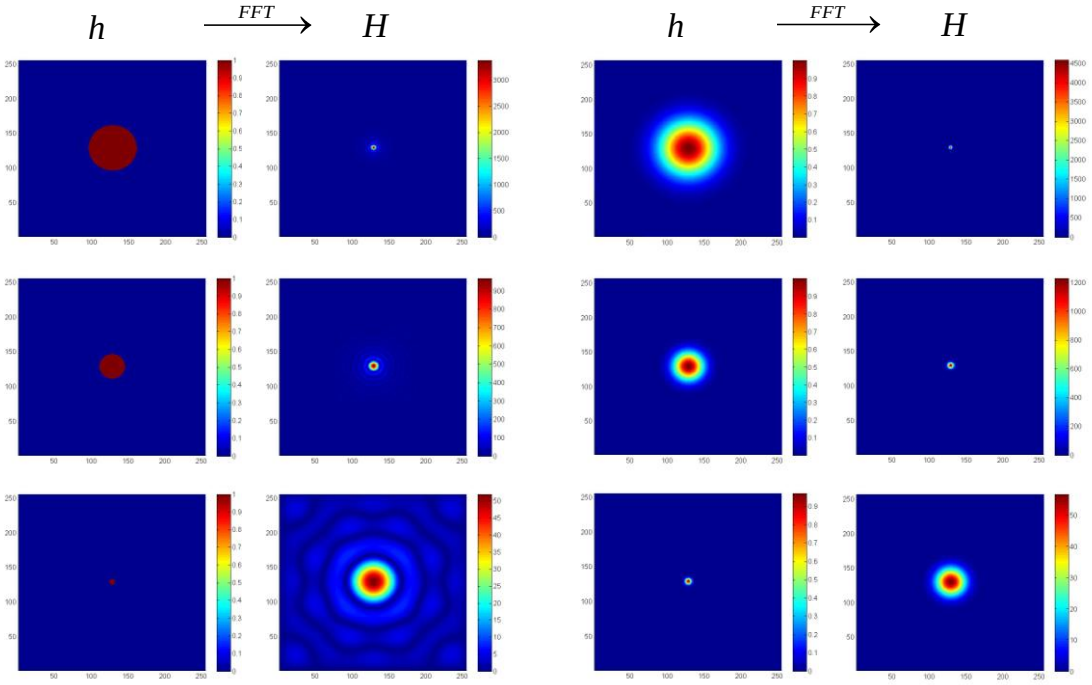

(a) (b)

Figure. 4.6 Hard-cut filter vs. smoothed filter – effect of ringing (a) Ideal 2D circular hard-cut filter and its frequency spectrum, (b) 2D Gaussian low pass filter and its frequency spectrum

CHAPTER 5: EXPERIMENTAL RESULTS AND DISCUSSION

In this section the proposed method is applied to real data provided by various groups. The US Air Force Research Laboratory's (AFRL) initiated the idea that it would be healthy for the inverse scattering community to test their algorithms on measured data from unknown targets. They conducted a number of scattering experiments and provided scattered field data, known as Ipswich data, in the mid-1990s [54]-[57] and which has still kept the community busy since then. More recent data sets have been the focus of special issues of journals such as Inverse Problems using data provide by the Institut Fresnel [58]. Also I have applied the proposed method on analytic data to study the effect of sampling on the inverse scattering problem.

5.1 IPSWICH DATA

The AFRL collected Ipswich data in an anechoic chamber, using the swept-bistatic system described in [59]. Fig.5.1 (taken from [54]) shows the layout of the measurement system, and defines the angles used to describe the data.

5.1.1 IPS008

I performed the minimum phase procedure on Ipswich data sets IPS008 and IPS0010, the strong scatterers. The IPS008 consisted of two cylinders, the outer cylinder is filled with sand and the inner cylinder is filled with salt. The cylinder was

placed far enough from the source to ensure that the illuminating wave was well approximated by a plane wave.

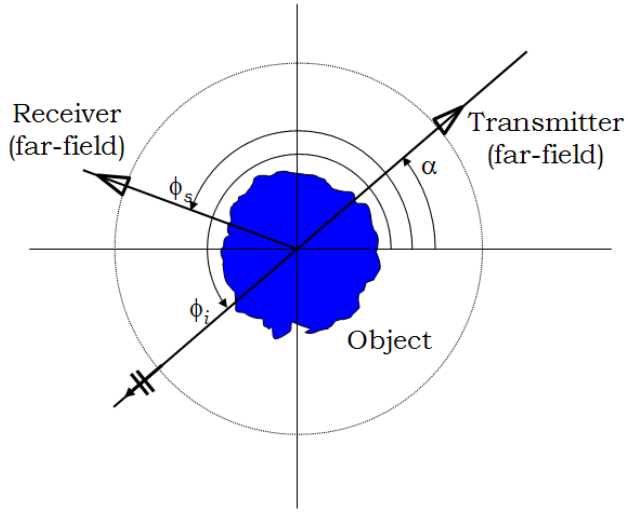

Figure. 5.1. Ipswich scattering experiment where α is angle of incidence, $\phi_s$is scattering angle and ϕ_i gives illuminating direction.

The measured and limited data consisted of 36 illumination directions, at equal angular separations of 10 degrees and 180 complex scattered field measurements for each view angle using a frequency of 10GHz. These data were located on arcs in k-space and moved into one quadrant to impose causality. The IPS008 object represents a strongly scattering penetrable object and has proved the most difficult to recover from its scattered field data [54]. The geometry of IPS008 is shown in Fig. 5.2 and alongside it, the best image one could expect from the available scattered field measurements, assuming only an inverse Fourier transform is necessary over the loci of data circles in k-space.

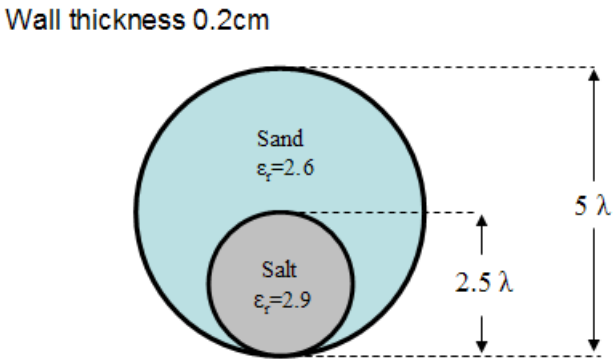

(a)

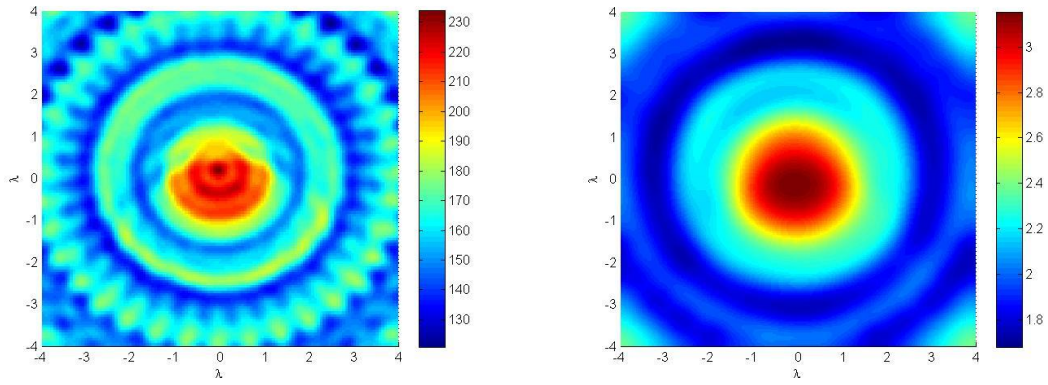

(b) (c)

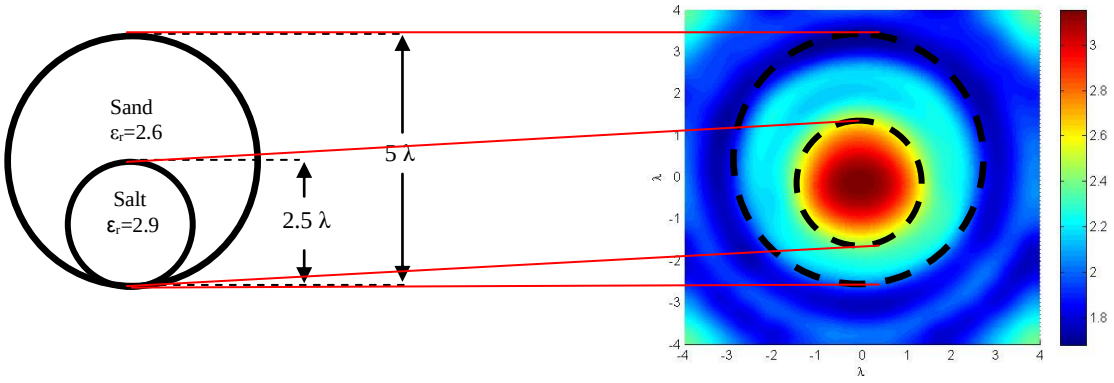

(d)

Figure. 5.2. IPS008 target configuration: (a) Target object IPS008 geometry, (b) Born reconstruction, (c) Cepstral reconstruction, (d) Geometrical comparison between reconstructed object and original object.

Fig.5.2 shows a reconstruction from the nonlinear filtering method. The reference point, *R*, introduced at the origin in k-space was increased until the phase of $V(\mathbf{r})\langle\Psi(\mathbf{r},\hat{\mathbf{r}})\rangle$ lies between ± π. A Gaussian low pass filter was then applied until all wave-like features had been eliminated from the resulting reconstruction of the object, V. The Ipswich008 target is a strong scattering object as $k|V|a \approx 87$ where k, wave number, is calculated as $k=2\pi/\lambda = 2\pi/0.03 = 209.5$, V is the scattering strength or average permittivity and 'a' is the dimension of the largest feature of object. IPS008 has proved to be a challenging object to image for all of the inverse scattering community as most of the algorithms applied were based on the first Born approximation and clearly the image obtained using the Born approximation shows poor reconstruction, Fig.5.2(b). When an incident plane wave impinges on IPS008 it gets diffracted at the boundary of the larger cylinder. As a result the wave which is incident on the smaller cylinder can be interpreted as a convergent wavefront. This constitutes a serious violation of the first order Born approximation, which assumes the incident field to pass the target essentially unperturbed, as a result of which we see artifacts in the reconstruction as shown in Fig.5.2(b). Fig.5.2(c) shows the reconstruction obtained using the proposed method. The image of Fig.5.2(c) looks much better as compared with an estimate using the Born approximation. The step by step process of recovering a scattering object using cepstral filtering method is shown in Fig.5.3. It not only gives an improved estimate of the shape of object but also provides a good approximation of the permittivity distribution. The cepstral filtering method did a good job in recovering the dimensions of cylinders however the recovered inner cylinder is not tangent to the external one, as it should be.

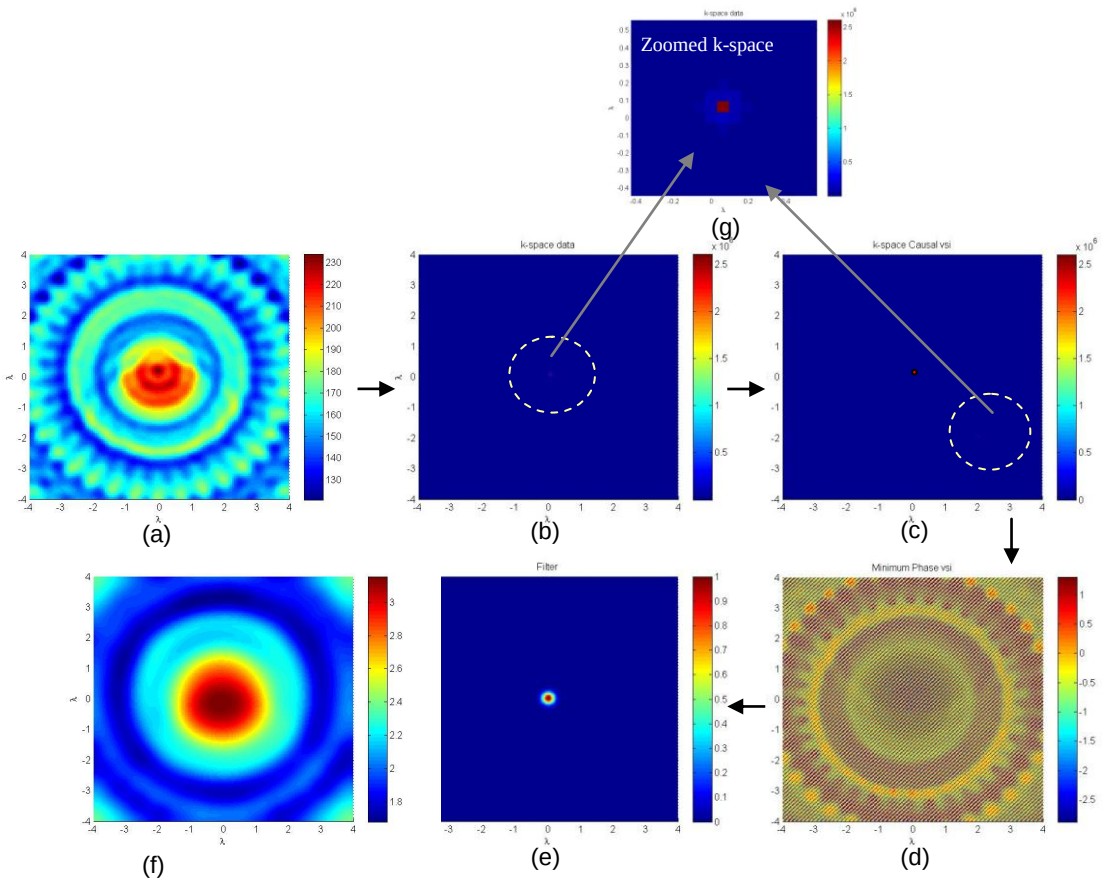

Figure. 5.3. Cepstral inversion steps: (a) Born reconstruction, (b) k-space data, (c) Causal k-space data with reference added at origin, (d) Minimum phase V<Ψ>, (e) Gaussian filter, (f) Cepstral reconstruction, (g) zoomed k-space data

I believe that this difference in position of inner cylinder is due to the limited data coverage and later I will show that the spectral estimation technique, PDFT, helps in resolving this position offset.

Fig.5.4 shows the comparison of reconstructed IPS008 object from various inverse scattering groups published in IEEE Antennas and Propagation Magazine [60] [68]- [69] and a minimum phase based reconstruction.

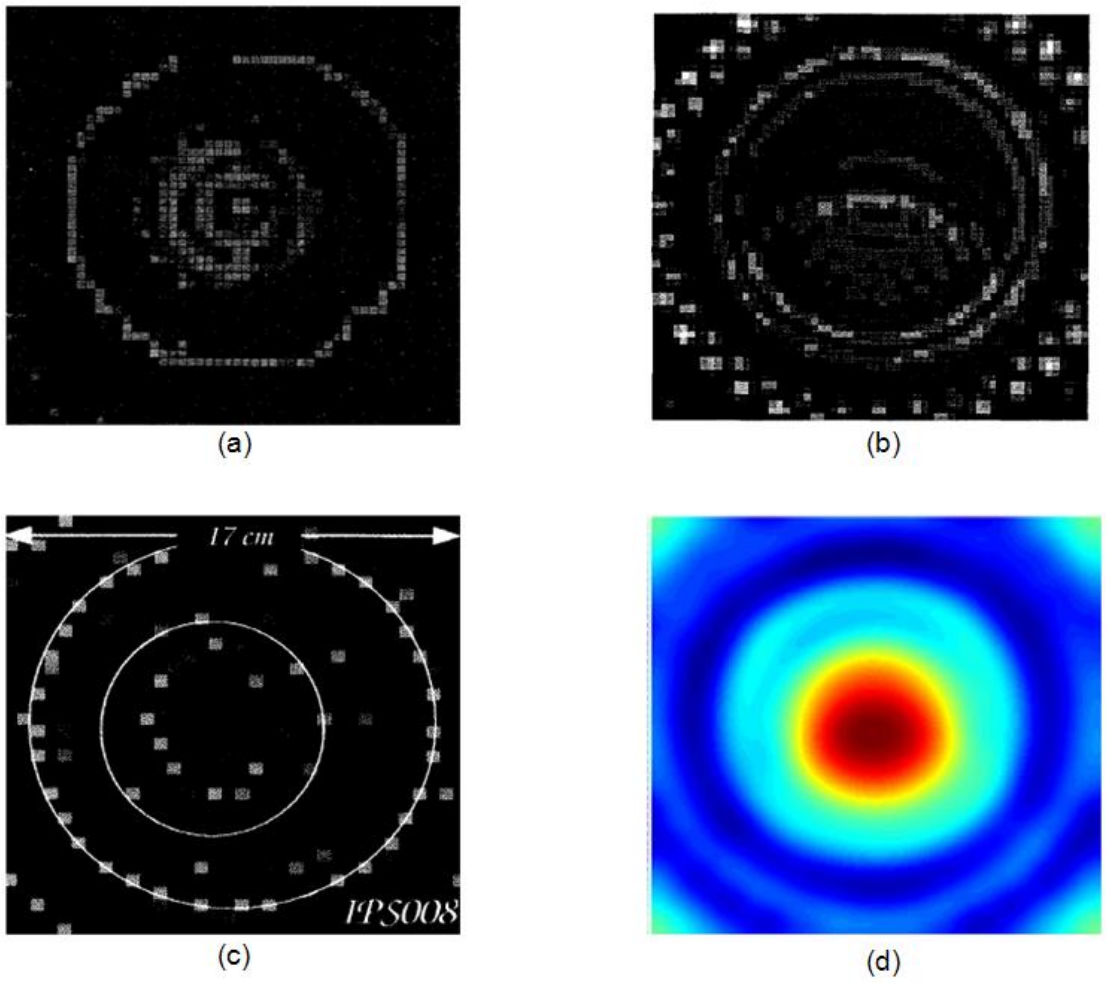

Figure. 5.4. IPS008 reconstructions: (a) Reconstruction taken from reference [60], (b) Reconstruction taken from reference [68], (c) Reconstruction taken from reference [69], (d) Cepstral reconstruction

5.1.2 IPS010

The IPS010 is a dielectric wedge made of Plexiglass with relative permittivity $\varepsilon_r \approx 2.25$. The IPS010 proved to be a very challenging object for participating groups due to its high permittivity and sharp shape features. Fig.5.5 shows the Born reconstruction and cepstral reconstruction.

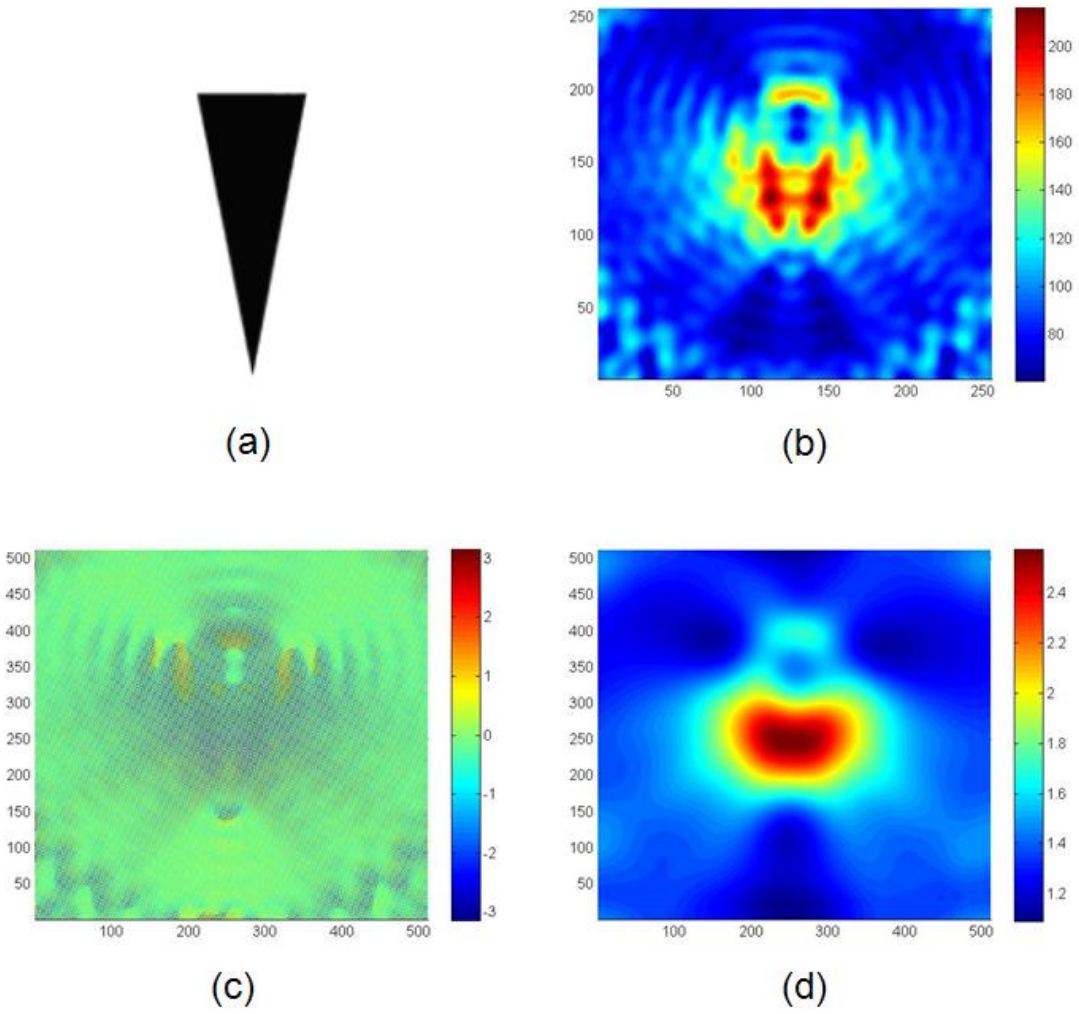

Figure. 5.5. IPS010 target configuration: (a) Target object IPS010 geometry, (b) Born reconstruction, (c) Minimum phase, (d) cepstral reconstruction

Combination of the wedge shape and high permittivity has made this object very difficult to image. The cepstral method did a reasonable job in recovering the quantitative description of IPS010, however shape estimation is still poor both in the Born and cepstral methods. One reason for this poor shape could be the insufficient sampling rate. The same number of illumination angles which are used to reconstruct simple cylindrical objects may not be sufficient to reconstruct a wedge shaped object with sharp features, as I will discuss later.

5.2 THE PRIOR DISCRETE FOURIER TRANSFORM (PDFT)

In practice, the analyticity of the estimate for $V\Psi$ is assured because of the fact that the data available are always limited in k-space. However, processing this assumes a good estimate of the separable function $V\Psi$ since it is necessary to separate V from Ψ. Since V is assumed to be of finite extent, then $\mathbf{V}\Psi$ should also be of compact support and hence the data in k-space should be analytic. In principle, one may use analytical continuation of the scattered field data in k-space to obtain a better estimate of $V\Psi$ as a product rather than a low pass filtered and hence bandlimited function. However it has been observed by several authors [79]-[81] that analytic continuation is not practical because of its instability and sensitivity to noise. The inverse scattering algorithms are Fourier based in nature and improvement in the image quality of the recovered object can be accomplished by interpolating and extrapolating the Fourier data lying on semi circular arcs in k-space.

I have adopted a very stable (regularizable) spectral estimation method known as the PDFT [34] [61] - [64], which gives a minimum norm solution of the estimate for $V\Psi$ using properly designed Hilbert spaces. The success of the PDFT algorithm relies on its flexibility and effective encoding of prior knowledge about the object. The PDFT is a Fourier based estimator so it is easy to incorporate it in our signal processing method. The details of the PDFT algorithm can be found in [61]-[64] but in summary the PDFT assumes that Fourier information about the product of $V\Psi$ is available, which is precisely our measured data in k-space. Let

$$f(\mathbf{r}) = V(\mathbf{r})\Psi(\mathbf{r}) \tag{5.1}$$

then the Fourier transform of $f(\mathbf{r})$ is written as

$$F_n = F(\mathbf{k}_n) = \int_{-\infty}^{\infty}\int_{-\infty}^{\infty} f(\mathbf{r}) e^{-i\mathbf{k}_n \mathbf{r}} d^2\mathbf{r} \tag{5.2}$$

for n=1,2,3…N. The PDFT estimator is given by

$$f_{PDFT} = p(\mathbf{r}) \sum_{m=1}^{M} a_m e^{i\mathbf{k}_m \mathbf{r}} \tag{5.3}$$

where *p(***r***)* is the non-negative prior weighting function which contains information about the object. The advantage of the PDFT algorithm is that the data need not to be uniformly sampled which is why this approach can be used to interpolate and extrapolate both nonuniformly sampled and an incomplete data set. The term PDFT comes from the fact that it's the product of a prior *p(***r***)* and the discrete Fourier transform. The coefficients a_m for m = 1, 2, 3,…, M are determined by solving a system of linear equations,

$$F_n = \sum_{m=1}^{M} a_m P(\mathbf{k}_n - \mathbf{k}_m). \tag{5.4}$$

In matrix notation we can write above equation as

$$\mathbf{f} = \mathbf{Pa} \tag{5.5}$$

where

$$\mathbf{f} = [F(\mathbf{k}_1), F(\mathbf{k}_2), ..., F(\mathbf{k}_M)]^T \tag{5.6}$$

$$\mathbf{a} = \left[a_1, a_2, ..., a_M\right]^T \tag{5.7}$$

and where *T* denotes the transpose of matrix and P is the MxM square matrix and it is the Fourier transform of prior *p(***r***).* Thus using the coefficients calculated by solving the above set of equations the PDFT provides a data consistent image estimate by minimizing the weighted error

$$\xi = \int \frac{1}{p(\mathbf{r})} \left| f(\mathbf{r}) - f_{PDFT}(\mathbf{r}) \right| d^2\mathbf{r} = \min . \tag{5.8}$$

The above integral is taken over the support of the prior function *p(***r***)* which contains the information about the true or estimated support of the object. The computation of P can be made even if the prior is not available in closed form but is estimated as a surrounding shape since matrix elements can be readily computed. There are also challenges associated with Fourier data being noisy and a method of regularization needs to be employed. If the prior is chosen such that the object energy lies outside the prior support, then without any method of regularization this will lead to spurious oscillations in the estimate of the object function because the PDFT is data consistent and requires a lot of energy in the extrapolated spectral values to accommodate an underestimated support. To address this problem the Miller-Tikhonov regularization is used, which helps in removing the ill-conditioning of the P-matrix by adding a small number to the diagonal elements of the P-matrix [66]. This is equivalent to adding a small constant amplitude outside the prior support. The regularization step essentially reduces the energy in the estimate arising from the unstable eigenvalues by adding a small value into the prior function (i.e. not allowing it to be zero outside of the support) to slightly increase all eigenvalues without altering the eigenvectors.

If no prior knowledge is available then *p(***r***)* would be a constant and the estimator reduces to the DFT of the available Fourier data. Also when the regularization constant τ is very large such that

$$1 + \tau \approx \tau$$

the estimator essentially looks like the DFT. The PDFT estimator is both data consistent and continuous and works in any number of spatial dimensions version [67]. The result

is shown in Fig.5.6 for the case when the PDFT is used instead of the DFT to reconstruct IPS008.

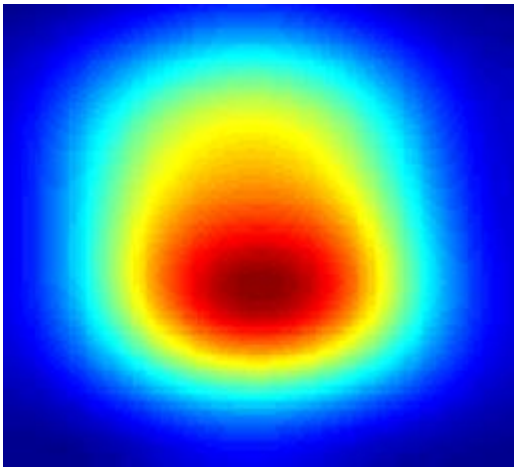

Figure. 5.6. IPS008 cepstral reconstruction using PDFT

I also applied the PDFT algorithm to IPS010 to improve reconstruction quality. It is important to know the location of the object in order to distinguish between target and artifacts. I can get rid of unwanted signal components by carefully choosing *a prior* to encompass V as tightly as one can reasonably estimate without cutting in to the actual dimensions of V. Actually, if one did, the energy of the PDFT estimate would become very large and one can use this as a means to "shape" or determine the perimeter of an unknown V. For IPS010 I investigated various prior functions. I found that the best reconstruction was obtained when a rectangular prior was chosen centered on the center of wedge. Fig.5.7 shows the prior and resulting PDFT estimate of ISP010.

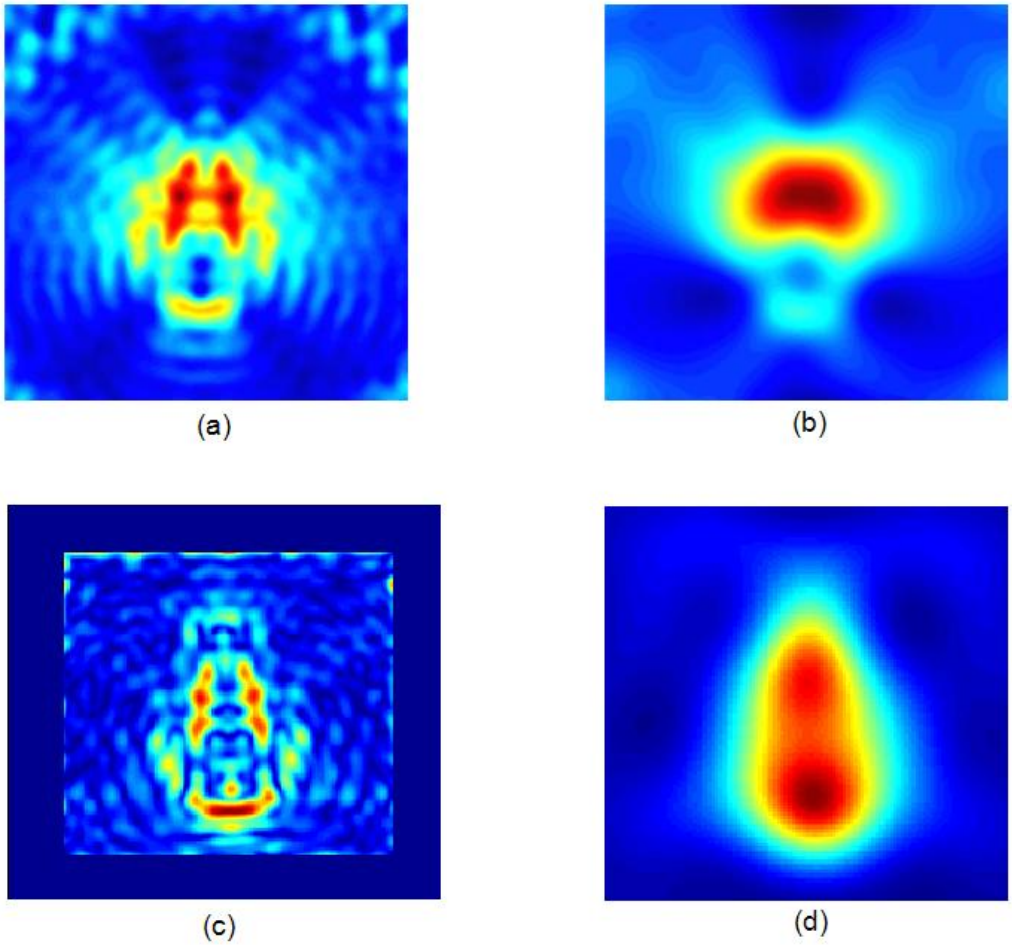

Figure. 5.7. IPS010 object: (a) Born reconstruction, (b) Cepstral with DFT reconstruction, (c) IPS010 with prior, (d) Cepstral with PDFT reconstruction

5.2 INSTITUT FRESNEL DATA

The Institute Fresnel data come from a series of laboratory-controlled experiments performed at the Institut Fresnel (Marseille, France), with the same idea of providing a means to help groups evaluate and improve their inverse scattering algorithms. The experimental setup consists of a fixed transmitting antenna and a moving receiving antenna which can move on a circular rail around the object corresponding to the Cartesian coordinate system as shown in Fig.5.8. The transmitting

antenna illuminates the objects from various locations equidistant around the object. The antennas are located at a distance of 1.67m from the center of experimental setup. More details about these experimental data can be found at [70].

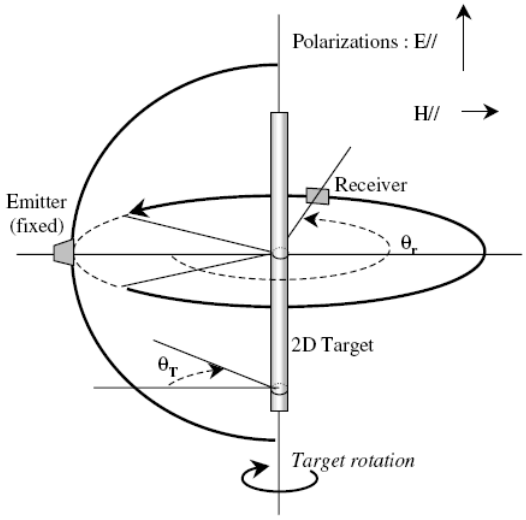

Figure. 5.8. Experimental setup from Institut Fresnel

Fig.5.8 shows the schematics of the cross sections of the actual object location with respect to the source and receiver. The scattered field was provided for a range of illumination frequencies and angles. For FoamDielInt and FoamDielExt (their notation for data sets) the emitting antenna was placed at 8 different locations which were 45˚ apart whereas for FoamTwinDiel and FoamMetExt, which are more complicated objects, the emitting antenna was positioned at 18 locations with 20˚ angular intervals. The receiving antenna collected complex data at 1˚ intervals. The scattering experiment was conducted using 9 operating frequencies which range from 2 GHz to 10 GHz. I first normalize the data and then compute the scattered field by subtracting the complex incident field from the complex total field. The inverse Fourier transform of the scattered field data gives a first Born reconstruction.

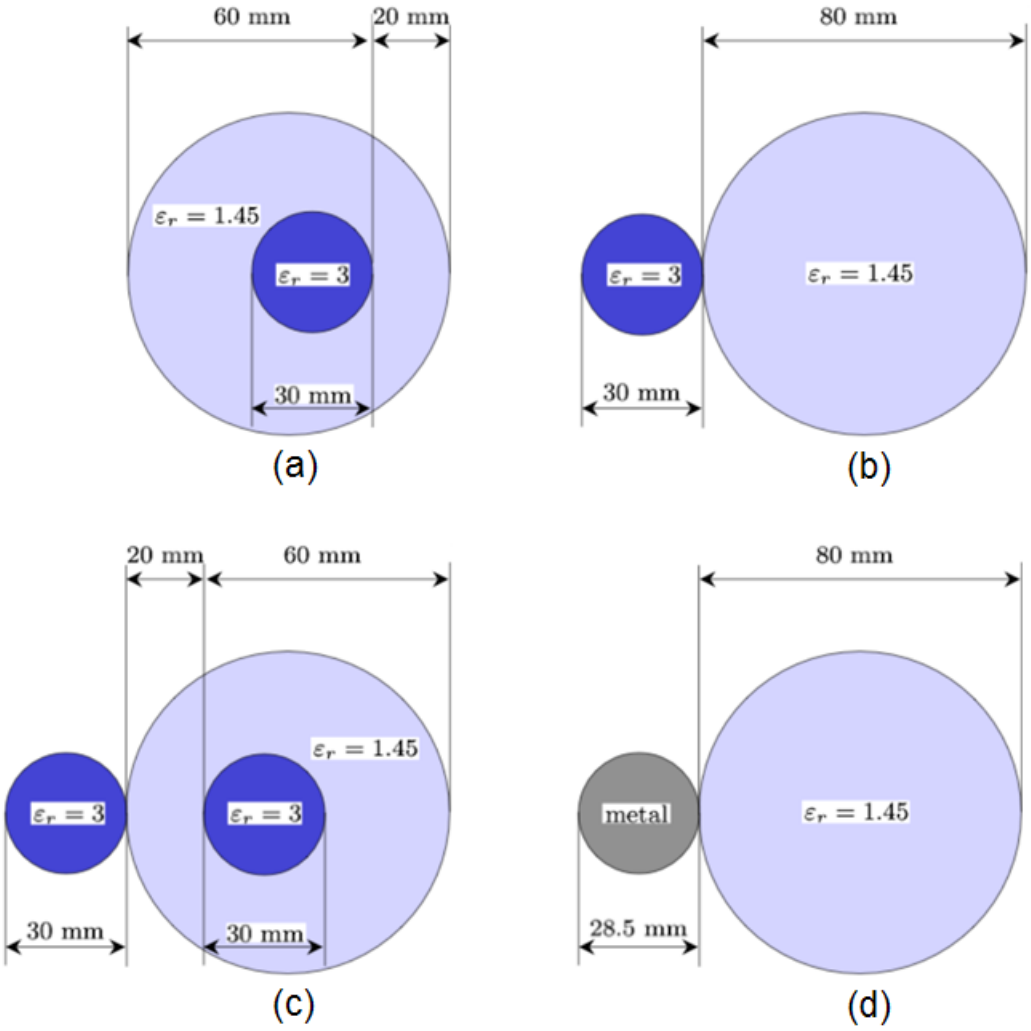

Figure. 5.9. Shape and relative permittivity of Institut Fresnel targets: (a) FoamDielInt, (b) FoamDielExt, (c) FoamTwinDiel, (d) FoamMetExt

5.3.1 FOAMDIELINT

The FoamDielInt consists of two cylinders: a "foam" of relative permittivity $\varepsilon_r \approx 1.45$ and inside the "foam" there is another circular dielectric of relative permittivity $\varepsilon_r \approx 3.0$. Fig.5.10 shows the reconstruction from the inverse Fourier transform of scattered field data i.e. first Born reconstruction of FoamDielInt. The Born reconstruction is computed at 6 GHz operating frequency for which the scattering strength of the object is $|kVa| \approx 22$. The object represents a fairly strong scatterer, $|kVa| >> 1$, as a result of which we see that the first Born reconstruction is not all that good, Fig.5.10.

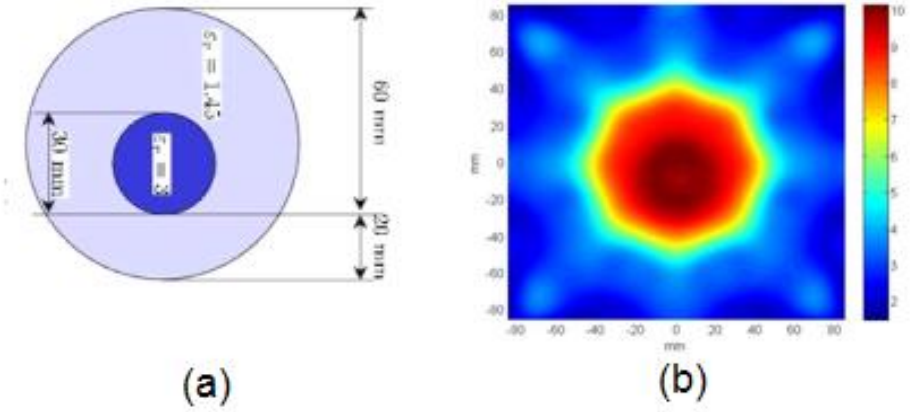

Figure. 5.10. FoamDielInt: (a) Actual object, (b) Born reconstruction

Fig.5.10(b) shows image of FoamDielInt using the Born reconstruction. The reconstruction shows several artifacts and it also fails to give any meaningful (i.e. quantitative) numbers for relative permittivity. I applied the homomorphic filtering method to FoamDielInt at 6Ghz. Fig.5.11 shows the implementation of the method to estimate the FoamDielInt object. I made the available data causal by moving it into one quadrant and added a reference point such that the phase of VΨ lies between $\pm\pi$.

A Gaussian filter is then applied to the cepstral domain and it is reduced in diameter until no discernable wavelike features associated with Ψ remain in the final image, which is obtained as a further inverse Fourier transform of the filtered cepstrum and exponentiation. Fig.5.11(e) shows the reconstruction obtained by applying cepstral filtering. The ratio of the contrast of the reconstructed cylinders matches the ratio of the permittivities in the original object. Fig.5.11(c) shows a log-plot of the cepstrum of VΨ after the reference point has been added. The log-plot is used to view the low energy features in the cepstral domain.

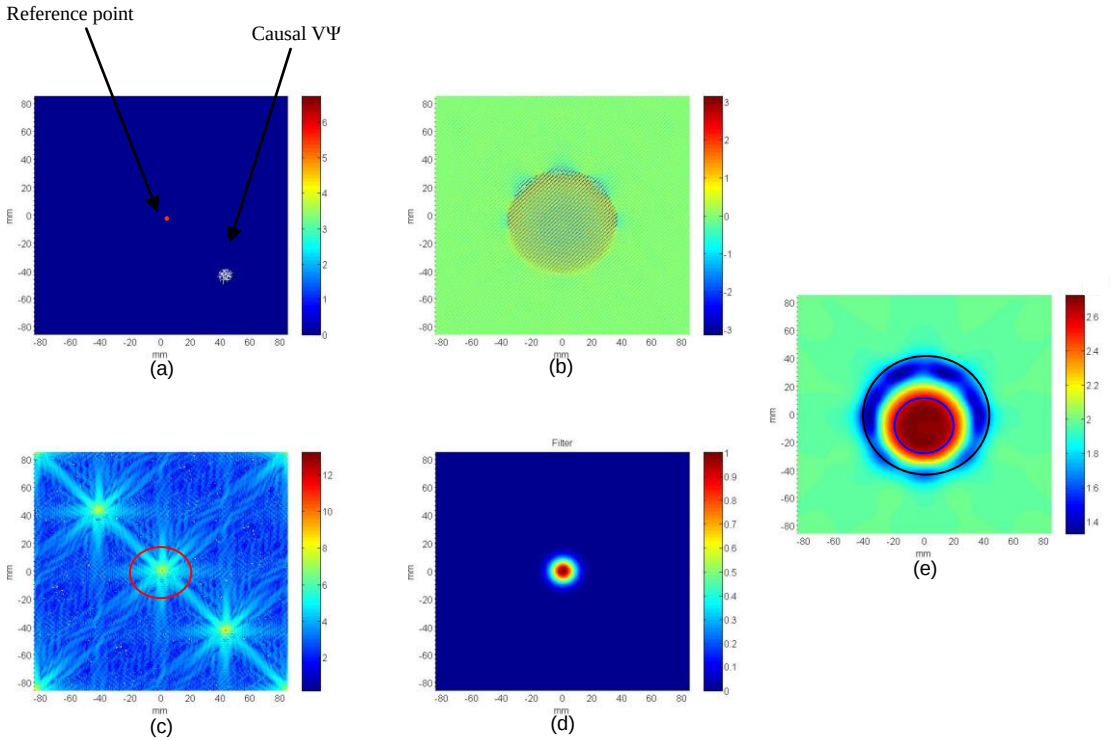

Figure. 5.11. Homomorphic filtering applied to FoamDielInt at 6 GHz: (a) Causal k-space data with reference point, (b) minimum phase VΨ, (c) log plot of cepstral domain, (d) Gaussian filter, (e) Cepstral reconstruction

The success of cepstral filtering relies on VΨ being minimum phase which is dependent upon the amplitude and location of the "artificial" reference point. Fig.5.12 shows how the quality of reconstruction varies as we change the reference point amplitude. Fig.5.12(c) shows that the quality of reconstruction improves as we get closer to satisfying the minimum phase condition. I also computed FoamDielInt for various other frequencies; the results are shown in Fig.5.13.

One of several factors that will affect the quality of the reconstruction (quite apart from the need to invert multiply scattered data) is the point spread function.

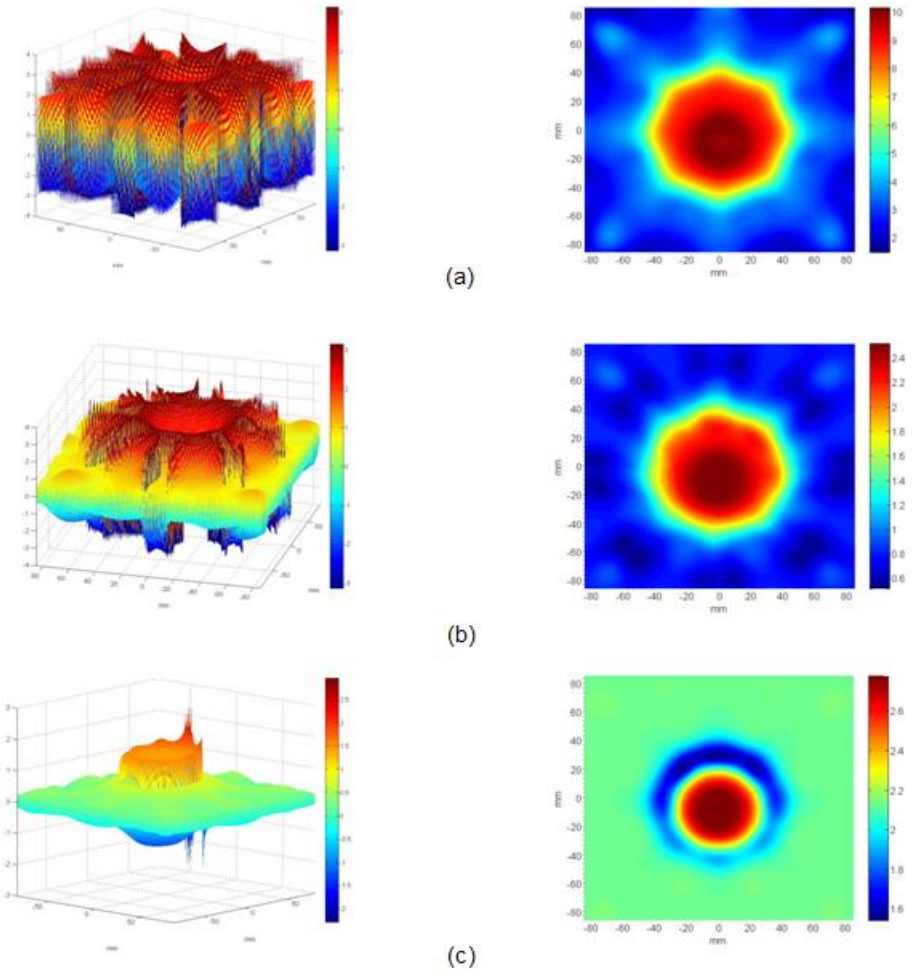

Figure. 5.12. Reference strength and cepstral reconstruction – left side image is the phase of VΨ and right side image is the cepstral reconstruction: (a) No reference added, (b) A small reference added, (c) Reference amplitude is strong enough such that phase < 2π.

Fig.5.14 shows the point spread function for different frequencies determined as the inverse Fourier transformation of the set of delta functions which mark the locations of the measured (i.e. Fresnel Institut provided) sampling points in k-space. These indicate the extent of features that one can hope to resolve in the final reconstructions of the scattering object V(r) from the measured scattered data in an ideal situation.

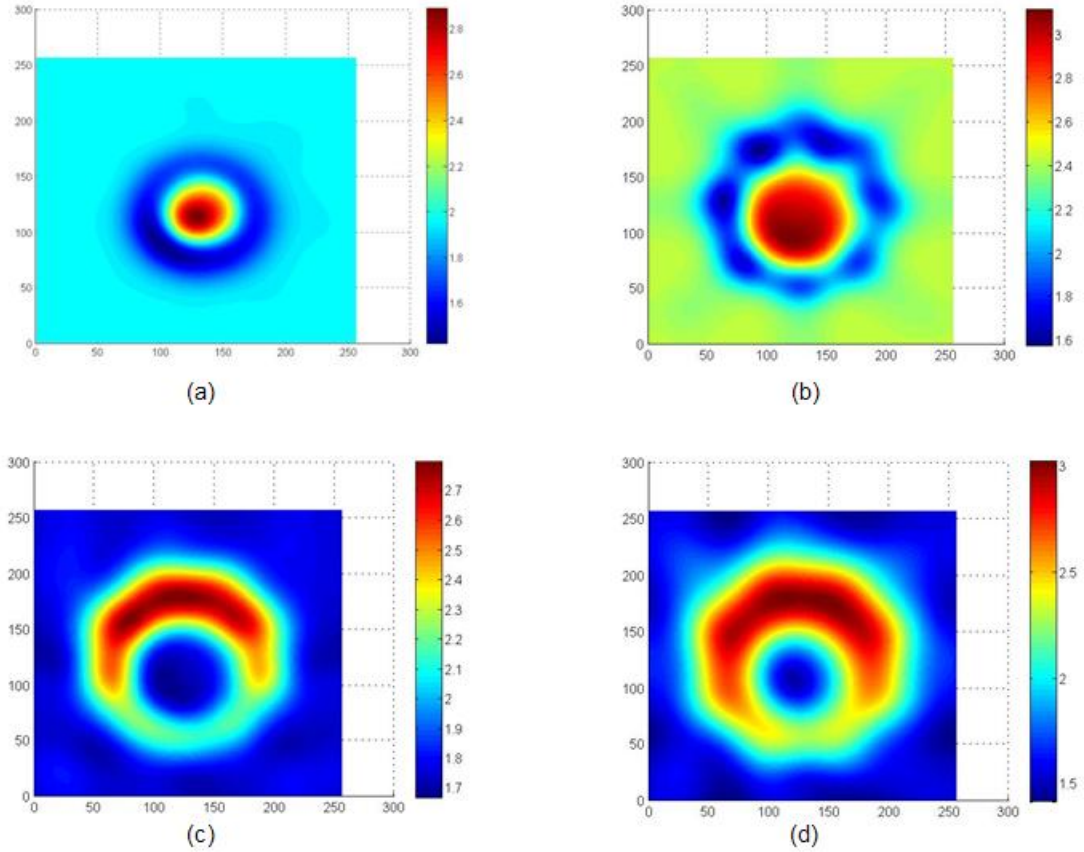

Figure. 5.13. Cepstral reconstruction of FoamDielInt at various frequencies: (a) 3 GHz, (b) 7 GHz, (c) 9 GHz, (d) 10 GHz

At lower frequencies, e.g. 3 GHz, the locus of data in k-space is over a much smaller radius Ewald circle than for the 10 GHz case. As a consequence, the main lobe of the point spread function is much larger at lower frequencies of illumination, and therefore, one can expect to see a lower resolution reconstruction. However, low frequency illumination also implies a better image estimate of V(r) based on the conditions for the validity of the first Born approximation, since a condition for the Born approximation to be valid is that $|kVa| << 1$. In addition, Fig.5.14(b) illustrates that for high frequencies the k-space coverage available from the measured data is insufficient to avoid strong side lobes, which can appear as replicas of the central lobe.

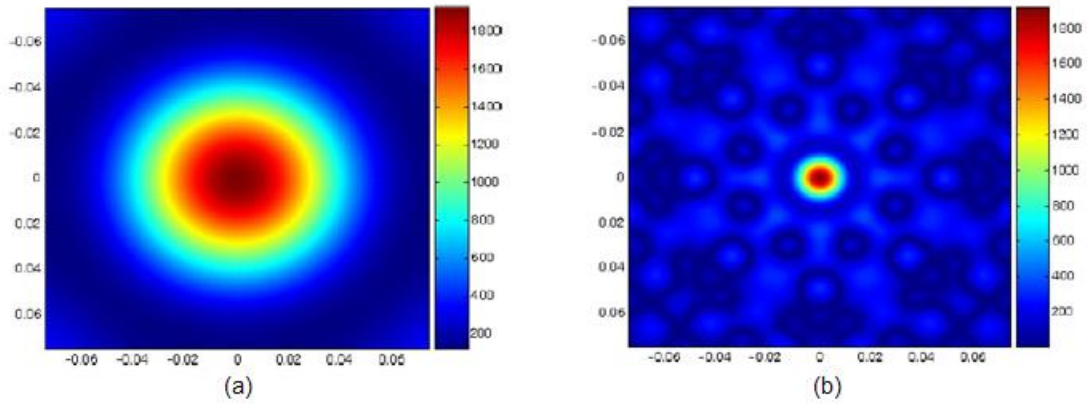

Figure. 5.14. Point spread functions corresponding to the locus of k-space scattered field coverage for the frequencies of (a) 3 GHz, (b) 10 GHz

This means, for a reconstruction based on the Born approximation one would expect an optimum performance at some lower frequencies but perhaps including more measured data at a larger number of incident and scattering angles. For data collected at 6 GHz, a good trade-off between high resolution and minimum artifacts can be observed.

It is important to note the poor reconstruction and an apparent contrast reversal at 9GHz and 10 GHz; see Fig.5.13(c) and Fig.5.12 (d). It is observed that the contrast of the recovered permittivity of the inner and outer cylinder is reversed i.e. the recovered permittivity of the inner cylinder should be around 3 but it is around 1.7 whereas the outer cylinder should have a permittivity of 1.45 but we recover it around 3. There are two possible explanations for this. The first is that inversion at lower frequencies meets conditions that increasingly favor the validity of the first Born approximation (i.e. $|kVa| << 1$) and for this scatterer at relatively lower frequencies, the sampling rate of the scattered field is adequate. One might also speculate that at higher frequencies, as the effective wavelength is reduced, there may be relatively more scattering from the boundary and less penetration of the field into the target, and so, less scattering from the higher permittivity internal features. Another important factor is that the angular

sampling of the scattered field and the number of incident field directions are identical for all frequencies employed. One can view this as an effective sampling of k-space that results in increasingly spread out high spatial frequency data locations as k increases, as indicated in Fig.5.15 below and one might justifiably expect that an increased sampling rate would be necessary in order to capture this information.

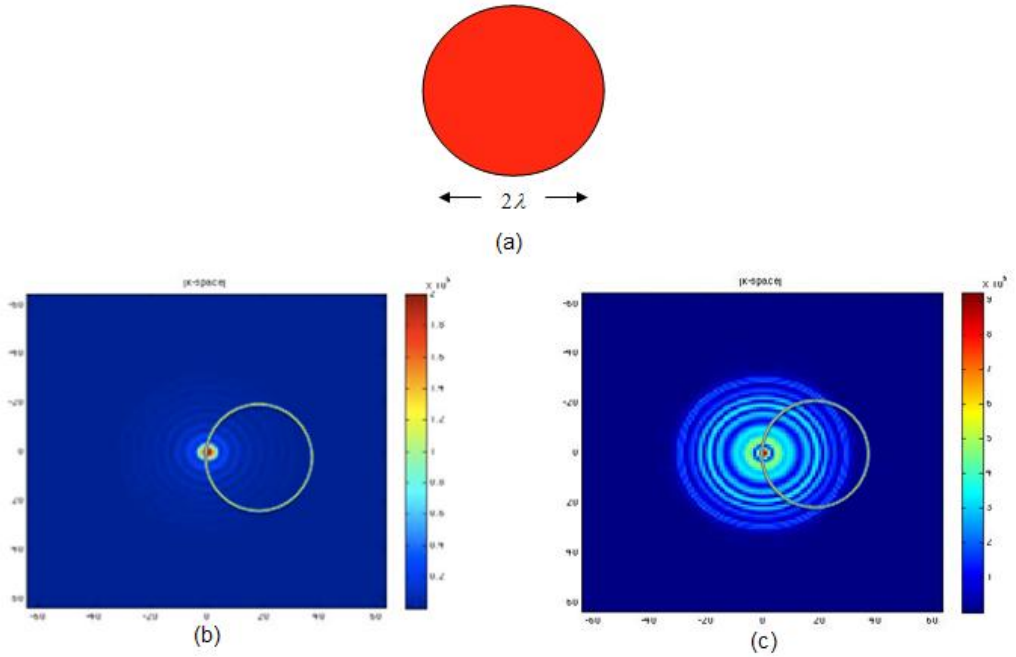

Figure. 5.15. k-space coverage for cylinder of radius 2λ (a) Target cylinder, (b) k-space coverage for weak scattering cylinder, (c) k-space coverage for strong scattering cylinder

Note that for the same geometrical sized cylindrical object in the images above, the k-space coverage varies dramatically as a function of the permittivity of the cylinder. For this reason, small radius Ewald circles will cover mostly low spatial frequencies while large radius Ewald circles will capture information about both low and many high spatial frequencies. The radius of the Ewald sphere in k-space changes with varying incident frequencies. Hence, the mapping between the scattered field data on these circles and the k-space representation of the two different $V\Psi$ shown here, results in

different regions of k-space being sampled. Small incident k values only map on to lower spatial frequencies. Each estimate obtained from a given incident frequency, can add information about different spatial frequencies and in principle should help in improving reconstruction quality.

I also observed the wrong background permittivity in Fig.5.11 (e). I postulated that the contrast reversal and incorrect surrounding permittivity level could be caused by the limited sampling of the scattered field for these objects, increasingly limited as k increases for a given source-receiver set of locations. The problem of limited data and undersampling is addressed by using the PDFT algorithm. Fig.5.16 shows the comparison of DFT and different prior functions incorporated into the PDFT reconstructions. It is evident from Fig.5.16 (b) that the contrast of the reconstruction is incorrect when using cepstral filtering with the DFT, since the background permittivity level has to be the lowest level for this object. Fig.5.16 (d) and Fig.5.16 (f) show that the PDFT has corrected this problem of an incorrect background permittivity. The effect of two different prior functions used with the PDFT are also shown, one a square and one a circle. The improvement using these is significant and the choice of prior is not that critical, as expected when it is large compared with V. Considering the fact that FoamDielInt is a strong scattering object, even first Born reconstructions have shown some improvement with the use of PDFT, as evident from Fig.5.16 (a) and Fig.5.16 (c).

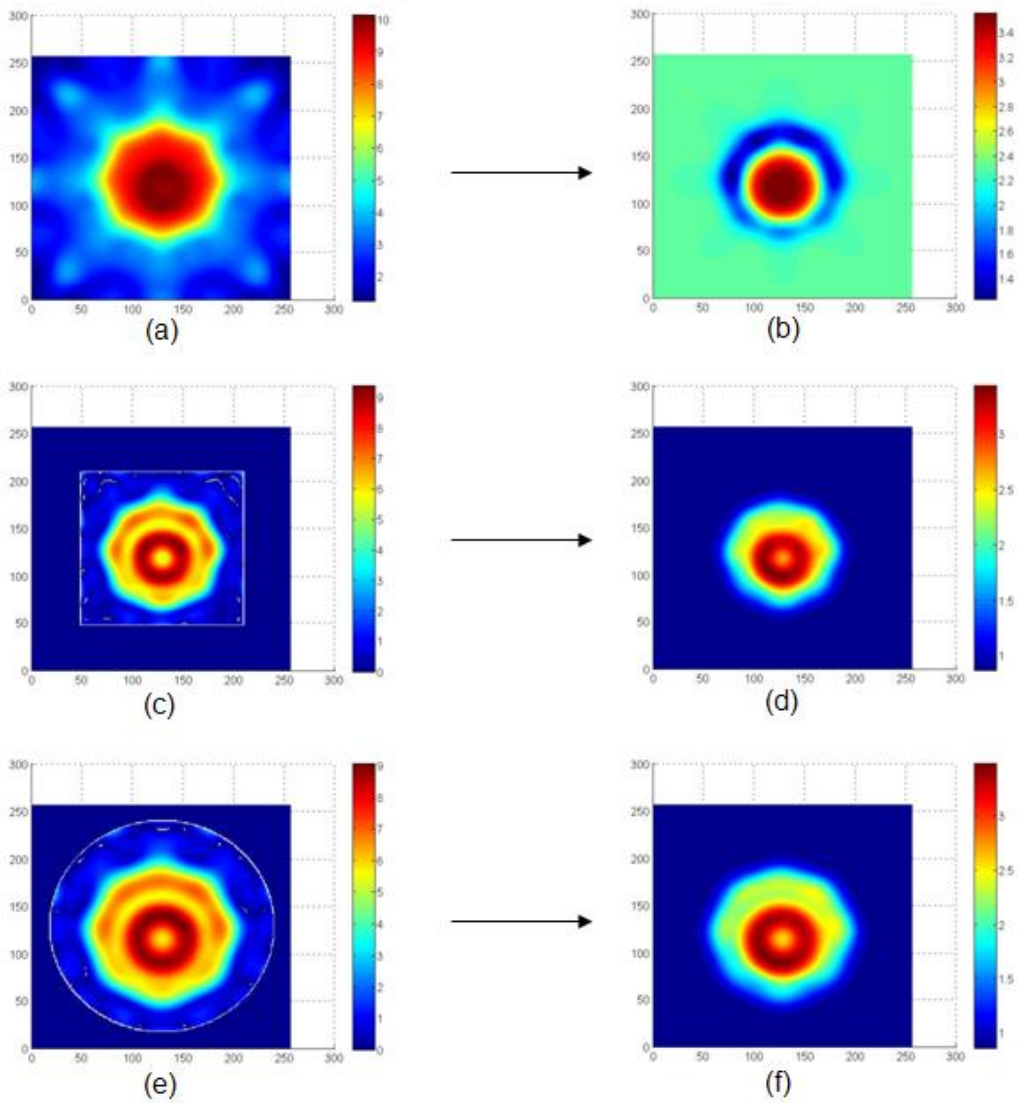

Figure. 5.16. FoamDielInt at 6 GHz (a) Born reconstruction with DFT, (b) Cepstral reconstruction using DFT, (c) Born reconstruction using PDFT–square prior, (d) Cepstral reconstruction using PDFT–square prior, (e) Born reconstruction using PDFT–circular prior, (f) Cepstral reconstruction using PDFT–square prior

Since each illumination frequency generates a different $V(\mathbf{r})\langle\Psi\rangle$ with V being the same and $\langle\Psi\rangle$ different for each wavelength, it follows that each illumination frequency provides us with different information and helpful redundancy. In other words changing the frequency of the incident field will provide an additional mechanism for extracting spatial frequencies of V alone from the cepstrum. A linear

combination of estimates for V acquired in this way, will further improve the SNR of the estimate for V while suppressing any residual components from the FT in each of these images. An example is shown below in Fig.5.17. I found, also as expected, that a Gaussian cepstral filter, being apodized, is preferable to a circular or square hard-cut filter.

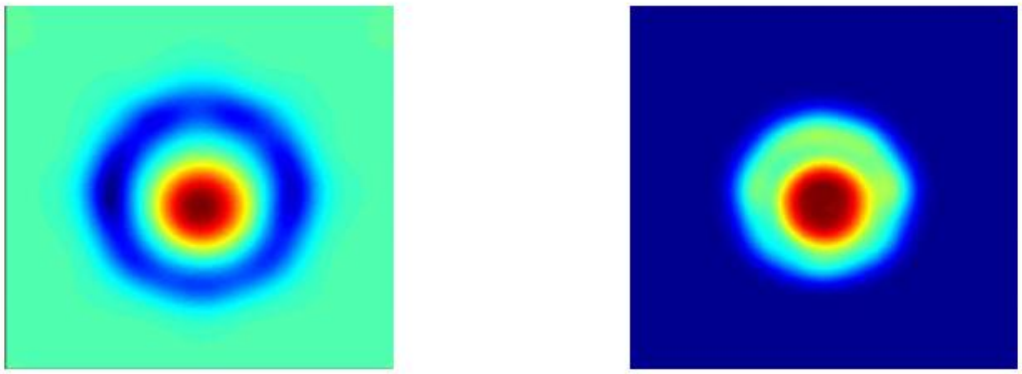

(a) (b)

Figure. 5.17. FoamDielInt at 6 GHz (a) Summation of cepstral reconstruction of 4Ghz, 5Ghz and 6Ghz with PDFT, (b) Summation of cepstral reconstruction of 4Ghz, 5Ghz and 6Ghz with DFT

The summation of cepstral reconstructions for different frequencies when used with the PDFT has shown significant improvement over the summation of cepstral reconstructions with DFT. To compare Fig.5.17 (a) and Fig.5.16 (f) one sees that the summation of cepstral reconstructions for different frequencies has shown improvement in shape estimation over a single frequency cepstral reconstruction using the PDFT, however summed up cepstral reconstructions still need improvement to recover the permittivity distribution of the object, V. One can employ a two step process in which one can use summation for shape retrieval and single frequency reconstruction for quantitative recovery.

5.3.2 FOAMDIELEXT

The FoamDielExt consists of a cylinder with of relative permittivity $\varepsilon_r \approx 1.45$ and an external cylinder with relative permittivity $\varepsilon_r \approx 3.0$. The Born reconstruction and cepstral reconstruction at illumination frequency of 6 GHz are shown in Fig.5.18.

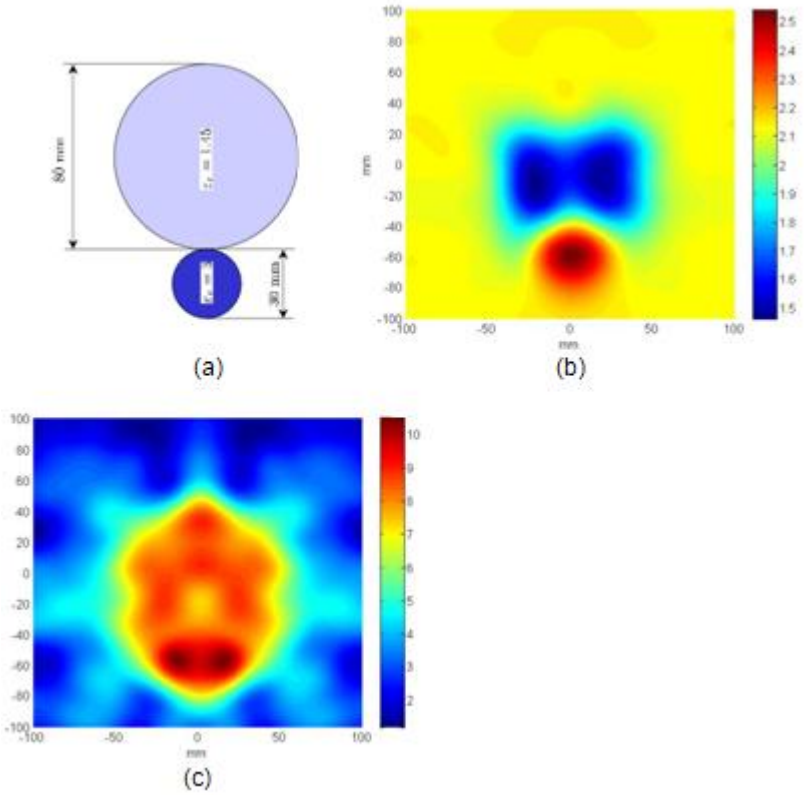

Figure. 5.18. FoamDielExt at 6GHz (a) Target, (b) Cepstral reconstruction with DFT, (b) Born reconstruction with DFT

Again I observed the background permittivity level being inconsistent from the actual object's background. The PDFT implementation of FoamDielExt with rectangular prior is shown in Fig.5.19

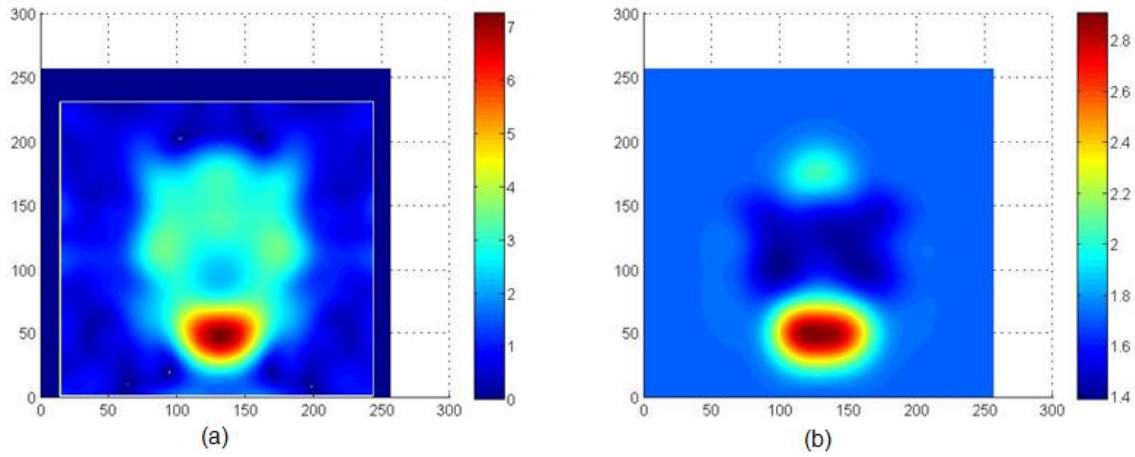

Figure. 5.19. FoamDielExt at 6 GHz (a) Born PDFT reconstruction with rectangular prior, (b) Cepstral PDFT reconstruction with rectangular prior

In Fig.5.19 (b) the background permittivity from PDFT estimate is improved significantly as compared to the DFT in Fig.5.18 (b) by use of a rectangular prior function. The extrapolated values contribute to the improvement of the resolution of the object estimate. If I chose to include more prior information in PDFT such as object feature information or relative permittivity differences, then I would see further improvement in the reconstruction.

5.3.3 FOAMTWINEXT

FoamTwinExt is one of the most complex objects made available by Institut Fresnel. It is the combination of FoamDielInt and FoamDielExt objects i.e. it contains a large cylinder with relative permittivity of $\varepsilon_r \approx 1.45$, a smaller inner cylinder with relative permittivity of $\varepsilon_r \approx 3.0$ and an outer small cylinder with relative permittivity of $\varepsilon_r \approx 3.0$. The Born reconstruction and cepstral reconstruction for FoamTwinExt are shown in Fig.5.20

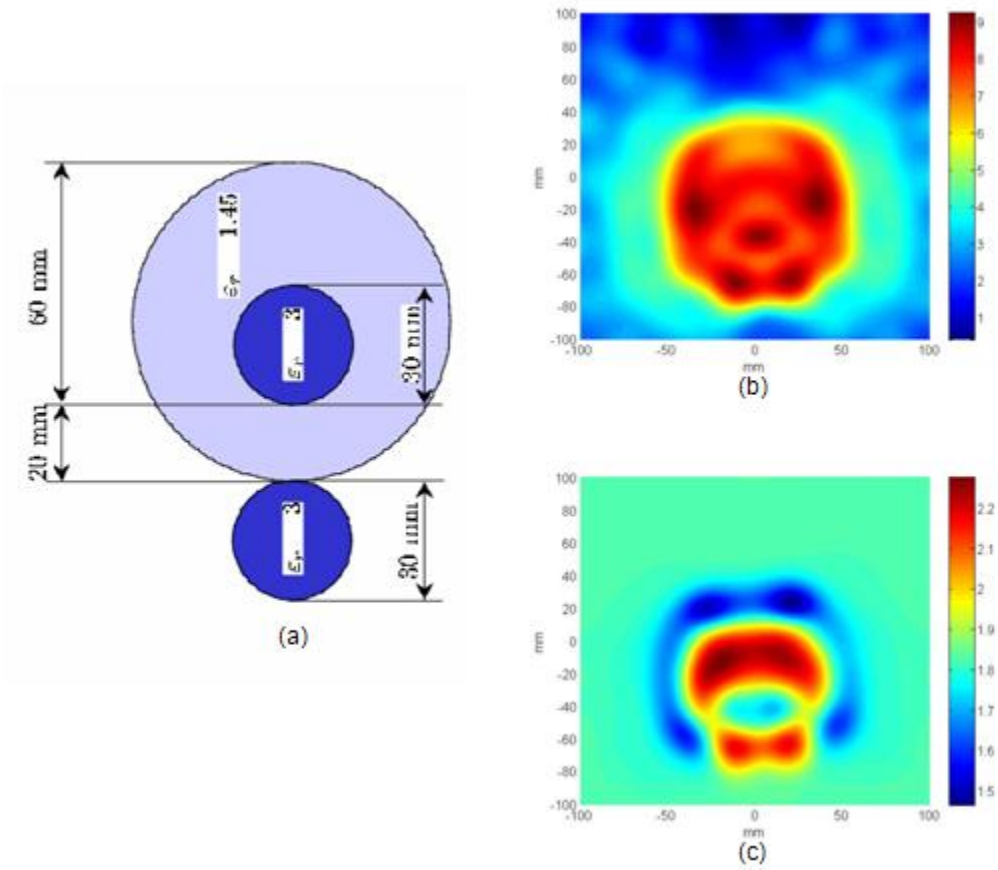

Figure. 5.20. FoamTwinExt at 6 GHz (a) Target, (b) Born reconstruction, (c) Cepstral reconstruction

The FoamTwinExt is a complex strong scatterer and a Born reconstruction is not able to retrieve either correct dimensions or the permittivity distribution of object, see Fig.5.20 (b). Considering the complexity of the object, the cepstral reconstruction has made a reasonable attempt in identifying all three cylinders or permittivity contrast levels as evident in Fig.5.20(c). I believe that the degradation in image quality is due to the lack of measured data, given the extent of multiple scattering that results from the high scattering strength of the original object. The amount of data provided for FoamTwinExt is not sufficient to recover a good image estimate. The scattering data for FoamDielInt, which has a simple circular geometry, was collected using 8 incident

illuminations, whereas the FoamTwinExt, which has a complex geometry, was collected using only 18 incident illuminations. This is strong evidence to suggest that as the geometrical and optical complexity of the scattering object increase one needs higher sampling density of the scattered field to obtain a meaningful reconstruction of the object. In section 5.4 I will discuss how scattered field data sampling requirements change with scattering strength.

5.3.4 FOAMMETEXT

FoamMetExt is a hybrid target which contains a large dielectric cylinder with relative permittivity of $\varepsilon_r \approx 1.45$ and an external metal cylinder. For metal objects the incident scattered field is scattered at the surface and then reflects back without entering into the object itself. However due to the scattered field components which cross a metal-dielectric interface, the multiple scattering effects become significant. Fig.5.21 shows the reconstruction of the hybrid object. It is evident from the figure that the shape of metal objects can be recovered with good quality even using linear approximations. The Born reconstruction has retrieved shapes for both the outer metal cylinder and the inner dielectric cylinder. Fig.5.21 (c) shows that the cepstral reconstruction has further cleaned the artifacts from the Born reconstruction.

5.3.5 COMPARISON OF RECONSTRUCTIONS

In this section I will show the comparison of reconstructions from various other methods, published in the journal *Inverse Problems* vol.**21**, issue 6, 2005 with our cepstral reconstructions.

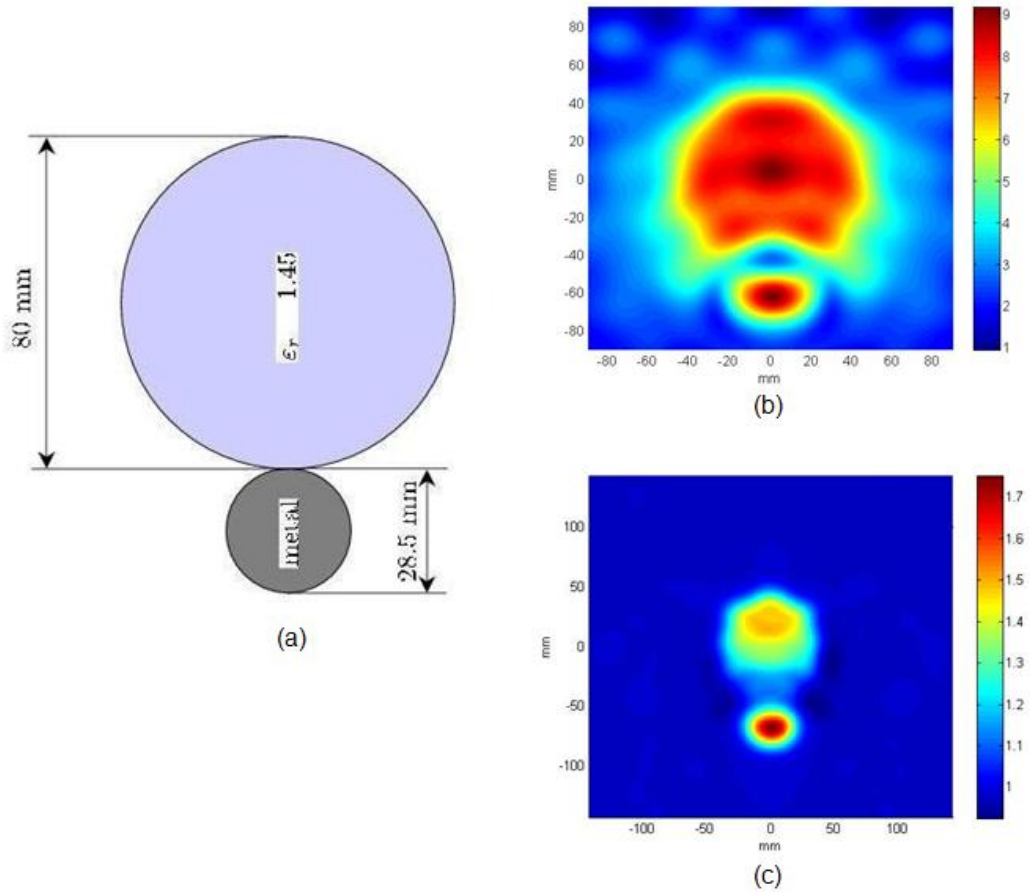

Figure. 5.21. FoamMetExt at 6 GHz (a) Target, (b) Born reconstruction, (c) Cepstral reconstruction

Fig.5.22 shows reconstruction attempts of FoamDielInt using various methods. Fig.5.22 (a) shows the reconstructed image of object using a two step inexact-Newton method [71] where Fig.5.22 (a) is reconstructed at 2 GHz and Fig.5.22 (b) is reconstructed at 5 GHz. Both the reconstructions show artifacts and the quality of reconstruction is poor. The recovered permittivity values are far off from the actual values. Fig.5.22(c) shows reconstruction from an iterative regularized contrast source inversion (CSI) method [24]. The reconstruction quality is average and it fails to give a good quantitative estimate of relative permittivity.

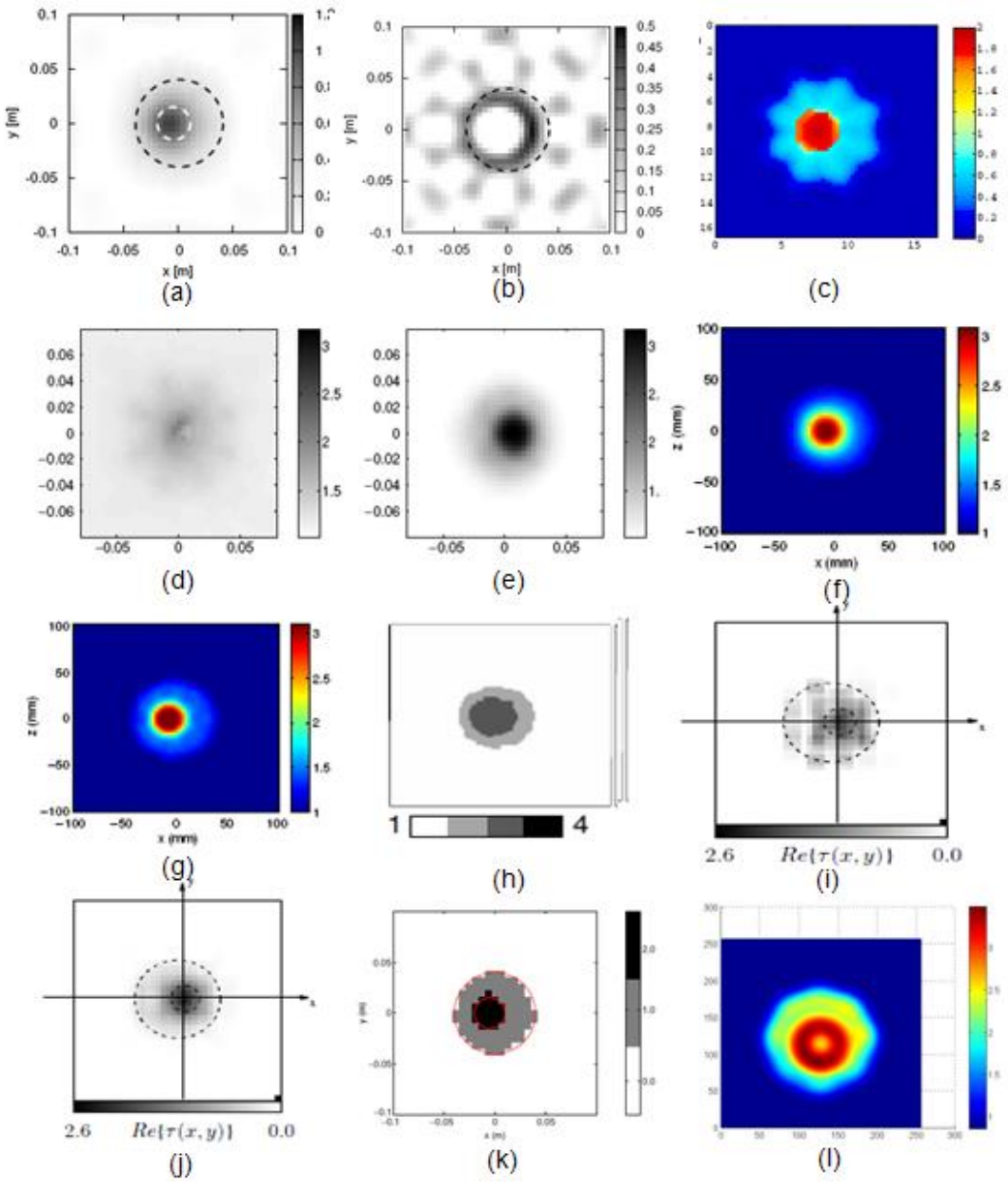

Figure. 5.22. Comparison of reconstruction algorithms on FoamDielInt (a) Figure taken from [71], (b) Figure taken from [71], (c) Figure taken from [24], (d) Figure taken from [72], (e) Figure taken from [72], (f) Figure taken from [27], (g) Figure taken from [27], (h) Figure taken from [73], (i) Figure taken from [74], (j) Figure taken from [74], (k) Figure taken from [75], (l) Cepstral reconstruction [46]

Fig.5.22 (d) and (e) show the reconstructions obtained using a modified gradient method (MGM) for the inversion of the scattered field data in conjunction with an adaptive multiscale approach based on spline pyramids to improve image quality [72].

Fig.5.22 (d) shows the reconstruction using MGM by itself. Again the quality of image reconstruction is poor as the boundaries of inner and outer cylinders are not distinguishable. Fig 5.22(e) shows reconstruction using MGM with an adaptive multiscale approach [72]. This method has done a decent job in recovering permittivities of cylinders. The reported permittivities for the outer cylinder and the inner cylinder are $\varepsilon_r \approx 2.5$ and $\varepsilon_r \approx 1.68$ respectively. The reconstruction obtained with this approach has shown good results but at the cost of 15% more computation time as compared to MGM. Fig.5.22 (f) and Fig.5.22 (g) show the reconstruction of FoamDielInt by a technique which combined diagonal tensor approximation (DTA) and CSI [27]. The reconstructions from this method are by far the best but again it uses an iterative approach which is computationally expensive and there is no guarantee of the convergence of the algorithm to a solution, right or wrong. Fig.5.22 (h) shows reconstruction from another iterative method based on a Bayesian inversion method. The quality of the reconstruction is poor in a sense that it not only fails to retrieve the correct dimensions of the cylinders but also gives a poor estimate of relative permittivity. The reconstructions shown in Fig.5.22 (i) and Fig.5.22 (j) are obtained by using an iterative multi-scaling approach (IMSA) which exploits the scattered field data through a multi-step reconstruction procedure [74]. Fig.5.22 (i) shows the reconstruction when the incident wave is modeled as a plane wave and Fig.5.22 (j) shows the reconstruction when the incident wave is modeled as a line source. Fig.5.22 (k) shows an image estimate using another iterative approach [75]. This approach has done a good job in recovering the shape of the object but it fails to recover any

quantitative information about the object. Fig.5.22 (l) shows a reconstruction from my proposed method, cepstral filtering.

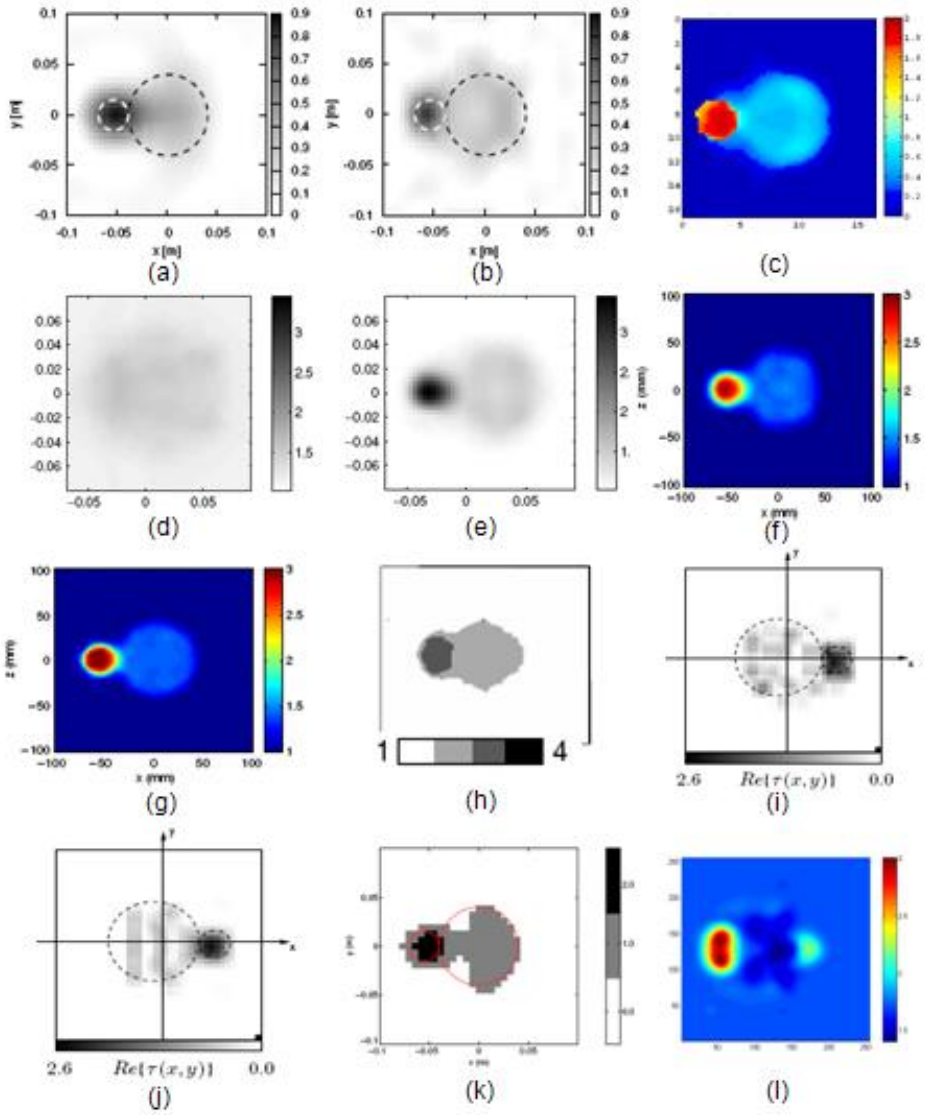

Figure. 5.23. Comparison of reconstruction algorithms on FoamDielExt (a) Figure taken from [71], (b) Figure taken from [71], (c) Figure taken from [24], (d) Figure taken from [72], (e) Figure taken from [72], (f) Figure taken from [27], (g) Figure taken from [27], (h) Figure taken from [73], (i) Figure taken from [74], (j) Figure taken from [74], (k) Figure taken from [75], (l) Cepstral reconstruction [46]

Considering the fact that it is a non-iterative low computational cost algorithm, the reconstruction not only gives a good estimate of the object's geometry but also gives a

meaningful recovery of relative permittivities. The reconstruction comparison for FoamDielExt, FoamTwinDiel and FoamMetExt are shown in Fig.5.23, Fig.5.24 and Fig.5.25 respectively.

Fig.5.23 shows the reconstructions of FoamDielExt from various methods. Again most of the methods fail to do a reasonable job in reconstructing FoamDielExt except reconstructions shown in Fig.5.23(f) and Fig.5.23(g), which is done using a combination of DTI and CSI [27]. Fig.5.23 (h) which is reconstructed using a Bayesian inversion method [73], gives a good estimate of shape but it lacks quantitative accuracy. Fig.5.23 (i) and Fig.5.23 (j), which are based on IMSA [74], both show artifacts in reconstruction. The reconstruction shown in Fig.5.23 (e) is based on MGM along with a multi-scale approach [72]. The quality of reconstruction is good in a sense that it has not only recovered shape but also relative permittivity. The only downside is that it is an iterative process and it takes 15% more iterations as compared to MGM. The reconstruction from the cepstral method, Fig.5.23 (l), has done a reasonable job in recovering permittivity and shape of object but we still see image artifacts associated with limited data availability.

Fig.5.24 shows the comparison of the reconstructions between various published methods for FoamTwinDiel. Because of its complex geometrical configuration this object is one of the most challenging objects provided by Institut Fresnel. Other than [27], most of the reconstructions have shown a low quality estimate of the object. Being non-iterative in nature, the cepstral method depends on data coverage. For this multi-layered object, in order to get a meaningful reconstruction from cepstral method I will

argue here that more data is needed. Even with less data the cepstral method is still able to isolate contrast difference between all three cylinders.

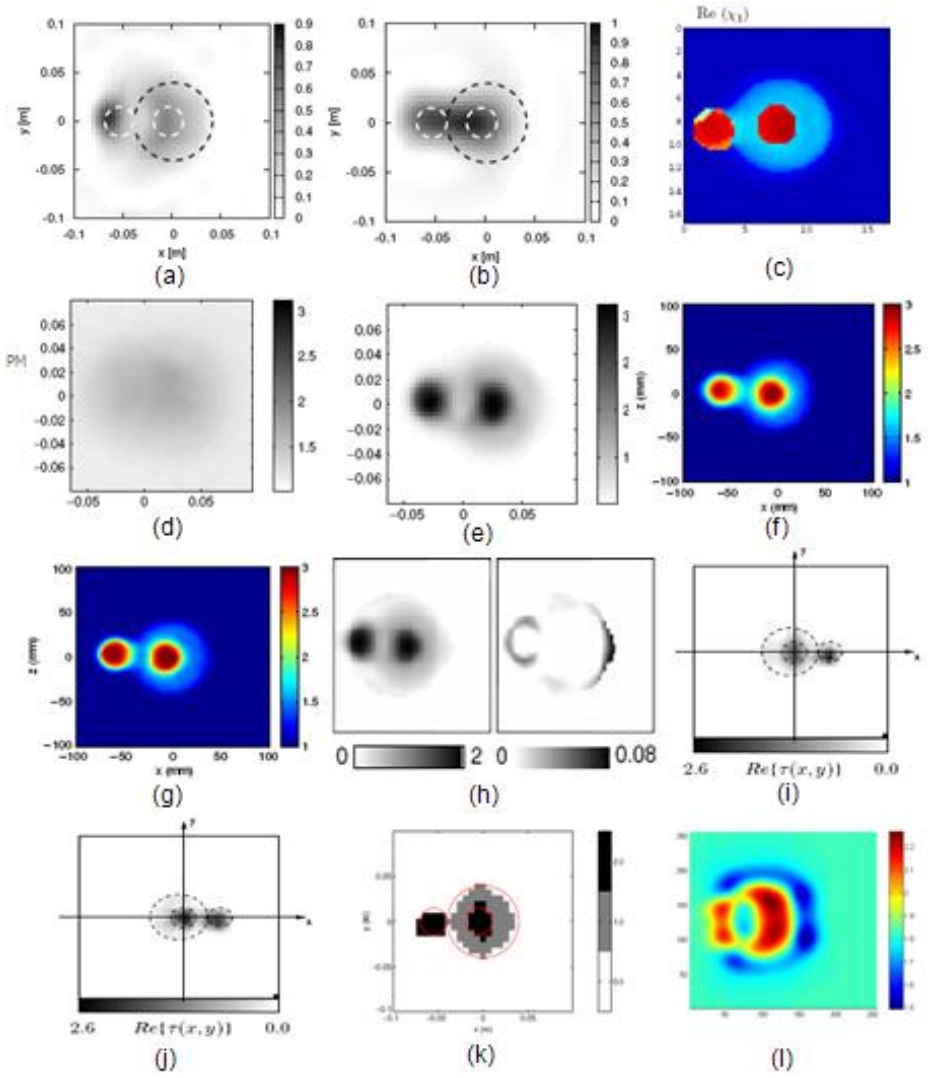

Figure. 5.24. Comparison of reconstruction algorithms on FoamTwinDiel (a) Figure taken from [71], (b) Figure taken from [71], (c) Figure taken from [24], (d) Figure taken from [72], (e) Figure taken from [72], (f) Figure taken from [27], (g) Figure taken from [27], (h) Real and imaginary parts, Figure taken from [73], (i) Figure taken from [74], (j) Figure taken from [74], (k) Figure taken from [75], (l) Cepstral reconstruction [46]

Fig.5.25 shows the comparison of different reconstruction methods on FoamMetExt. The two step Newton method [71], which attempted to reconstruct the first three objects, was not able to show any reconstruction for the metal object. Also the iterative

method proposed in [75] did not present any reconstruction for the metal object. Fig.5.25 (a) based on CSI [24] shows good reconstruction of the shape but does not provide any quantitative description. Fig.5.25 (d) shows both shape and a quantitative image. Fig.5.25 (e) and Fig.5.25 (f) show the real and imaginary part of the reconstructions using the Bayesian inversion method [73]. Fig.5.25 (g) and Fig.5.25 (h) show real and imaginary part of metal object using IMSA [74]. Both the reconstructions from [73] and [74] lack quantitative recovery. Also they fail to recover all object features in a single image.

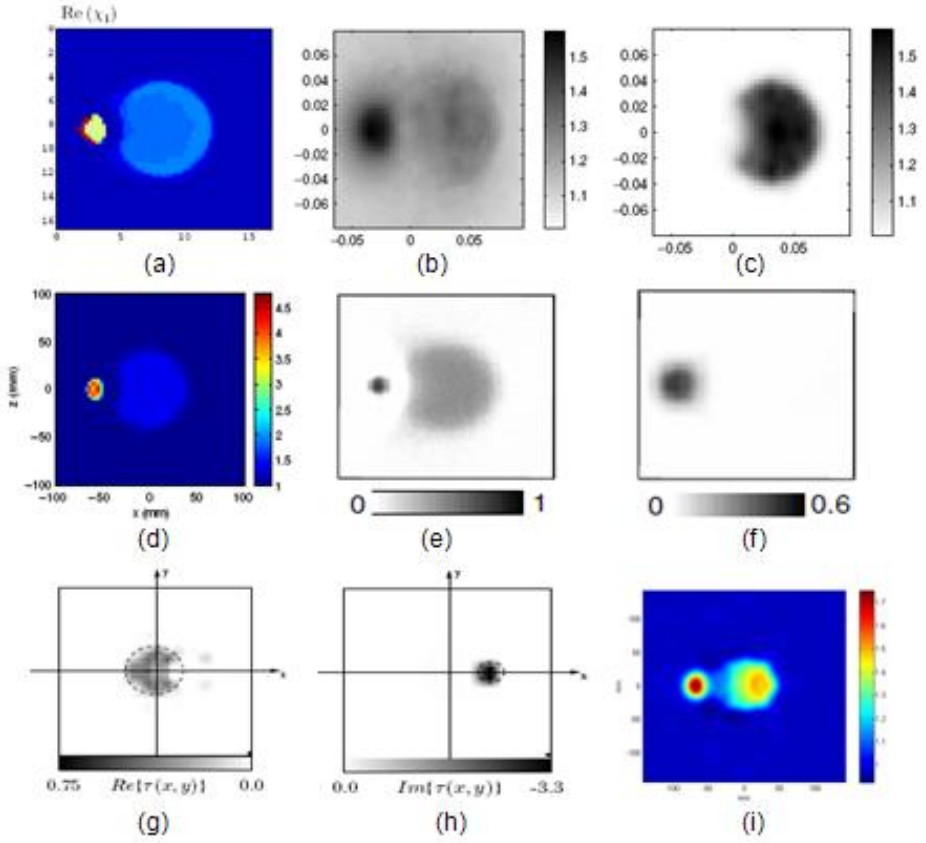

Figure. 5.25. Comparison of reconstruction algorithms on FoamMetExt (a) Figure taken from [24], (b) Figure taken from [72], (c) Figure taken from [72], (d) Figure taken from [27], (e) Figure taken from [73], (f) Figure taken from [73], (g) Figure taken from [74], (h) Figure taken from [74], (i) Cepstral reconstruction [46]

The image from the cepstral method shows good shape and permittivity estimation. It still suffers from wrong background permittivity, which is due to limited data availability.

5.4 SAMPLING NEEDS FOR INVERSE SCATTERING PROBLEM

In this section I will discuss the impact of sampling on the quality of the reconstruction also as a function of scattering "strength", i.e. extent of multiple scattering. As the complexity and average permittivity of the scattering object increases, the effects of limited data (i.e. number of incident angles used and number of scattered field measurements as a function of scattering angle) become more significant. With only a finite number of measurements available, even noise-free data are insufficient to provide a unique solution. In the presence of noise, ill-conditioning becomes a serious issue, as described earlier when introducing the PDFT. The quality of the reconstruction is obviously strongly dependent on how a scattered field is sampled. In 1-D (and also of course in higher dimensions) one tends to rely on Shannon's sampling theorem. Let *f(t)* represent the object with finite support and its Fourier transform is given by

$$F(\omega) = \int_{-W}^{W} f(t) e^{-i2\pi\omega t} dt \tag{5.9}$$

where F(ω) is an analytic function. Assuming

$$F(n\alpha)\,,\ n = 1, 2, ..., N$$

$$0 < \alpha \le d = \frac{\pi}{W}$$

the Shannon sampling theorem tells that for $|t| \le W$

$$f(t) = d \sum_{m=-\infty}^{\infty} F(md) e^{imdt} \tag{5.10}$$

$$F(\omega) = d \sum_{m=-\infty}^{\infty} F(md) \frac{\sin\ W(\omega - md)}{\pi\ \ \omega - md}\ . \qquad (5.11)$$

In two or higher dimensions, it is well known that for any given object support, there could be many sampling grids available and one typically adopts an optimum sampling grid in order to achieve the best reconstruction from a minimum density of samples; of course in principle, Shannon demands an infinite number of samples with the specified bandwidth dependent sampling density, or denser.

The sampling needs for the inverse scattering problem depend upon the geometrical complexity and scattering strength of the object. With a high permittivity, the effective wavelength inside the scattering medium is smaller and so smaller features will more likely contribute to propagating waves as compared to evanescent waves within the scattering volume. Recognition of this effective increase in the inherent bandwidth within the scattering volume needs to be accounted for in the sampling strategy outside the scattering volume. An analysis to this effect was developed by Miller [84] recently. He analyzed propagation and scattering from a very fundamental modal perspective as radiation transferred from a "source" volume to a "receiver" volume. His intent was to try to put fundamental limits on various optical systems such as a slow light system or optical information channel. His conclusion was that the total number of degrees of freedom, N, of a scattering system, based on a model, would be proportional to the total experimental volume, B_v and the maximum refractive index (= square root of permittivity in our case), specifically $N = (B_{v)}(n_{max)} / \lambda^3$. Clearly as the maximum permittivity and extent of multiple scattering increases, the number of degrees of freedom pertinent to the system also increases and so, additional sampling points to properly represent the fields in this experimental volume will be needed.

This is consistent with observations made by others. The strong scatterers have significant contributions from multiple scattering components in far-field as compared to weak scatterers. It has been shown by Chen and Chew [77] that by considering multiple scattering in the reconstruction algorithm super resolution is possible. The evanescent waves, generated within an inhomogeneous medium, contain subwavelength information about the object. The multiple scattering converts these evanescent waves into the propagating waves as a result of linear interaction between evanescent waves and the scatterer [77]. Therefore these strong multiple scattering components carry additional information about the structure of the scatterer in the far field [76]-[78]. An object with higher permittivity will have more information encoded in the far field pattern of the scattered wave than the same object with lower permittivity. In order to benefit from this additional information it is important to ensure an adequate sampling rate i.e. a lower scattering strength object will have different sampling requirements than a higher scattering strength object.

To investigate the impact of scattering strength on reconstruction quality, consider two cylinders with the same geometry but different relative permittivities as shown Fig.5.26. The wavelength employed in the experiment is 1mm and the diameter of both cylinders is 2mm. The scattered field data in the far field is generated using an analytical solution for homogeneous cylinders.

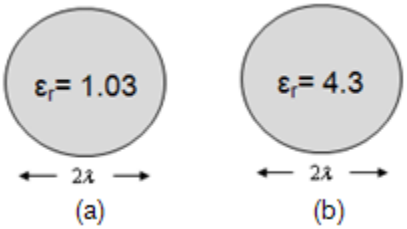

Figure. 5.26. Target description (a) Weak scatterer (b) Strong scatterer

Fig.5.27 shows the Born reconstructions for the target cylinders. Fig.5.27 (a) is the reconstruction for weak cylinder with relative permittivity of ε_r=1.03 and scattering strength k|V|a ≈ 0.2. Fig.5.27 (b) is the reconstruction for strong cylinder with relative permittivity of ε_r =4.3 and scattering strength of k|V|a ≈ 21. The object in each case is illuminated with incident plane wave ranging from 0º to 315º and it is sampled at increments of 45º i.e. total number of samples are 8. The simulated scattered field data are mapped onto an Ewald sphere in k-space and then inverse Fourier transformed to compute Born images. The Born estimate for the weak scatterer has a cleaner reconstruction as compared to the Born reconstruction for the strong scatterer as evident from Fig.5.27.

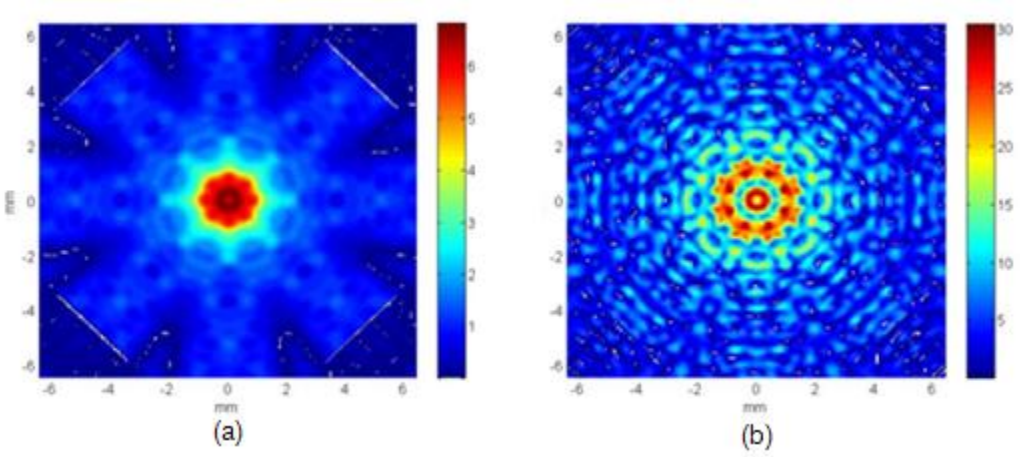

Figure. 5.27. Born reconstruction for target cylinders (a) Reconstruction for weak scatterer (b) Reconstruction for strong scatterer

The scattered field for strong scatterers encodes more information about the scattering object and in order to utilize this extra information we need a higher sampling rate than the weak scatterer. In order to investigate further, the object is illuminated with an incident plane wave sampled at 1º increments i.e. the total number of samples are 360.

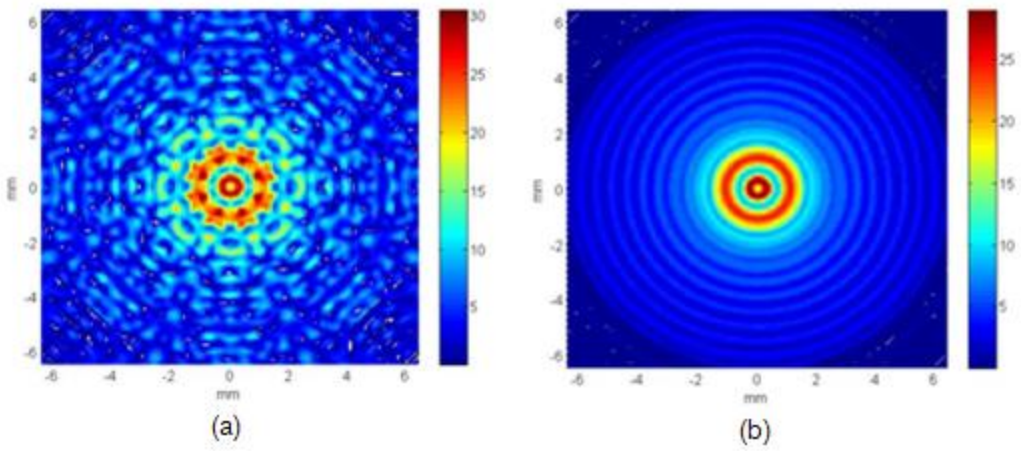

Figure. 5.28. Born reconstructions for strongly scattering cylinder (a) 8 illumination angles (b) 360 illumination angles

Fig.5.28 shows side by side images of the Born reconstructions from the strong scattering object with Fig.5.28 (a) showing reconstruction using 8 illumination angles and Fig.5.28 (b) showing image estimate using 360 illumination angles.

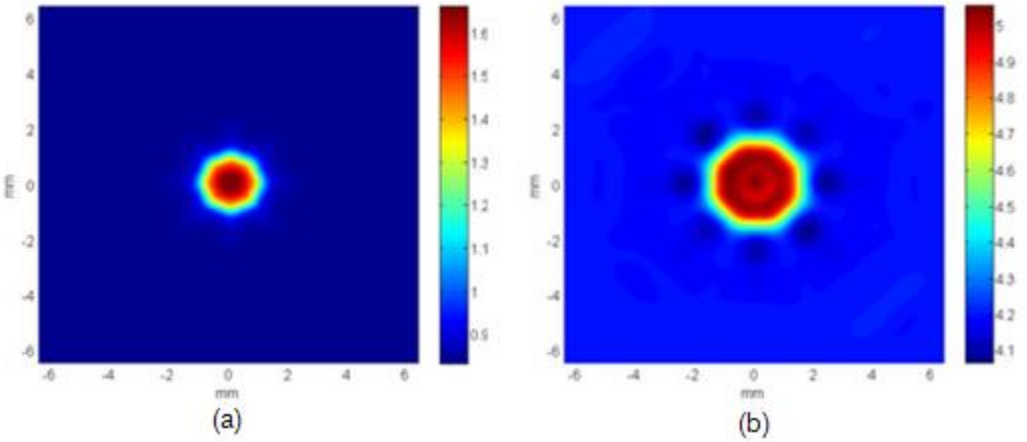

Figure. 5.29. Cepstral reconstruction for target cylinders (a) Reconstruction for weak scatterer (b) Reconstruction for strong scatterer

Increasing the sampling rate has significantly improved the quality of reconstruction for the strong scatterer. Clearly with more views one is able to extract additional information encoded in multiple scattering components of far field data. The cepstral

inversion method was also applied to recover a weak scatterer and a strong scatterer for 8 illumination angles and 360 illumination angles. Fig.5.29 shows the reconstructions for the strong cylinder and the weak cylinder using the cepstral inversion method. The scattering experiment was conducted using 8 illumination angles with 45º increments. Fig.5.29 (a) shows the reconstruction for the weak scattering target and Fig.5.29 (b) shows the reconstruction for the strong scatterer. Comparing both images closely it is again evident that for the given illumination angles, the reconstruction quality of the weak cylinder is better than the reconstruction quality of the strong cylinder. For a weak scattering object, dimensions are closer to the actual target and the background is smoother, whereas for a strong scatterer I see multiple scattering artifacts in the background along with incorrect dimensions. It is important to note that the cepstral method has still done a remarkable job in reconstructing the strong scatterer. The comparison between Born reconstruction and cepstral reconstruction for strong scattering targets with 8 illumination angles is shown in Fig.5.30. Despite higher permittivity the cepstral reconstruction is still cleaner because it takes into account multiple scattering components. I also investigated cepstral inversion for 360 illumination angles with 1º increments. The results are shown in Fig.5.31. Increasing the number of incident illumination angles from 8 to 360 has less impact on the reconstruction of the weak cylinder as compared to the reconstruction of the strong cylinder.

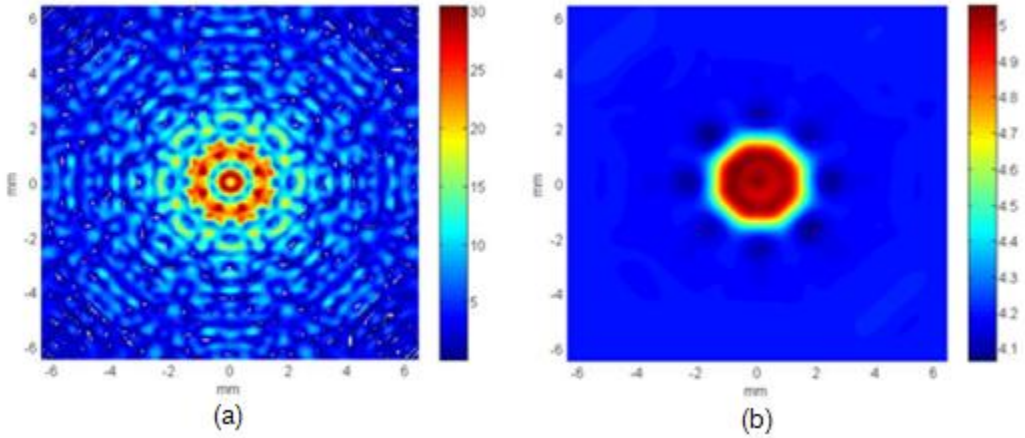

Figure. 5.30. Reconstruction for strong cylinder with 8 illuminations (a) Born reconstruction (b) Cepstral reconstruction

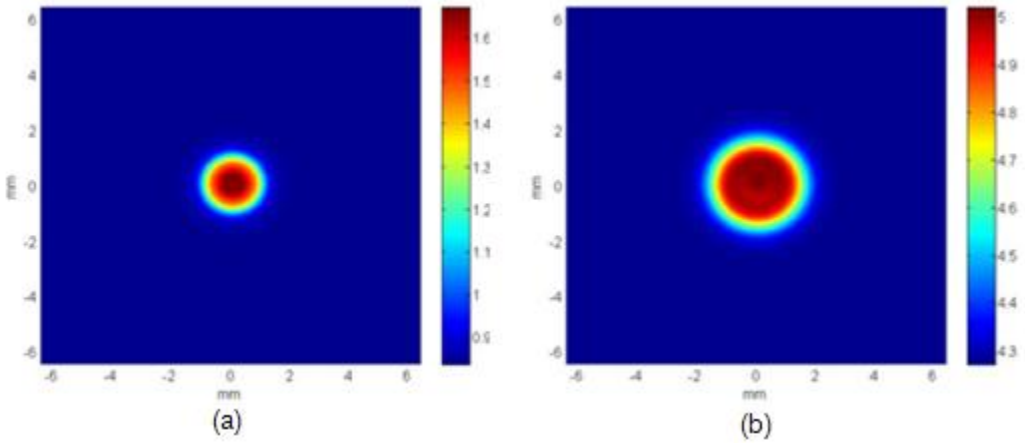

Figure. 5.31. Cepstral reconstruction with 360 illuminations (a) Weak cylinder (b) Strong cylinder

This is in accordance with my earlier discussion that the scattered field for weak scattering objects has less contribution from multiple scattering components and hence can perform reasonably well with a lower sampling rate as opposed to strong scatterers whose field is dominated by strong contributions from multiple scattering components. In order to study the relationship between the quality of reconstruction and scattering strength I performed a series of experiments on simulated data. I considered three cylinders with the same dimensions but different permittivities. I then systematically

increased the number of illumination angles and studied their effects on the quality of reconstruction for all three objects. Simulations suggest that there exists a linear relationship between sample points and refractive index as shown in Fig.5.32.

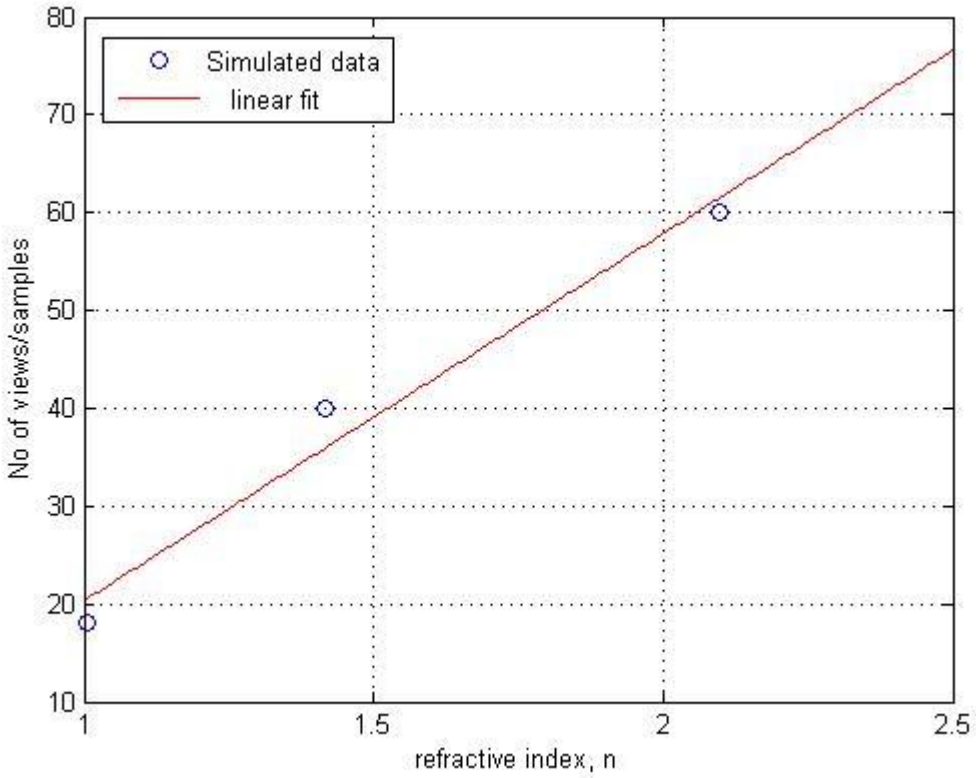

Figure. 5.32. Refractive index vs. No of views

These results and the paper by Miller [84] provide a criterion for a new sampling theorem for the inverse scattering problem which properly takes into account scattering strength, structural details of the object and illumination wavelength. In Miller's paper, he explores so-called fundamental limits to optical systems by considering the number of degrees of freedom an arbitrary system can possess. His approach is completely general and counts the number of modes that can exist in a volume connecting a source

domain to a receiver domain through an arbitrary "transport" or multiply scattering domain. An upper bound on the number of degrees of freedom turn out to be proportional to the volume of the system divided by the cube of the wavelength multiplied by a measure of the maximum refractive index in the system. As we have seen in simulations, when the permittivity of a target increases, there is obviously increased multiple scattering. To get a reconstruction of the same quality that one might find acceptable for a truly weak object (i.e. first Born scatterer) from a specific number of data points, then one needs to increase the amount of data collected in proportion to the increased index of the stronger scattering target.

CHAPTER 6: CONCLUSIONS

In this dissertation I proposed a nonlinear signal processing based method to solve the inverse scattering problem for strongly scattering targets. In other words, I developed a method to determine a quantitative image of the permittivity distribution inside a penetrable scattering object. Limited noisy data render this inverse problem highly ill-posed and the need to compute an estimate for the secondary source or contrast source, prior to applying the (nonlinear) homomorphic filter, was explained. The PDFT algorithm was introduced for this purpose.

Current methods to solve inverse scattering problems are either iterative in nature or they use linearization techniques. The iterative methods are computationally very expensive and their convergence is not always guaranteed. The linearization techniques use first Born or Rytov approximations which are applicable to only a very restricted class of scatterers, usually requiring that the strength of the scattering distribution be weak or slowly varying in the scale of incident wavelength. If the characteristic size of scattering inhomogeneities is vanishingly small then a single scattering (i.e. first Born approximation) is appropriate, and thus, making the inverse step a relatively straightforward Fourier-based algorithm.

The approach described here was based on homomorphic filtering to recover the unknown object, V(r) from a limited set of scattered field data, Ψ. From this, one can obtain an estimate of $V\langle\Psi\rangle$ by mapping the scattered field data onto Ewald surfaces in k-space and inverse Fourier transforming. Fourier inversion of the far field scattered

data is assumed but near field data can also be used. If <Ψ> were similar in nature to the incident field, which is the case when the first Born approximation is valid, then it would not corrupt the resulting image of V. This is the standard approach in conventional diffraction tomography. The homomorphic filtering step linearizes the product of $V\langle\Psi\rangle$ by taking its natural logarithm and Fourier transforming into the so-called cepstral domain. A filter was applied in the cepstral domain to remove the cepstral frequencies associated with the unwanted "noise-like" term $\langle\Psi\rangle$. Successful filtering requires some preprocessing of the estimate of $V\langle\Psi\rangle$ in order to ensure that its logarithm was well behaved and amenable to spatial filtering in the associated Fourier, i.e. cepstral domain. Only the logarithm of a minimum phase function is well-defined. The preprocessing step ensured that the data being filtered fulfills this minimum phase condition. With processed minimum phase V<Ψ> data, the nonlinear filtering operation can be executed in a reliable and stable fashion. The minimum phase condition was enforced by adding an appropriate reference wave, R, to $V\langle\Psi\rangle$ or a delta function in the k-space domain thereby satisfying Rouche's theorem. Satisfying the theorem, requires that the k-space data be moved into one quadrant to make it causal and the reference point, R was located at the origin of causal k-space data. Its amplitude was systematically increased until the minimum phase condition was met. The ideal value for R occurred when the phase of the modified $V\langle\Psi\rangle$ was continuous and unwrapped with values lying strictly within the range of $-\pi$ and $+\pi$. The homomorphic filtering step was achieved by multiplying the cepstrum with a filter whose width was systematically reduced until the wavelike structures associated with $\langle\Psi\rangle$ were eliminated.

I applied this method to real laboratory-controlled experimental data collected at the Air Force Research Laboratory's (AFRL) Ipswich Facility in MA [54]-[57] and the Institut Fresnel (Marseille, France) [70]. The data consisted of real and imaginary parts of scattered field measurements from a number of inhomogeneous strong scattering targets with different geometries. I was able to estimate not only the shape of objects but also their relative permittivity. Since cepstral filtering will inevitably remove some frequencies associated with the target function, V, I also showed how combining estimates for V obtained using different frequencies, improved the SNR and overall quantitative accuracy of the resulting estimate for V, while further suppressing any residual features arising from the averaged internal total field distributions.

For various scattering objects I also compared the reconstructions using the proposed method and the reconstructions from various other methods and found that my proposed method showed better results in terms of qualitative and quantitative reconstruction of objects as compared to other methods. However I observed some inconsistencies in the reconstructions as a function of frequency and investigated the consequences of having undersampled data in a nonlinear algorithm. A contrast reversal and an erroneous background level in the reconstructions prompted this study. Since only a limited number of incident view angles were provided and scattered field data for each of these were only measured at discrete angles, the k-space coverage is necessarily sparse. To address this problem I employed a linear spectral estimation method known as the PDFT which provides a solution that is both data consistent and of minimum weighted norm through the use of a suitably designed Hilbert space. The PDFT, by incorporating prior information, helped improve the initial estimate of $V\langle\Psi\rangle$ prior to

homomorphic processing. It reduced the background permittivity problem and enhanced image quality. For each target the optimal prior was found by monitoring the energy of the PDFT estimate as the prior function was modified. The prior function can be as simple as an estimate of the support of the target, or it can contain information about the target itself that lies within its boundaries.

The artifacts were still observed in the reconstructions of some objects which were geometrically more complex and with a larger range of permittivities. This led me to revisit the impact of the number of data points available for the inverse algorithm, since it is recognized that sampling theorems are written for linear problems based on bandwidth. A numerical experiment was conducted to study the impact of scattering strength (i.e. increasing values of V) on the quality of the reconstruction but as a function of the number of scattered field data available to process. The scattered field data was numerically generated for two similarly sized objects but with different scattering strengths. I showed that the object with higher permittivity requires a higher density of scattered field data than the object with lower permittivity in order to give the same quality of reconstruction. In other words, the results demonstrated that for strongly scattering objects, in order to extract additional information encoded in multiple scattering components, one needs a higher sampling rate. An intuitive and important point that supports this is that the effective wavelength inside the object for a strong scatterer is smaller than the effective wavelength inside the object for a weak scatterer. Effective wavelength will be roughly proportional to free space wavelength divided by n where n is the refractive index or the square root of the permittivity. Some prior knowledge about the range of V is very important when planning data collection for an

inverse scattering problem; i.e. the permittivity should be taken into account for choosing k-space coverage. From this, I discussed the formulation of a new sampling theorem for inverse scattering problems which considers scattering strength, shape of the object and wavelength used in the experiment, to dictate sampling rate.

In addition, as part of this research, I developed an interactive graphical user interface (GUI) known as the "cepstral inversion tool" which implements the cepstral inversion algorithm. This tool provides a user-friendly interface to load k-space scattered field data and implement causality, minimum phase condition and homomorphic filtering to reconstruct an object under test. It is the first tool of its kind for this problem domain that visually demonstrates the quality of reconstruction as you vary parameters. The software can be used as a modeling tool to further investigate different invariants of the inverse scattering problem.

In summary one of the main contributions of this research was to develop a new and robust inverse scattering algorithm. The significance of this method is that it is non-iterative, it retrieves both quantitative and qualitative descriptions of objects and it is applicable to objects for which the Born or Rytov approximation fails. The second contribution was to demonstrate that the method could be successfully applied to real scattered field data. The third and most significant contribution of this research was to investigate sampling needs for inverse scattering problems in general. The final contribution was to develop user-friendly software to reconstruct an unknown object using the cepstral inversion method.

To take this research forward, a next step is to further investigate the relationship between scattering strength, object geometry and reconstruction quality.

From this we would expect to formalize a completely new sampling theorem for inverse scattering problems, as an alternative to the Shannon sampling theorem. The new theorem should be able to suggest the k-space data density based on the scatterer's geometry, permittivity properties, and the wavelength employed. The opportunity also exists to refine the filtering step with more sophisticated and automated filters, say an annular bandpass filter. Future work is needed to adapt this algorithm for 3-D objects and to demonstrate its applicability to 3-D strong scatterers in the full electromagnetic (i.e. vector) case. More work can be done to make the cepstral inversion software more robust and the next generation of software can include different reconstruction algorithms so that users can switch from one algorithm to another algorithm and do a comparative study, although it is expected that the cepstral method will always be superior in speed and superior to other methods for a large classes of targets.

REFERENCES

1. Avinash C.Kak and Malcom Slaney, *Principles of computerized tomographic imaging*, IEEE press, New York, 1988.

2. W.C.Chew, *Waves and fields in inhomogeneous media*, IEEE Press, Piscataway, 1995.

3. R.Zoughi, *Microwave nondestructive testing and evaluation*, Kluwer academic publishers, Netherlands, 2000.

4. A.J.Devaney, "Nonuniquemess in the inverse scattering problem," *J.Math.Phys*, July 1978.

5. Xio An Chen and Wen Xun Zhang, "On the well-posedness of solution in the inverse scattering problem," *IEEE Antennas and Propagation Symposium*, vol.1, June 1989.

6. Angela Maria Darling, *Digital object reconstruction from limited data incorporating prior information*, Thesis, University of London, 1984.

7. F.C.Lin and M.A.Fiddy, "Image estimation from scattered field data," *Int. J. Imag. Sys. Technol*., vol.2, pp.76-95, 1990.

8. P.M.Morse and H.Feshbach, *Methods of theoretical physics*, New York: McGraw-Hill, 1953.

9. John B.Morris, Michael A.Fiddy and Drew A.Pommet, "Nonlinear filtering applied to single-view backpropagated images of strong scatterers," *J. Opt. Soc. Am. A*., Vol.13, No.7, pp.1506-1513, July 1996.

10. D. Colton and R. Kress, *Integral equations in scattering theory*, Wiley, New York, 1983.

11. A. J. Devaney, "A computer simulation of diffraction tomography," *IEEE Trans. Biomed. Eng.* vol. BME-30. pp. 377-386. 1983.

12. W. Rieger, M. Haas, C. Huber, G. Lehner and W. M. Rucker, "Image Reconstruction from Real Scattering Data using an Iterative Scheme with Incorporated a priori Information," *IEEE Antennas and Propagation Magazine*, vol. 41, No. 2, April 1999.

13. Haruyuki Harada, David J. N. Wall, Takashi Takenaka, and Mitsuru Tanaka, " Conjugate Gradient Method Applied to Inverse Scattering Problem," *IEEE Transactions on Antennas and Propagation*, vol. 43, No. 8, August 1995.

14. Y. M. Wang and W. C. Chew, "An iterative solution of the two-dimensional electromagnetic inverse scattering problem," *International journal of imaging systems and technology*, vol. 1, 100-108, 1989.

15. Y. M. Wang and W. C. Chew, "Reconstruction of two-dimensional permittivity distribution using the distorted Born iterative method," *IEEE Trans. Medical Imaging*, vol. 9, pp. 218-225, June 1990.

16. P. A. Martin and A. G. Ramm, "Inverse scattering for geophysical problem. III. On the velocity-inversion problems of acoustics," *Proc. R. Soc. Lond*. A, 399, 153-166, 1985.

17. A. G. Ramm, "Recovery of potential from fixed energy scattering data," *Inverse problems*, vol. 4, 877-886, 1998.

18. A. G. Ramm, "Stability of numerical method for solving the 3D inverse scattering problem with fixed-energy data," *Inverse problems*, vol. 6, L7-L12, 1990.

19. Y. M. Wang and W. C. Chew, "Accelerating the inverse scattering algorithms by using fast recursive aggregate *T*-matrix algorithm," *Radio Sci.*, vol. 27, 109-116, 1992.

20. C. Estatico, G. Bozza, A. Massa, M. Pastorino and A. Randazzo, "A two-step iterative inexact-Newton method for electromagnetic imaging of dielectric structures from real data," *Inverse problems*, 21, S81-S94, 2005.

21. Estatico C, Pastorino M and Randazzo A, "An inexact-Newton method for short-range microwave imaging within the second order Born approximation," *IEEE Trans. Geosci. Remote Sens*., 2005.

22. Kohn R V and McKenney A, "Numerical implementation of a variational method for electrical impedance tomography," *Inverse Problems*, 6, 389–414, 1990.

23. P. M. van den Berg P M, van Broekhoven A L and Abubakar A, "Extended contrast source inversion," *Inverse Problems*, 15, 1325–44, 1999.

24. Aria Abubakar, Peter M van den Berg and Tarek M Habashy, "Application of the multiplicative regularized contrast source inversion method on TM- and TE-polarized experimental Fresnel data," *Inverse problems*, vol. 21, S5-S13, 2005.

25. Song L P and Liu Q H, "Fast three-dimensional electromagnetic nonlinear inversion in layered media with a novel scattering approximation," *Inverse Problems*, vol. 20, 171–94, 2004.

26. Song L P and Liu Q H, "A new approximation to three-dimensional electromagnetic scattering," *IEEE Geosci. Remote Sens*. Lett. 2 238–42, 2005.

27. Chun Yu, Song L P and Liu Q H, "Inversion of multi-frequency experimental data for imaging complex objects by a DTA-CSI method," *Inverse Problems*, vol. 21, 165–178, 2005.

28. Belkebir K and Tijhuis A G, "Modified^2 gradient method and modified Born method for solving a two dimensional inverse scattering problem," *Inverse Problems*, vol. 17, 1671–88, 2001.

29. A Dubois, K Belkebir and M Saillard, "Retrieval of inhomogeneous targets from experimental frequency diversity data," *Inverse Problems*, vol. 21, 65–79, 2005.

30. Tommaso Isernia, Lorenza Crocco and Michele D'Urso, "New Tools and Series for Forward and Inverse Scattering Problems in Lossy Media," *IEEE geoscience and remote sensing* letter, Vol. 1, No. 4, Oct 2004.

31. Tommaso Isernia, Lorenza Crocco and Michele D'Urso, "Testing the contrast source extended Born inversion method against real data: the TM case," *Inverse problem*s 21, 2005.

32. E. Wolf, "Three-dimensional structure determination of semi-transparent objects from holographic data," *Optics Comm.*, 1, 1969.

33. A. G. Ramm, "Is the Born approximation good for solving the inverse scattering problem when the potential is small?," *J. Math. Anal. Appl.*, vol. 147, 480-485, 1990.

34. C. L. Byrne, R. L. Fitzgerald, M. A. Fiddy, T. J. Hall, and A. M. Darling, "Image restoration and resolution enhancement," *J. Opt. Soc. Am*. 73, pp. 1481—1487, 1983.

35. A. Ishimaru, *Wave propagation and scattering in random media*, Academic press, New York, vol. 1, 1978.

36. Malcom Slaney, Avinash C. Kak and Lawrence E. Larsen, "Limitations of Imaging with First-Order Diffraction Tomography," *IEEE transactions on microwave theory and techniques*, vol. MIT-32, No. 8, 1984.

37. M. Kaveh and M. Soumekh, "Algorithms and error analysis for diffraction tomography using the Born and Rytov approximations," *Inverse methods in electromagnetic imaging*, part 2, 1983.

38. R. H. T. Bates, W. M. Boerner and G. R. Dunlop, "An extended Rytov approximation and its significance in remote sensing and inverse scattering," *Opt. Comm.*, vol. 18, 421-423, 1978.

39. J. Richmond, "Scattering by a dielectric cylinder of arbitrary cross-sectional shape," *IEEE Trans. Antennas Propagat.* , vol. AP-13, pp334-341, 1965.

40. R. F. Harrington, *Field Computation by Moment Methods*, FL: Krieger, Malabar 1983.

41. P. Lobel, R. E. Kleinman, Ch. Pichot, L. BlancFeraud, and M. Barlaud, "Conjugate-Gradient Method for solving inverse scattering with experimental data," *IEEE Antennas and Propagation*, Vol. 38, No. 3, pp 48-51, 1996.

42. T. Takenaka, H. Harada, and M. Tanaka, "On a simple diffraction tomography technique based on modified Newton-Kantorovich method," *Microwave Opt. Tech. Lett.*, vol. 5, pp. 94-97, 1992.

43. M. Testorf, A. Morales-Porras and M. Fiddy, "Imaging of strongly scattering targets based on signal processing algorithms," *IEICE Trans. Electron*., vol. E83-C, No. 12, 2000.

44. Donald G. Childers. David P. Skinner and Robert C. Kemerait, "The cepstrum: A Guide to processing," *IEEE proc*., vol. 65, No. 10, 1977.

45. D. Raghuramireddy and R. Unbehauen, "The Two-Dimensional Differential Cepstrum," *IEEE transactions on acoustics, speech and signal processing*, vol. ASSP-33, No. 4, 1985.

46. U Shahid, M Testorf, and M A Fiddy, "Minimum-phase-based inverse scattering algorithm," *Inverse Problems*, vol. 21, pp 1 – 13, 2005.

47. Dan E. Dudgeon and Russel M. Mersereau, *Multidimensional digital signal processing*, Prentice-Hall, New Jersey, 1984.

48. Fiddy M A and Shahid U, "Minimum phase and zero distributions in 2D," *Proc. SPIE*, vol. 5202, pp 201–208, 2003.

49. R. E. Burge, M. A. Fiddy, A. H. Greenaway and G. Ross, "The phase problem," *Proc. Roy. Soc. Lond*., A350, pp 191-212, 1976.

50. M. A. Fiddy, *The Role of Analyticity in Image Recovery - Image Recovery: Theory and Applications*, Ed. H. Stark, Academic Press, Florida, pp. 499-529, 1987.

51. E.C. Titchmarsh, *Introduction to the theory of Fourier integrals*, 2nd Edn. Oxford University Press, 1948.

52. A. V. Oppenheim, R. W. Schafer and J. R. Buck, *Discrete-time signal processing*, Prentice-Hall, 1999.

53. M. A. Fiddy, M. Testorf and U. Shahid, "Minimum-phase-based inverse scattering method applied to IPS008," *SPIE*, vol. 5562, pp 188–195, 2004.

54. McGahan R V and Kleinman R E, "Special session on image reconstruction using real data", *IEEE Antenna Propagat. Mag*.38(3) 39-59, 1996.

55. McGahan R V and Kleinman R E, "Second annual special session on image reconstruction using real data", *IEEE Antenna Propagat. Mag*. 39(2) 7-32, 1997.

56. McGahan R V and Kleinman R E, "The third annual special session on image reconstruction using real data, part1", *IEEE Antenna Propagat. Mag*. 41(1) 34-51, 1999.

57. McGahan R V and Kleinman R E, "The third annual special session on image reconstruction using real data, part2", *IEEE Antenna Propagat. Mag*. 41(2) 20-40, 1999.

58. Christelle Ayraud, Jean-Michel Geffrin, Pierre Sabouroux, Kamal Belkebir and Marc Saillard, "Laboratory controlled data for validating inversion algorithms", Institut Fresnel, UMR-CNR 6133, France.

59. Marc G Cote, "Automated Swept-Angle Bistatic Scattering Measurements Using Continuous Wave Radar," *IEEE Transactions on Instrumentation and Measurement*, 41, 2, April 1992, pp 185-192.

60. P. Maponi', L. Misici F. Zirilli`, "A Numerical Method to Solve the Inverse Medium Problem: An Application to the Ipswich Data," *IEEE Antennas and Propagation Magazine*, Vol. 39, No. 2, April 1997.

61. T. Hall, A. Darling, and M. Fiddy, "Image compression and restoration incorporating prior knowledge," *Opt. Lett*. 7, pp. 467—468, 1982.

62. Byrne C L and Fitzgerald R M, "Spectral estimators that extend the maximum entropy and maximum likelihood methods," *SIAM J. Appl. Math*., 44, pp 425–442, 1984.

63. Hsin M. Shieh and Michael A. Fiddy, "Accuracy of extrapolated data as a function of prior knowledge and regularization," *Applied Optics*, vol. 45, 2006.

64. Hsin M. Shieh, Charles L. Byrne, Markus E. Testorf and Michael A. Fiddy, " Iterative image reconstruction using prior knowledge," *J. Opt. Soc. Am. A*, Vol. 23, No. 6, 2006.

65. Markus Testorf and Michael Fiddy, "Imaging from real scattered field data using a linear spectral estimation technique," *Inverse Problems*, vol. 17, pp 1645 – 1658, 2001.

66. A. M. Darling, T. J. Hall and M. A. Fiddy, "Stable, noniterative object reconstruction from incomplete data using a *priori* knowledge," *J. Opt. Soc. Am*., vol .73, pp 1466 – 1469, 1983.

67. Hsin M. Shieh, Charles L. Byrne, Markus E. Testorf and Michael A. Fiddy, " Incorporation of prior information in surface imaging applications," *Proc. SPIE*, vol. 4491, pp 336–345, 2001.

68. J. B. Morris, R. K. McGahan, J. L. Schmitz, R. M. Wing, D. A. Pommet and M. A. Fiddy, " Imaging of Strongly Scattering Targets from Real Data," *IEEE Antennas and Propagation Magazine*, Vol. 39, No. 2, pp 22 – 26, 1997.

69. B. Duchêne, D. Lesselier, and R. E. Kleinman, " Inversion of the 1996 Ipswich Data Using Binary Specialization of Modified Gradient Methods," *IEEE Antennas and Propagation Magazine*, Vol. 39, No. 2, pp 9 – 12, 1997.

70. Kamal Belkebir and Marc Saillard, "Special section: Testing inversion algorithms against experimental data," *Inverse Problems*, vol. 17, pp 1565 – 1571, 2001.

71. C Estatico, G Bozza, A Massa, M Pastorino and A Randazzo, "A two-step iterative inexact-Newton method for electromagnetic imaging of dielectric structures from real data," *Inverse Problems*, vol. 21, pp 81 – 94, 2005.

72. Alexandre Baussard, "Inversion of multi-frequency experimental data using an adaptive multiscale approach," *Inverse Problems*, vol. 21, pp 15 – 31, 2005.

73. O Féron, B Duchêne and A Mohammad-Djafari, "Microwave imaging of inhomogeneous objects made of a finite number of dielectric and conductive materials from experimental data," *Inverse Problems*, vol. 21, pp 95 – 115, 2005.

74. M Donelli, D Franceschini, A Massa, M Pastorino and A Zanetti, "Multi-resolution iterative inversion of real inhomogeneous targets," *Inverse Problems*, vol. 21, pp 51 – 63, 2005.

75. A Litman, "Reconstruction by level sets of n-ary scattering obstacles," *Inverse Problems*, vol. 21, pp 131 – 152, 2005.

76. Francesco Simonetti, Matthew Fleming, and Edwin A. Marengo, " Illustration of the role of multiple scattering in subwavelength imaging from far-field Measurements," *J. Opt. Soc. Am. A*, vol. 25, No. 2, 2008.

77. Fu-Chiarng Chen and Weng Cho Chew, "Experimental verification of super resolution in nonlinear inverse scattering" *Applied Physics Letters*, vol.72, No. 23, 1998.

78. F. Simonetti, "Multiple scattering: The key to unravel the subwavelength world from the far-field pattern of a scattered wave," *Phys. Rev. E.*, issue 3, vol.73, 2006

79. C. K. Rushforth and R. W. Harris, "Restoration, resolution and noise," *J. Opt. Soc. Am.* vol. 58, pp 539–545, 1968.

80. G. Toraldo Di Francia, "Degrees of freedom of an image," *J. Opt. Soc. Am*. vol.59, pp799–804, 1969.

81. T. Habashy and E. Wolf, “Reconstruction of scattering potentials from incomplete data,” *J. Mod. Opt*.,vol. 41, pp 1679–1685, 1994.

82. A. Roger, “Newton-Kantorovitch Algorithm Applied to an Electromagnetic Inverse Problem,” *IEEE Trans. Antennas. Propag*. vol. AP-29, No. 2, 1981.

83. R. F. Remis and P. M. van den Berg, “On the equivalence of the Newton-Kantorovich and distorted Born methods ,” *Inverse Problems*, vol. 16, 2000.

84. David A. B. Miller, “Fundamental limit for optical components,” *J. Opt. Soc. Am. B*, vol. 24, No.10, 2007.

APPENDIX A: CEPSTRAL INVERSION TOOL

I have developed user-friendly software which implements the cepstral inversion method. It loads the calculated quantity V<Ψ> from measurements or simulations, pre- or post-PDFT and executes the cepstral method, allowing a choice of parameters for the reference wave and the cepstral filter itself. In this way, one can see the sensitivity of the inversion (or not) to these parameters and evaluate the quality of the reconstruction.

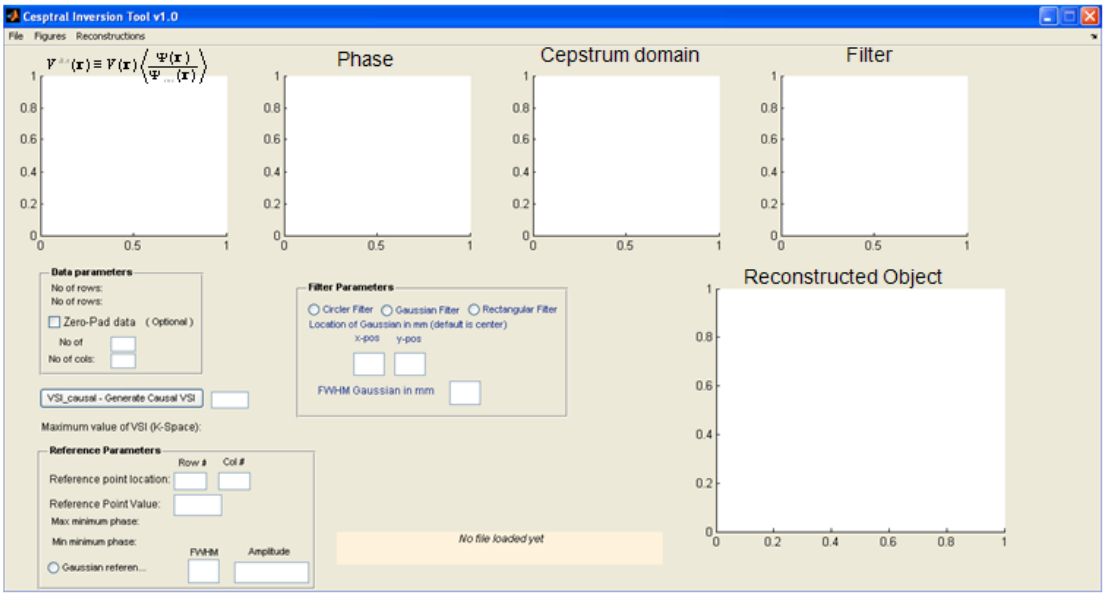

Figure. 6.1. Cepstral Inversion Tool

As a starting step of our algorithm the software enforces causality by moving the k-space data into one quadrant of k-space. It is noteworthy that with measured data one could start directly in this domain rather than form an image of V<Ψ> first. The software then interactively allows users to modify the amplitude and location of the reference wave to ensure that the minimum phase condition is met . It can be very useful to study the relationship between minimum phase fluctuations and the quality of

reconstructions. Once the minimum phase condition is met, which can be verified by visual inspection of the phase of V<Ψ> or by looking at the minimum and maximum value of V<Ψ> displayed in GUI, the next step is to apply filtering in the cepstral domain. Currently this tool offers Gaussian, circular and rectangular filters. We can change the width and location of filter in the cepstral domain to remove unwanted spatial frequencies associated with the field <Ψ>. While we modify the filter we can, in real time, observe its effect on the quality of reconstruction. This tool provides an easy interface to optimize the reference wave and filter to achieve the best quality reconstruction as well as facilitating a helpful intuitive understanding of how the method works. The software also allows users to save and load simulations, which is very handy for keeping track of experiments. In summary this software is a modeling tool to study the inverse scattering problem. In a very short time it can provide an estimate of the shape and permittivity of an object.